Cell

Genomic structure predicts metabolite dynamics in microbial communities

Graphical abstract

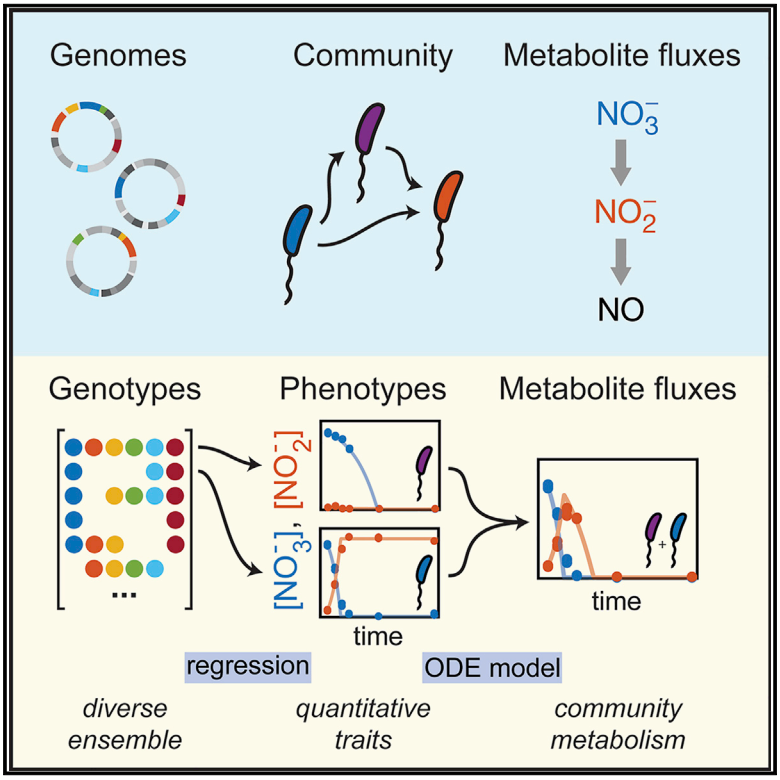

Highlights

- Metabolite fluxes in microbial communities are predictable from individual genotypes
- A diverse collection of 79 bacterial isolates was sequenced and phenotyped
- Gene presence and absence predict metabolic phenotypes of isolates via regression
- A consumer-resource model predicts community metabolite fluxes from phenotypes

Authors

Karna Gowda, Derek Ping, Madhav Mani, Seppe Kuehn

Correspondence

madhav.mani@gmail.com (M.M.), seppe.kuehn@gmail.com (S.K.)

In brief

The presence or absence of specific genes within communities of wild bacterial isolates is sufficient to predict community-level metabolite dynamics without detailed knowledge of pathway regulation or complex ecological processes.

Gowda et al., 2022, Cell *185*, 530–546
February 3, 2022
https://doi.org/10.1016/j.cell.2021.12.036

CellPress

CellPress

Cell

Article

Genomic structure predicts metabolite dynamics in microbial communities

Karna Gowda,[1,2] Derek Ping,[3] Madhav Mani,[4,5,6,*] and Seppe Kuehn[1,2,7,*]
[1]Department of Ecology and Evolution, University of Chicago, Chicago, IL 60637, USA
[2]Center for the Physics of Evolving Systems, University of Chicago, Chicago, IL 60637, USA
[3]Department of Physics, University of Illinois at Urbana-Champaign, Urbana, IL 61801, USA
[4]Department of Engineering Sciences and Applied Mathematics, Northwestern University, Evanston, IL 60208, USA
[5]Department of Molecular Biosciences, Northwestern University, Evanston, IL 60208, USA
[6]NSF-Simons Center for Quantitative Biology, Northwestern University, Northwestern University, Evanston, IL 60208, USA
[7]Lead contact
*Correspondence: madhav.mani@gmail.com (M.M.), seppe.kuehn@gmail.com (S.K.)
https://doi.org/10.1016/j.cell.2021.12.036

SUMMARY

The metabolic activities of microbial communities play a defining role in the evolution and persistence of life on Earth, driving redox reactions that give rise to global biogeochemical cycles. Community metabolism emerges from a hierarchy of processes, including gene expression, ecological interactions, and environmental factors. In wild communities, gene content is correlated with environmental context, but predicting metabolite dynamics from genomes remains elusive. Here, we show, for the process of denitrification, that metabolite dynamics of a community are predictable from the genes each member of the community possesses. A simple linear regression reveals a sparse and generalizable mapping from gene content to metabolite dynamics for genomically diverse bacteria. A consumer-resource model correctly predicts community metabolite dynamics from single-strain phenotypes. Our results demonstrate that the conserved impacts of metabolic genes can predict community metabolite dynamics, enabling the prediction of metabolite dynamics from metagenomes, designing denitrifying communities, and discovering how genome evolution impacts metabolism.

INTRODUCTION

The metabolism of microbial communities plays an essential role in sustaining life on Earth, impacting global nutrient cycles (Falkowski et al., 2008; Canfield et al., 2010; Stein and Klotz, 2016), wastewater treatment (Lu et al., 2014), and human health (Subramanian et al., 2014). A challenge in microbial ecology is understanding how community metabolism is determined by the taxa present, their metabolic traits, and the genes they possess (Widder et al., 2016; Louca et al., 2018). Addressing this challenge requires mapping the genotypes of each community member to its metabolic traits and then deciphering how complex interactions between each member impact the flux of metabolites through the community. Complicating the prediction of metabolite fluxes from community composition, interactions can depend on extracellular metabolites (Lilja and Johnson, 2016), abiotic factors (Ward et al., 2006), cooperation (Cordero et al., 2012), and higher-order effects (Sanchez-Gorostiaga et al., 2019; Mickalide and Kuehn, 2019). Despite these challenges, connecting genomic structure to the collective metabolism of a community is important for functionally interpreting community gene content (Anantharaman et al., 2016), designing synthetic communities (Shou et al., 2007), and understanding how gene gain and loss (Molina and Nimwegen, 2009; Sela et al., 2019) impact community metabolism.

Recent work suggests that the genes present in a community may be more informative about metabolic activity than the identity of strains or species making up the community. Sequencing studies of environmental and host-associated communities show that, while the individual strains or species present are often highly variable (Louca et al., 2018), the genes or pathways present are often observed to be stable across communities in similar environments (Louca et al., 2018; Human Microbiome Project Consortium, 2012). For example, aquatic communities native to bromeliads contain prokaryotes from several functional groups (e.g., methanogens, fermenters, and photoautotrophs). The strain or species representing each functional group varies widely from one plant to the next, but the relative abundance of each functional group is remarkably stable across plants (Louca et al., 2016a). Similarly, studies in oceans and soils that measure both gene content and nutrient levels have found that the relative abundances of specific metabolic genes are better predictors of nutrient levels than the abundances of specific taxa (Jones and Hallin, 2010; Fierer et al., 2012; Louca et al., 2016b). These results suggest that the availability of nutrients, such as organic carbon, oxygen, nitrate, carbon dioxide, and light, constrain the composition of the community in terms of the abundances of specific metabolic capabilities more so than they constrain the taxa possessing those capabilities. One implication of this finding is that communities with similar genomic composition, in terms of the metabolic pathways

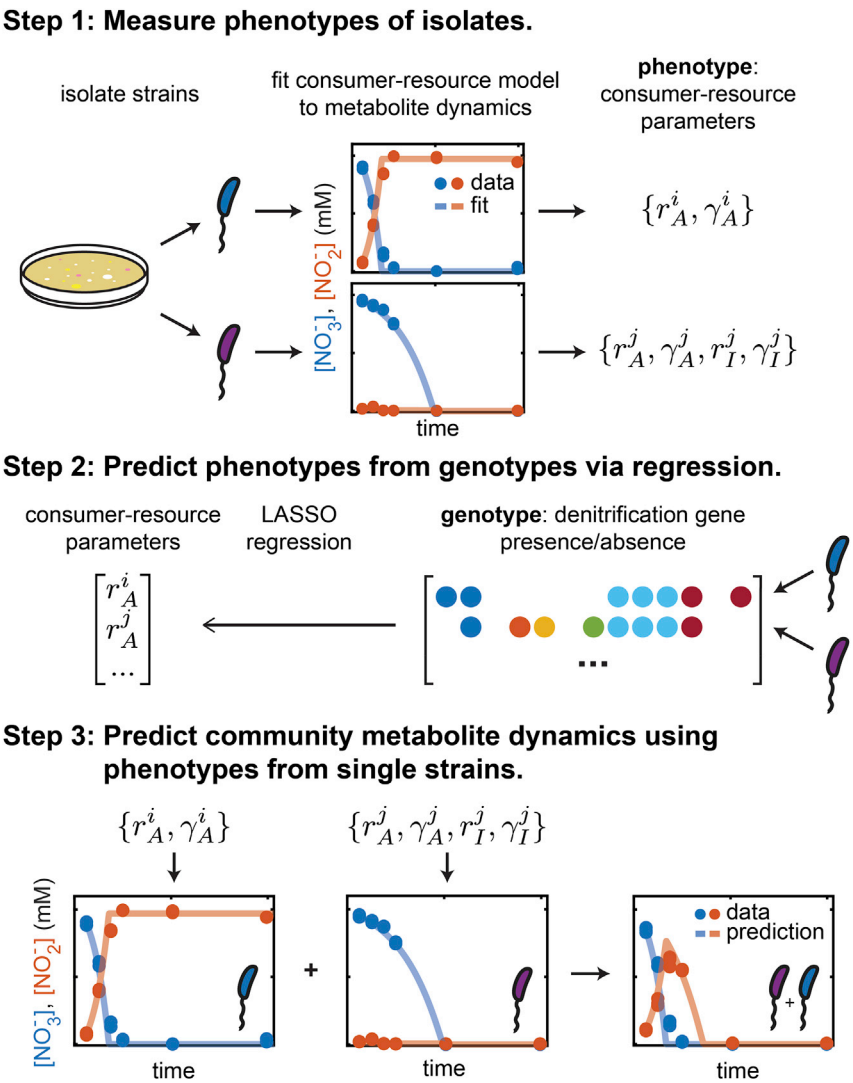

Figure 1. Workflow for predicting community metabolite dynamics from genomic structure

they possess, might exhibit similar rates and productivity of the associated metabolic process, but any such correspondence is yet to be demonstrated.

Corroborating the idea that nutrient availability strongly determines community composition, experiments in fixed nutrient conditions have shown that the metabolic traits of bacterial strains in assembled communities can be highly reproducible. To show this, several groups have sampled complex communities from natural environments and grown them under defined nutrient conditions in the laboratory (Datta et al., 2016; Goldford et al., 2018). Using this approach, Datta et al. showed that marine microbial communities degrading polysaccharide particles exhibit a succession of bacterial taxa (Datta et al., 2016). Succession on these particles arises from initial colonizers that cleave polysaccharides, followed by strains that compete for the resulting oligosaccharides or consume byproducts of sugar metabolism. Similarly, bacterial communities sampled from leaf surfaces and enriched in glucose minimal medium reproducibly yield communities comprising both consumers of glucose and consumers of glucose metabolic byproducts (Goldford et al., 2018).

Although the traits of organisms in an assembled community appear to be strongly influenced by the available nutrients, quantitatively relating genomic structure to the rates and productivity of metabolic processes at the community level remains a challenge. Phenotyping mutants of model organisms has done much to uncover the molecular basis of specific metabolic processes such as denitrification (Zumft, 1997). However, it is unclear how to use a detailed molecular characterization of metabolism in a few model organisms to understand the metabolic traits of organisms in natural communities that possess high levels of genomic diversity (Sakoparnig et al., 2021). Additionally, we lack an understanding of how this genomic diversity drives variation in metabolic traits and how phenotypes of individual taxa combine to give rise to metabolite fluxes through a community.

Here, we address the challenge of mapping gene content to metabolite dynamics by quantifying the flux of metabolites in an ensemble of genomically diverse communities composed of non-model organisms (see Figure 1 for a summary of the approach). We used bacterial denitrification, an essential metabolic process in the global nitrogen cycle that is performed by diverse and culturable bacterial taxa (Lycus et al., 2017), as a model metabolic process. We isolated an ensemble of denitrifiers and measured the dynamics of metabolite consumption and production for each isolate under controlled conditions. We then parameterized metabolite dynamics using a consumer-resource model. The genomic diversity of the ensemble of isolates enabled a simple linear regression approach to mapping gene content to consumer-resource model parameters, which resulted in a sparse and generalizable mapping of gene presence and absence to metabolic phenotypes. Finally, the consumer-resource model captured interactions between strains mediated by resource competition, yielding predictions for community-level metabolite dynamics that we verified experimentally.

RESULTS

Denitrification as a model metabolic process

We used denitrification as a model metabolic process because it is performed by diverse bacterial taxa, it is well characterized at

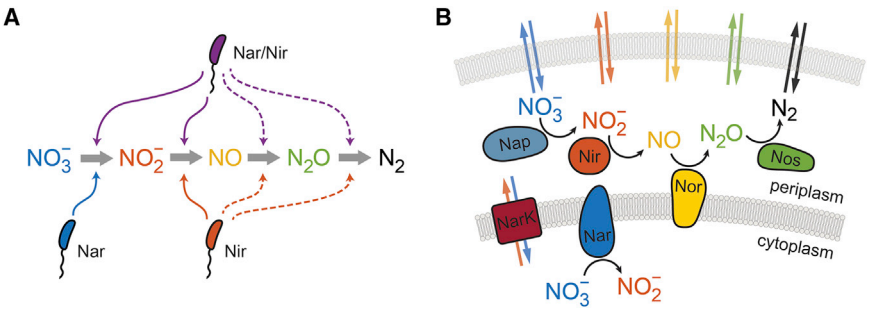

Figure 2. Denitrification as a model metabolic process

(A) Denitrification is a form of anaerobic respiration whereby oxidized nitrogen compounds are used as electron acceptors. The process results in a cascade of reactions from nitrate (NO_3^-) to di-nitrogen (N_2). Some bacteria perform all four steps in the cascade (purple, "Nar/Nir"), whereas others perform only a subset of reactions. Two examples of the latter are shown here: "Nar" strains (blue) perform only nitrate reduction, and "Nir" strains (red) perform nitrite (NO_2^-) reduction and potentially also subsequent steps (dashed lines).

(B) A schematic representation of the molecular steps in the denitrification process. Denitrification serves as the terminal step in the electron transport chain (not shown) and, thereby, contributes to ATP generation. Reduction of nitrate to nitrite takes place either in the cytoplasm (via the enzyme Nar) or in the periplasm (Nap). Nitrate reduction in the cytoplasm via Nar requires nitrate and nitrite to be transported across the inner membrane (NarK1, NarK2, and NarK1K2). The subsequent three steps all occur in the periplasm and are encoded by the reductases Nir, Nor, and Nos as shown. There are two functionally equivalent types of Nir and Nor reductases: NirK/NirS and qNor/cNor, respectively.

the molecular level, and the relevant metabolites are readily quantifiable (Zumft, 1997). Because denitrifiers are easily isolated and cultured (Lycus et al., 2017), we can capture substantial genomic diversity in an ensemble of natural isolates.

Denitrification is a form of anaerobic respiration whereby microbes use oxidized nitrogen compounds as electron acceptors, driving a cascade of four successive reduction reactions, $NO_3^- \rightarrow NO_2^- \rightarrow NO \rightarrow N_2O \rightarrow N_2$ (Zumft, 1997) (Figure 2A). As a biogeochemical process, denitrification is essential to nitrogen cycling at a global scale through activity in soils, freshwater systems, and marine environments (Seitzinger et al., 2006). In addition, denitrification impacts human health through activity in wastewater treatment plants (Lu et al., 2014) and in the human gut (Irrazábal et al., 2014). The process is performed by taxonomically diverse bacteria (Graf et al., 2014) that are typically facultative anaerobes. The denitrification pathway is known to be modular, with some strains performing all four steps in the cascade and others performing one or a nearly arbitrary subset of reduction reactions (Lycus et al., 2017) (Figure 2A). Denitrification in nature is, therefore, a collective process, wherein a given strain can produce electron acceptors that can be utilized by other strains (Lilja and Johnson, 2016).

Denitrification is well understood at the molecular level. The process couples the reduction of oxidized nitrogen compounds to the electron transport chain and, therefore, ATP production. The enzymes (reductases) that perform each step in the cascade are shown in Figure 2B. Reduction of nitrate to nitrite can occur either in the cytoplasm, by the Nar reductase, or the periplasm, using Nap. Inner membrane NarK transporters (NarK1, NarK2, and NarK1K2) facilitate the exchange of nitrate and nitrite between the cytoplasm and the periplasm. The remaining three reactions all occur exclusively in the periplasmic space (Figure 2B). The regulatory elements that control the expression of denitrification genes are also well characterized and include two-component systems that sense the oxidized nitrogen compounds and regulators that detect the loss of oxygen from the environment (Zumft, 1997; Rodionov et al., 2005). Because most of these reactions occur in the periplasm, substrates can readily leak into the surrounding environment, enabling cross-feeding between denitrifiers (Lilja and Johnson, 2016).

We focused experimentally on the first two steps of denitrification: the conversion of nitrate (NO_3^-) to nitrite (NO_2^-) and subsequently nitric oxide (NO) (Figure 2A). Nitrate and nitrite are soluble, enabling high-throughput measurements of metabolite dynamics (Miranda et al., 2001). To obtain a genomically diverse ensemble of non-model organisms, we isolated 78 bacterial strains spanning α-, β-, and γ-proteobacteria from local soils using established techniques (Tables S1–S3; STAR Methods). Each strain was obtained in axenic culture and was characterized as performing one or both of the first two steps of denitrification. Therefore, strains were classified into one of three possible phenotypes (Figures 2A and 3A): (1) Nar/Nir strains that perform both nitrate and nitrite reduction ($NO_3^- \rightarrow NO_2^- \rightarrow NO$), (2) Nar strains that perform only nitrate reduction ($NO_3^- \rightarrow NO_2^-$), and (3) Nir strains that perform only nitrite reduction ($NO_2^- \rightarrow NO$). In addition to these 78 isolates, our strain library also included the model denitrifier *Paracoccus denitrificans* (ATCC 19367).

Parameterizing metabolite dynamics

We first set out to quantify the metabolic phenotypes of each isolate in our diverse strain library (Step 1, Figure 1). We focused our efforts on quantifying the dynamics of the relevant metabolites, nitrate and nitrite. To accomplish this, strains were inoculated at low starting densities into 96-well plates containing a chemically defined, electron-acceptor-limited medium containing succinate as the sole non-fermentable carbon source (succinate-defined medium, SDM; Table S4; STAR Methods), with either nitrate or nitrite provided as the sole electron acceptor. Cultures were then incubated under anaerobic conditions (STAR Methods). Small samples (10 μL) were taken at logarithmically spaced time intervals over a period of 64 h and assayed for nitrate and nitrite concentrations (STAR Methods). At the end of the time course, optical density was assayed. The measurement resulted in a time series of nitrate and nitrite production/consumption dynamics in batch culture (points, Figure 3A). Contamination between wells using this culturing and sampling approach was assessed to be low (STAR Methods).

To parameterize the metabolite dynamics of each strain within a common framework, we utilized a consumer-resource model,

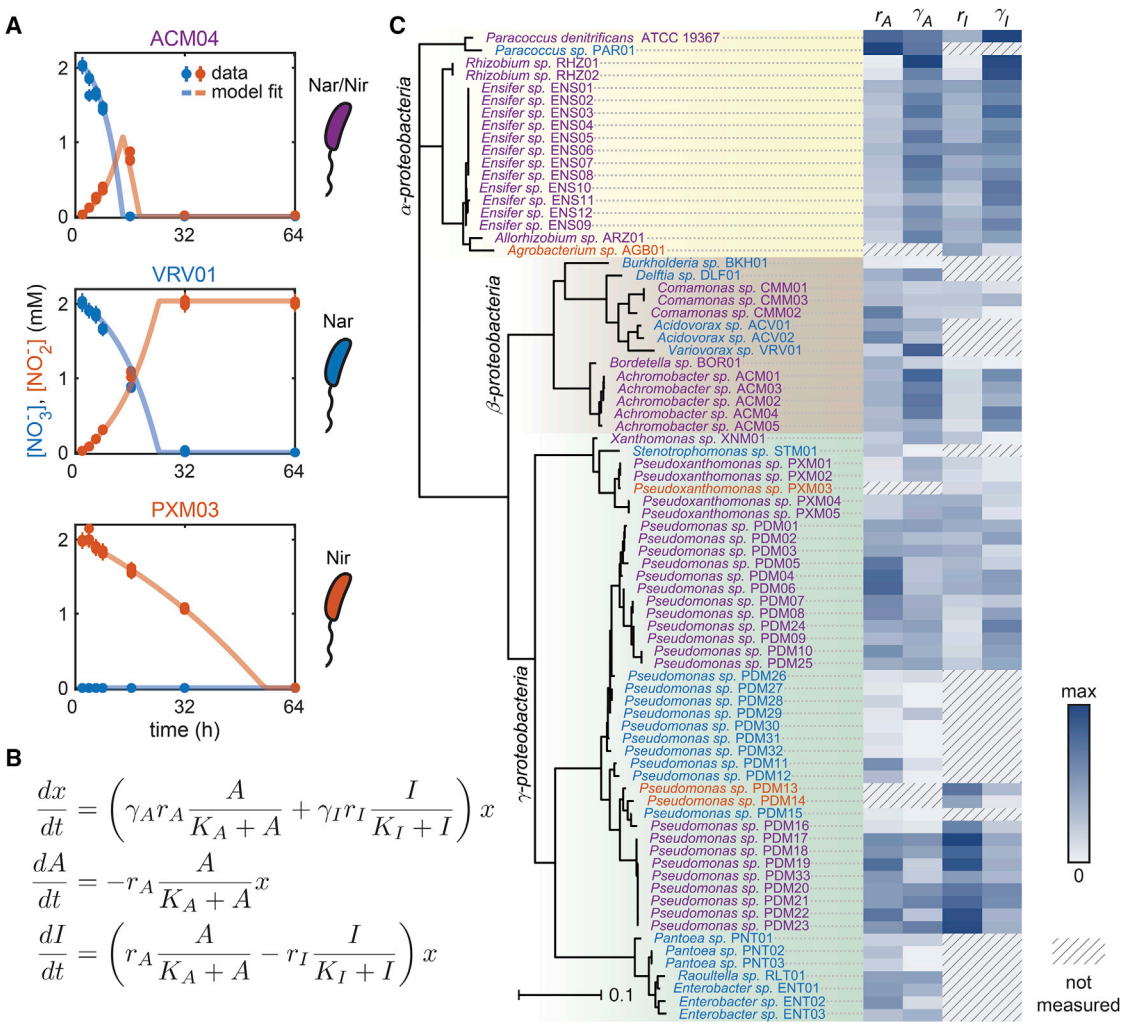

$$\frac{dx}{dt} = \left(\gamma_A r_A \frac{A}{K_A + A} + \gamma_I r_I \frac{I}{K_I + I}\right) x$$

$$\frac{dA}{dt} = -r_A \frac{A}{K_A + A} x$$

$$\frac{dI}{dt} = \left(r_A \frac{A}{K_A + A} - r_I \frac{I}{K_I + I}\right) x$$

Figure 3. Quantifying nitrate and nitrite dynamics in an ensemble of denitrifiers to map genomic structure to community metabolism

(A) Example batch culture metabolite dynamics for Nar/Nir (purple), Nar (blue), and Nir (red) isolates. Nitrate (NO_3^-, blue points) and nitrite (NO_2^-, red points) dynamics are measured at logarithmically spaced intervals (circles) via sampling and colorimetric assay (STAR Methods), with ± 5% error bars shown. Biomass densities are only measured at the final time point. Curves show fits to a consumer-resource model shown in (B).

(B) A consumer-resource model of nitrate and nitrite reduction by each strain describes the evolution of biomass density (x, OD), nitrate concentration (A, mM), and nitrite concentration (I, mM) with time. The model is parameterized by reduction rates r_A and r_I (mM/OD/h), and yields γ_A and γ_I (OD/mM), for growth on nitrate and nitrite, respectively. The affinity parameters K_A and K_I (mM) were not well constrained by the data and were fixed for all strains in the library (STAR Methods).

(C) Phylogenetic tree and normalized consumer-resource parameters for 79 denitrifying strains (78 isolates and the model denitrifier *Paracoccus denitrificans*). The strain library comprised 51 Nar/Nir, 24 Nar, and 4 Nir strains. Consumer-resource parameters were measured in a succinate-defined medium (SDM). Phylogenetic tree constructed using the 16S rRNA gene, and scale bar represents the estimated number of substitutions per site. Darker colors indicate larger values of the normalized parameters. Nitrate and nitrite reduction parameters were not measured for Nir and Nar strains, respectively. Consumer-resource parameters measured across diverse isolates constituted a dataset for relating genomic diversity to metabolite dynamics. See also Figure S1 and Tables S1–S5.

which explicitly relates the growth of each strain to the dynamics of metabolite production and consumption (Figure 3B; Equation 3; STAR Methods). The model contains up to six parameters: rates (r_*, mM/OD/h), biomass yields (γ_*, OD/mM), and affinities (K_*, mM), for the substrates nitrate (A) and nitrite (I). For each strain in monoculture, we parameterized the consumer-resource model using measured denitrification dynamics across a range of initial biomass densities and nitrate/nitrite concentrations (Figures 3A and S1A–S1E; STAR Methods). These data allowed us to quantify rates (r_*) and biomass yields (γ_*) but not the affinity parameters (K_*), which require measuring growth rates at very low substrate concentrations. Because the results of parameter fits were not sensitive to the values of K_* across a broad range (Figures S1F–S1I; STAR Methods), we fixed the affinity parameter to a small constant value. Therefore, we captured the phenotype of each strain in the library using at most four parameters: r_A, r_I, γ_A, and γ_I (the models for Nar and Nir strains correspond to setting $r_I, \gamma_I = 0$ or $r_A, \gamma_A = 0$, respectively). Yields (γ_*) were inferred using optical density measurements at $t = 64$ h, and rates (r_*) were inferred by fitting the observed nitrate and nitrite dynamics to the

consumer-resource model (Figure 3B). For the majority of strains in our library (62 out of 79), a single set of parameters quantitatively described metabolite dynamics across a range of initial biomass densities and nitrate/nitrite concentrations. The consumer-resource model captured metabolite dynamics over a restricted set of initial conditions for the remaining 17 strains (Figures S1J–S1L; Table S5; STAR Methods). Using a representative subset of four strains, we confirmed that biomass density dynamics were well predicted by the consumer-resource parameters, despite the fact that biomass density was not directly measured over time (Figure S1M; STAR Methods).

Fitting our consumer-resource model to data for each strain yielded a quantitative description of the metabolic traits (i.e., denitrification rates and yields) of each strain in the library (Figure 3C). We observed large variability between taxa, with coefficients of variation for rate constants (r_A, r_I) around 70% and yields (γ_A, γ_I) around 100%. We also observed some patterns of phylogenetic conservation, for example, α-proteobacteria produced generally higher yields than β- or γ-proteobacteria did, and a clade of *Pseudomonas* sp. isolates showed consistently higher rates of nitrite reduction than most other strains (PDM17-23, Figure 3C). Despite these patterns, the prevalence of each of the three qualitative phenotypes is not strongly dependent on phylogeny, with each present across the tree (Figure 3C). The latter observation is consistent with pervasive horizontal gene transfer of denitrifying enzymes (Heylen et al., 2006; Jones et al., 2008). Finally, neither did we observe a correlation between rates and yields, nor was there an obvious bound on these parameters, suggesting that they are not subjected to a trade-off.

Predicting metabolite dynamics from genomes

Understanding how genomic variation impacts metabolite dynamics at the community level requires first learning how genomic variation impacts the metabolic traits of individual strains. Therefore, we sought to determine how genomic variation across the strains in our library is related to variation in denitrification rates and yields (Figure 3C). One common approach to the problem of relating genomes to metabolite dynamics is constraint-based modeling. Constraint-based models infer the set of all metabolic reactions performed by an organism from an annotated genome, and then predict growth rates and metabolite fluxes, assuming the metabolic network is in steady state and is subject to biologically motivated constraints (Orth et al., 2010). Constraint-based methods have found some success in predicting collective metabolism from genomes (Klitgord and Segrè, 2010; Mori et al., 2016; Harcombe et al., 2014), but these methods require significant manual refinement (Norsigian et al., 2020), complicating the prospect of making predictions from the genomes of non-model organisms. As a result, successfully constructing constraint-based models of denitrification for all strains in our library is a daunting task.

We took an alternative approach to the problem of mapping genomes to metabolite dynamics. We asked whether the variation in metabolic phenotypes across strains in our library can be quantitatively predicted simply from knowledge of the genes possessed by each strain. Our conjecture was motivated by two observations. First the metabolic traits of bacteria correlate strongly with environmental variables in marine microbial communities (Louca et al., 2016a). For example, the relative abundance of taxa capable of nitrate reduction are strongly correlated with local temperature, phosphate, and nitrate levels, suggesting that the presence of genes responsible for those traits might also be predictable from nutrient levels and temperature. Second, the statistics of gene presence and absence across large numbers of sequenced genomes provides insights into the functional roles that genes play in pathways, such as the coupling between dihydrofolate reductase and thymidylate synthase activity in the folate metabolism pathway (Schober et al., 2019). Together, these observations suggest that the genes a strain possesses could allow for predictions of metabolic traits. Therefore, rather than building constraint-based metabolic models for all of our strains, each of which would require significant manual refinement, we took a simple regression approach.

We used linear regression to predict the consumer-resource model parameters (Figure 3C) of each strain from gene presence and absence (Step 2, Figure 1). To accomplish this, we performed whole genome sequencing on all 79 strains in the library. Then, we assembled and annotated each genome (STAR Methods) and determined the complement of 17 denitrification-related genes possessed by each strain (Table S6), exploiting the fact that the molecular and genetic basis of denitrification is well understood (Zumft, 1997). We identified not only the reductases that perform the reduction of the oxidized nitrogen compounds but also the sensors/regulators (Rodionov et al., 2005) and transporters (Moir and Wood, 2001) known to be involved in denitrification (STAR Methods). We intentionally excluded genes encoding structural subunits and chaperones required for the functioning of any reductase (Table S7) because such genes have the same presence/absence pattern as the corresponding reductases and, therefore, would have identical predictive power. The presence and absence the denitrification-related genes in each genome are presented in Figure 4A. Patterns of gene presence and absence agree well with known features of the denitrification pathway, including the mutual exclusion (Pearson correlation -1.0 among nitrite reducers) of the two reductases performing nitrite reduction, NirS and NirK (Jones et al., 2008; Jones and Hallin, 2010).

Next, we showed that the presence and absence of denitrification genes in each strain were sufficient to quantitatively predict metabolite dynamics in monoculture. Specifically, we constructed a linear regression where the measured phenotypic parameters of our consumer-resource model were predicted on the basis of gene presence and absence (Figure 4B). Consistent with the observation that bacterial genomes are streamlined (Lynch, 2006), almost all strains possessing nitrate and/or nitrite reductase performed the associated reactions in culture (the only exception being the Nar strain *Acidovorax* sp. ACV01, which possesses both nitrate and nitrite reductase, Figure 4A). Therefore, we carried out independent regressions for each consumer-resource model parameter using only strains that performed the associated reaction (i.e., Nar and Nar/Nir strains for the r_A and γ_A regressions, and Nir and Nar/Nir strains for the r_I and γ_I regressions). The regression coefficients for each gene quantify the impact of the presence of the gene on a given phenotypic parameter. We used L_1-regularized regression (least absolute shrinkage and selection operator, LASSO) to avoid

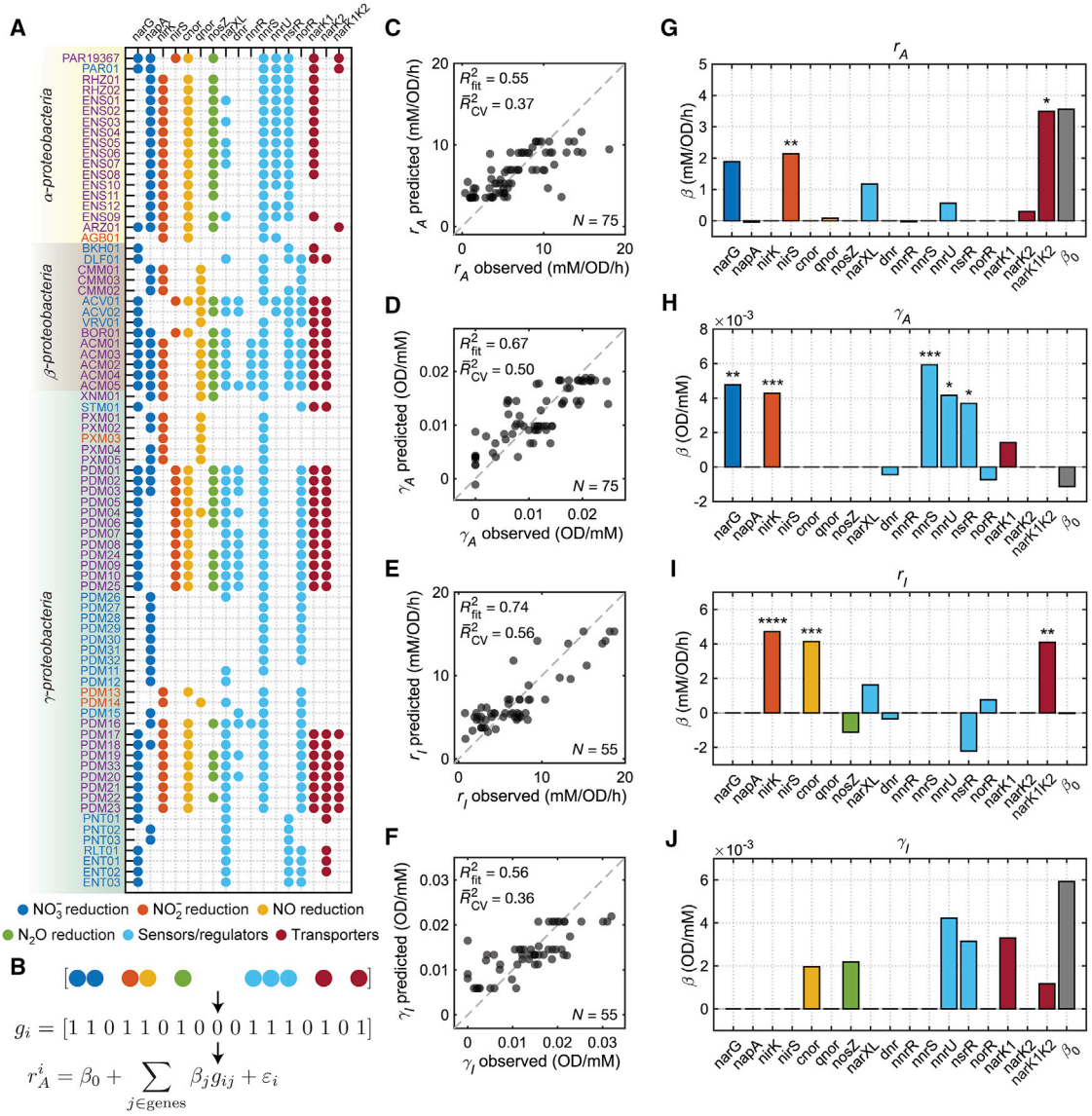

Figure 4. A statistical mapping from gene presence and absence to metabolite dynamics of individual strains

(A) The presence and absence of genes in the denitrification pathway for the 79 denitrifying strains in our library. The color of each circle corresponds to the gene function as indicated in the legend further on.

(B) Observed consumer-resource phenotypic parameters for each strain in SDM (e.g., nitrate reduction rate r_A, Figure 3C) were linearly regressed against gene presence and absence via L_1-regularized regression, resulting in regression coefficients β_j for each gene j, an intercept β_0, and a noise term ε_i for each observation i. Coefficient β_j captures the impact of possessing gene j on the corresponding phenotypic parameter. Independent regressions were performed for each phenotypic parameter.

(C–F) Predicted values of r_A, γ_A, r_I, and γ_I, respectively, plotted against measured values. The dashed line indicates perfect agreement between observations and predictions. The in-sample coefficients of determination for these data (R^2_{fit}) and the out-of-sample coefficients of determination estimated via iterated 4-fold cross-validation ($\bar{R}^2_{CV}$) are shown. N indicates the number strains in each regression. Strains that do not perform a particular reaction were omitted from the corresponding regression (e.g., Nir strains were excluded from the regression for r_A).

(G–J) Estimates of β for each gene and β_0 for r_A, γ_A, r_I, and γ_I, respectively. Asterisks indicate significance level for each β (*: $p \leq 0.05$, **: $p \leq 10^{-2}$, ***: $p \leq 10^{-3}$, and ****: $p \leq 10^{-4}$; STAR Methods). See also Figure S2 and Tables S6 and S7.

overfitting, performing independent regressions for each of the phenotypic parameters in our consumer-resource model (Figures 4C–4J; STAR Methods). By design, LASSO searches for a level of sparsity that optimizes predictive power, often selecting a few variables to make predictions while forcing other coefficients (β_j) to zero. The result can then be a sparse model that makes predictions using a handful of variables. It is important to note that LASSO does not first presume that a few variables are sufficient to make a prediction (in contrast to forward stepwise and best subset regression approaches). In the situation

where strong predictive power does not exist, e.g., a phenotypic parameter cannot be predicted well from gene presence and absence, LASSO would effectively fail to identify a predictive model by returning $\beta_j = 0$ for all genes (Fraebel et al., 2020).

Performing LASSO regressions on our dataset revealed that the presence and absence of a small set of genes is highly predictive of the consumer-resource parameters for all strains in our library (Figures 4C–4J). The in-sample coefficients of determination (R^2_{fit}) of our regressions were between 0.55 and 0.74 depending on the phenotypic parameter. Crucially, our regression approach generalized out-of-sample, as determined by iterated 4-fold cross-validation (1×10^4 iterations; STAR Methods), albeit with a slightly lower predictive power ($\overline{R}^2_{CV}$ between 0.36 and 0.56). Therefore, across a diverse set of natural isolates, knowledge of the full complement of genes a denitrifying strain possesses is sufficient to accurately predict the rates and biomass yields of that strain on nitrate and/or nitrite.

Validating regression approach to predicting traits from gene presence and absence

Our regression approach leveraged biological knowledge of the denitrification pathway to predict metabolite dynamics, in effect presuming that denitrification gene content is the only significant genomic feature for prediction. To investigate whether this assumption is correct, we asked whether other genomic properties could better predict metabolite dynamics and also examined the role that phylogenetic correlations played in our predictions.

First, we tested the predictive capability of sets of randomly selected genes. To do this, we chose sets of 17 random genes that were not strongly correlated with any denitrification genes but retained the same marginal frequency distribution in the population as the denitrification genes. We found that regressions using these randomly selected genes had, on average, much less predictive power than regressions using the denitrification genes (Figures S2A–S2C; STAR Methods). We also tested augmented sets of up to 2,048 predictors that were generated by adding varying numbers of randomly selected genes to the 17 denitrification genes. We found that the prediction quality changed remarkably little as more genes were added and that even sets of 2,048 predictors (representing approximately 30%–50% of genes in each genome) contained about as much predictive power as the regressions using the 17 denitrification genes alone (Figure S2D; STAR Methods). This result indicates that the 17 denitrification genes harbor the majority of gene presence and absence predictive power.

Second, we tested whether 16S rRNA copy number, genome size, or GC-content improves the predictive ability of denitrification gene presence/absence regressions. We tested these genomic features because: (1) 16S rRNA copy number has been observed to correlate positively with maximal growth rate in nutrient-rich conditions (Roller et al., 2016; Li et al., 2019), (2) smaller genomes are associated with faster growth (Lynch, 2006; Li et al., 2019), and (3) GC-content has been investigated as a correlate for numerous bacterial phenotypes, such as optimal growth temperature (Galtier and Lobry, 1997), and can serve as a baseline for spurious phylogenetic correlations because it is a slowly evolving genomic property that exhibits a high degree of phylogenetic correlation (Haywood-Farmer and Otto, 2003). We found that including these additional predictors in our regressions alongside the 17 denitrification genes did not meaningfully improve predictive ability or alter the inferred coefficients (STAR Methods). Thus, denitrification gene presence and absence outperformed these coarse genomic features.

Third, we examined the role of correlations in consumer-resource parameters between closely related strains in the success of our regressions. We quantified the extent of phylogenetic correlation in our 79-strain library by computing the autocorrelation (Moran's I) for each consumer-resource parameter as a function of phylogenetic distance (STAR Methods). We observed that the rate parameter r_A was correlated to a small degree ($\max(I) = 0.16$) over short a phylogenetic distance (16S distance 0.01), whereas the parameters γ_A, r_I, and γ_I showed a modest degree of correlation ($\max(I) =$ 0.33, 0.27, and 0.48, respectively) over relatively longer distances (16S distance 0.16, 0.06, and 0.12, respectively). Pruning clades of closely related strains (e.g., ENS01–08, PDM20–23, Figure 3C) from the dataset decreased the correlation of γ_A, r_I, and γ_I ($\max(I) =$ 0.30, 0.21, and 0.39, respectively; 16S distance 0.05, 0.06, and 0.09, respectively) but had little impact on the correlation of r_A. Thus, some of the phylogenetic correlation is attributable to the over-representation of close relatives. Finally, we showed that the presence of these close relatives in our dataset did not skew the results of our regressions. We performed regressions on the pruned dataset (comprising 64 strains) and found that the predictive power and regression coefficients were similar to those for the full dataset (STAR Methods). From this, we concluded that the over-representation of close relatives did not have a large impact on the results of our regressions on the consumer-resource parameters.

Generalizing the regression approach to an alternative medium condition

Having mapped gene content to metabolite dynamics in a medium with succinate supplied as the carbon source, we next asked whether our regression approach would generalize to other media conditions. Of the 79 strains in our library, 64 grew on a defined medium with acetate supplied as the sole (non-fermentable) carbon source (acetate-defined medium, ADM; Table S1; STAR Methods). We assayed nitrate and nitrite dynamics for the 64 strains in this medium and inferred consumer-resource parameters. We observed that the consumer-resource parameters in the SDM and ADM conditions were strongly correlated (Pearson correlations 0.52–0.93, Figure 5A). Furthermore, LASSO regressions to predict consumer-resource model parameters measured in ADM from gene presence and absence achieved predictive power similar to what we observed in SDM (STAR Methods). The regression coefficients were correlated between nutrient conditions (Figure 5B), suggesting that the impacts of genes on phenotypes were conserved between conditions. We note, however, that rates and yields in ADM were systematically lower relative to SDM (Figure 5A), consistent with what has been observed previously for relative growth rates on these carbon sources (Forchhammer and Lindahl, 1971; Hempfling and Mainzer, 1975). Consequently, the magnitudes of regression coefficients were generally smaller in ADM than in SDM (Figure 5B). This indicates that, while conserved genotype to phenotype relationships may generally underlie predictive power across different environments and media conditions, predictions for a particular environment will

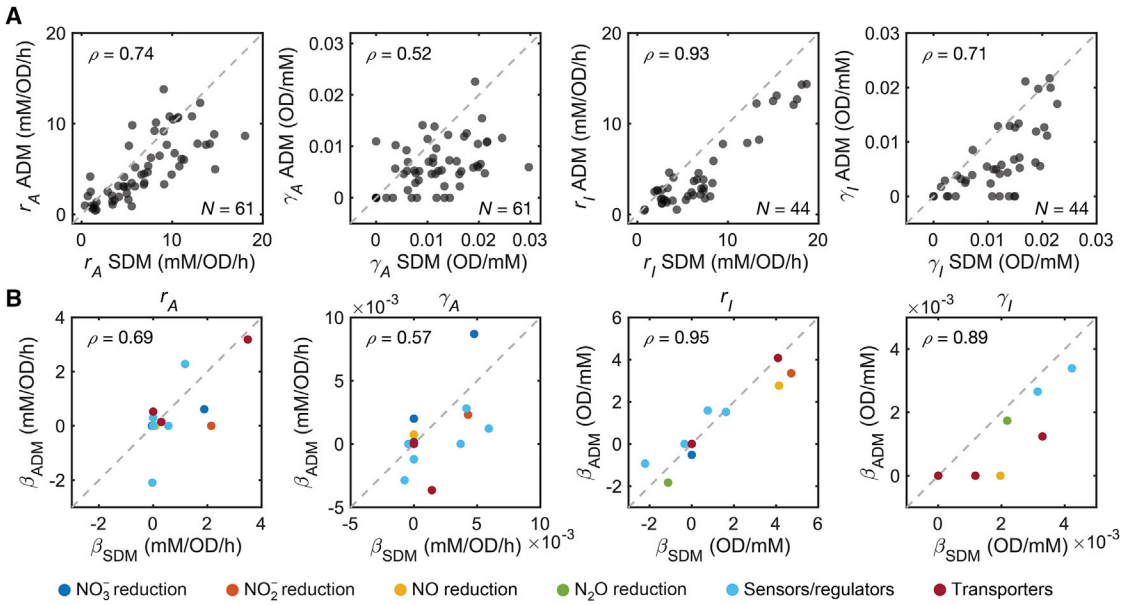

Figure 5. Metabolite dynamics of individual strains are predictable from gene presence and absence in an alternate carbon source

All strains in the 79-strain library were screened for growth on an acetate-defined medium (ADM), and consumer-resource parameters were measured for the 64 strains that grew in this medium.

(A) Observed consumer-resource parameters on succinate-defined medium (SDM) are plotted against observed parameters on ADM. The dashed line indicates perfect agreement between the values observed on SDM and ADM. The Pearson correlations between the observed values are shown, and $p < 10^{-4}$ for all correlations (permutation test).

(B) The consumer-resource parameters on ADM were regressed against gene presence and absence via L_1-regularized linear regression. The resulting regression coefficients, β_{ADM}, are plotted against the coefficients for regressions on parameters measured in SDM, β_{SDM} (shown also in Figures 4G–4J). The dashed line indicates perfect agreement between each pair of regression coefficients. Pearson correlations are shown, and $p = 0.008$, 0.01, $< 10^{-4}$, and $< 10^{-4}$ for r_A, γ_A, r_I, and γ_I, respectively (permutation test). The color of each point corresponds to the gene function, as indicated in the legend further on. See also Table S1.

be more accurate when trained using data measured in that environment.

Mechanistic interpretation of regression coefficients

Why did gene presence and absence alone hold such strong predictive power for metabolite dynamics, and why did the regressions select specific genes in the denitrification pathway as informative predictors? We propose that by characterizing metabolic phenotypes in terms of rates and yields, we captured the salient features of the metabolic process for each strain and that this enabled the regressions to succeed by exploiting the conserved correlations between the presence of specific genes and metabolic phenotypes. In some cases, these correlations appear to be related to the functional roles of specific genes in the pathway. We found that, for some genes, the sign and magnitude of the regression coefficients agree qualitatively with known properties of the associated enzymes. For example, previous comparisons between membrane-bound and periplasmic nitrate reductases (encoded by *narG* and *napA*, respectively; Figure 2B) in multiple bacterial strains showed that the membrane-bound enzyme exhibits higher nitrate reduction activity *in vitro* than the periplasmic enzyme (Stewart et al., 2002; Van Alst et al., 2009; Ikeda et al., 2009; Bell et al., 1990; Warnecke-Eberz and Friedrich, 1993). This accords with the large positive coefficient for *narG* in the nitrate reduction rate regression (Figure 4G). Similarly, in the nitrite reduction rate regression, we observed a large positive coefficient for the gene encoding the copper-based nitrite reductase (*nirK*) (Figure 4I), which in previous studies, showed markedly higher activity *in vitro* (Abraham et al., 1993; Masuko et al., 1984; Iwasaki and Matsubara, 1972; Liu et al., 1986; Kakutani et al., 1981; Kukimoto et al., 1994; Michalski and Nicholas, 1985; Sawada et al., 1978; Denariaz et al., 1991) and *in vivo* (Glockner et al., 1993) compared with the alternate nitrite reductase enzyme encoded by *nirS* (Zumft, 1997; Timkovich et al., 1982; Gordon et al., 2003; Besson et al., 1995; Sawhney and Nicholas, 1978). Further, our regression coefficients showed larger contributions of *narG* versus *napA* to yield on nitrate (Figure 4H) and, similarly, *cnor* versus *qnor* to yield on nitrite (Figure 4J). Both of these observations are consistent with the fact that the genes encoded by *narG* and *cnor* contribute more to the proton motive force (and, therefore, to ATP generation) than their alternatives (*napA* and *qnor*, respectively) do (Ferguson and Richardson, 2004). Finally, the transporter encoded by the gene *narK1K2* (Figure 2B) is a fusion of the nitrate/H^+ symporter NarK1 and the nitrate/nitrite antiporter NarK2, the latter of which is crucial for exchanging nitrate and nitrite between the cytoplasm and periplasm during denitrification when the membrane-bound nitrate reductase is utilized. In *Paracoccus denitrificans*, this fusion has been shown to have substantially higher affinity for nitrate than NarK2 alone, resulting in higher growth rates under denitrifying conditions (Goddard

et al., 2008). This agrees with what we found in the nitrate and nitrite reduction rate regressions, in which we observed large positive contributions of *narK1K2* (Figures 4G and 4I).

Taken together, these observations suggest that the regressions exploited conserved correlations between gene presence and metabolic traits that reflect known mechanistic properties of the denitrification pathway. It is important to note, however, that for many nonzero coefficients in our regressions, notably those corresponding to regulators, there is no clear mechanistic interpretation. Further, given that our regressions were trained on genomes of wild isolates and not on phenotypes of deletion mutants, we do not expect that the regression can be reliably used to predict mutant phenotypes. Instead, we expect that the regressions exploited the tendency for strains possessing specific genes to have specific traits on average (e.g., strains with NarG tend to have high r_A, γ_A). These correlations between the presence of specific genes and metabolic traits qualitatively agree with the mechanistic details of some genes in the pathway, but we do not expect the regression coefficients to make causal predictions about the loss of a single gene.

Implications of a statistical approach to mapping genomic structure to metabolic traits

Our statistical approach took two important steps toward mapping genomic structure to metabolic dynamics at the single-strain level. First, by making quantitative measurements in the laboratory, we removed the confounding environmental factors present in sequencing and metabolomic studies of natural communities to reveal that gene content has a conserved impact on dynamic metabolic phenotypes. Second, our results suggest that a statistical approach could be used to discover the key genomic features of pathways that determine other metabolic phenotypes, complementing direct genetic investigation of model organisms (Nichols et al., 2011). Finally, our predictions of metabolic phenotypes from genomes apply across a range of conditions and generalized well out-of-sample, suggesting that this approach can predict metabolite dynamics in settings for strains where only genome sequence data are available. These insights were made possible by parameterizing metabolic phenotypes across a genomically diverse strain library of non-model organisms, thereby exploiting genomic variation to learn the mapping from genotype to metabolic phenotypes.

Predicting metabolite dynamics in communities

Predicting community metabolite dynamics from genomic structure requires mapping single-strain phenotypes to collective behavior. Previous studies have found some success in predicting metabolite dynamics in consortia from knowledge of the monoculture metabolite consumption dynamics (Erbilgin et al., 2017; Medlock et al., 2018). These approaches used simple assumptions, such as a fixed rate of metabolite production or consumption for each strain (Medlock et al., 2018), rather than a dynamic model of metabolites. To predict community metabolite dynamics, we used the consumer-resource modeling formalism that describes metabolite dynamics for each strain to make quantitative predictions for metabolite dynamics in communities of multiple strains (Step 3, Figure 1). Since the consumer-resource parameters were sparsely encoded by the genomes of each strain (Figure 4), predicting community metabolite dynamics from the consumer-resource model would provide a mapping from gene content to community metabolism.

Therefore, we extended to our modeling formalism to *N*-strain communities by adding the rate contributions of each strain to the dynamics of nitrate and nitrite (Figure 6B; Equation 10; STAR Methods). This "additive" model assumes that strains interact only via cross-feeding and resource competition for electron acceptors. This model also assumes that the rates and yields on nitrate and nitrite for strains in pair culture are the same as in monoculture. As a result, the model provides predictions for *N*-strain community metabolite dynamics given the consumer-resource model parameters for individual strains without any free parameters.

To evaluate the ability of our consumer-resource model to make predictions of metabolite dynamics in communities, we used measured consumer-resource parameter values (Figure 3C) and not the values predicted by gene presence and absence (Figures 4C–4F). This allowed us to disambiguate the errors associated with the failure of the model to predict metabolite dynamics from the errors associated with predicting phenotypic parameters from genomes. However, as we subsequently discuss, using consumer-resource model parameters predicted from genomes has, at most, a modest impact on errors in our predictions of community metabolite dynamics.

Predicting metabolite dynamics in two-strain communities

We tested the ability of this approach to predict metabolite dynamics in all pair combinations of 12 strains from our library (4 Nar/Nir, 4 Nar, and 4 Nir). We assembled communities in 96-well plates containing SDM, supplying either nitrate or nitrite initially in two separate experimental conditions and then sampled over a 64-h period to measure concentrations of nitrate and nitrite (STAR Methods). Remarkably, we found that the additive model accurately predicted the metabolic dynamics for most 2-strain communities (Figures 6, S3A, and S3B) using only the measured consumer-resource parameters for individual strains. Specifically, the third column of Figure 6A shows the zero-free-parameter predictions (curves) of denitrification dynamics in 2-strain communities, which agreed well with measurements (points). The 2-strain community predictions include non-trivial dynamics, such as a transient increase in nitrite for a Nar/Nir + Nar community. In addition, we observed that the additive model accurately predicted total endpoint optical densities and community compositions (Figure S4; STAR Methods) in most cases, indicating that the model generally captures strain abundance dynamics in communities.

We quantified the quality of the additive model predictions for metabolite dynamics by computing a normalized root-mean-square error (NRMSE; see caption of Figure 6; Equation 12; STAR Methods). We found that most 2-strain communities have NRMSE between 0 and 2, indicating that our model successfully predicted metabolite dynamics given only the measured consumer-resource parameters for each strain. Predictions of metabolite dynamics in pair cultures were also accurate when using consumer-resource parameters predicted from genomes via regression (Figures S5A and S5B; STAR Methods). Further, the success or failure of the model predictions depended on the phenotypes of the strains present. The model

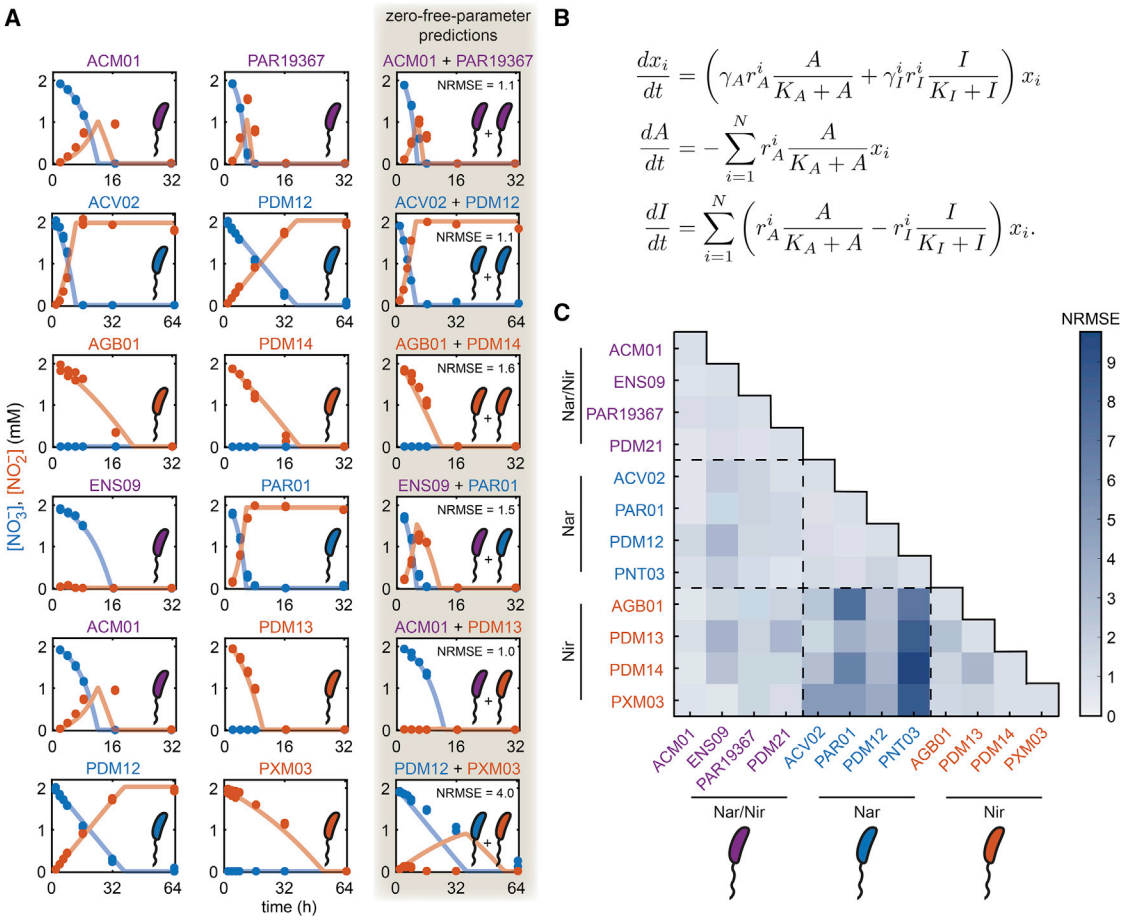

Figure 6. Metabolite dynamics in two-strain communities are predictable from monocultures

(A) Examples of pair culture dynamics for all combinations of the three denitrification phenotypes (Nar/Nir, purple; Nar, blue; Nir; red). The first two columns show metabolite dynamics for each of two strains cultured individually. The third column shows the metabolite dynamics for pair cultures of the two strains (points) with zero-free-parameter predictions using the consumer-resource model (curves, see model in B). All cultures were performed in SDM, and predictions were based on measured monoculture consumer-resource parameters in SDM, not those inferred from genomes. Errors in pair culture predictions are shown in each panel in the third column as quantified by the normalized root-mean-square error (NRMSE). For pair cultures, we defined $\mathrm{NRMSE}_{ij} = \mathrm{RMSE}_{ij}/((\mathrm{RMSE}_i^2 + \mathrm{RMSE}_j^2)/2)^{1/2}$, where RMSE_{ij} is the root-mean-square error between model predictions and observed metabolite concentrations of strains i and j in pair culture, and RMSE_i and RMSE_j are the RMSEs of strains i and j in monoculture. NRMSE in the range 0–2 indicates errors in 2-strain communities that are within 2-fold of fits associated with their constituent monocultures.

(B) An N-strain consumer-resource model (based on the model in Figure 3B) was used to predict pair culture metabolite dynamics ($N = 2$). A and I are nitrate and nitrite concentrations, respectively. x_i denotes the biomass density of strain i with parameters r_A^i, γ_A^i, r_I^i, and γ_I^i, which were determined from monoculture experiments (Figure 3C). The K_* values were fixed at 0.01 mM for all strains.

(C) A matrix of NRMSE values quantifying the quality of model predictions for all pairs of 12 strains: 4 Nar/Nir, 4 Nar, and 4 Nir. NRMSE values are shown for communities cultured in SDM with nitrate initially supplied, with the exception of Nir + Nir pairs for which nitrite was initially supplied. Only Nar + Nir communities are poorly predicted by the consumer-resource model (permutation test, $p<1\times10^{-5}$, Figures S3C and S3D). See also Figures S3–S6.

successfully predicted 2-strain metabolite dynamics for most combinations of phenotypes (e.g., Nar/Nir + Nar or Nar + Nar) but failed only in the case where Nar strains were cultured with Nir strains (Figures 6A, 6C, S3C, and S3D). The failure of our model predictions in Nar + Nir communities followed the common pattern that the rate of nitrate reduction was slower than expected (bottom row, Figures 6A and S6). We speculate that this failure of the model to predict metabolite dynamics in Nar + Nir communities was caused by excretion of nitric oxide by the Nir strain. Nitric oxide can be cytotoxic (Braun and Zumft, 1991), which may explain slower rates of nitrate reduction for Nar strains. For further exploration of this phenomenon, see the discussion section.

Predicting metabolite dynamics in larger communities

Next, we asked whether dynamical metabolic phenotypes measured from monocultures could be used to predict metabolite dynamics in 3–5-strain communities. We applied the additive model to predicting the nitrate and nitrite dynamics in 81 combinations of 3 strains, 21 combinations of 4 strains, and 6 combinations of 5 strains from the 12-strain subset (STAR Methods). As

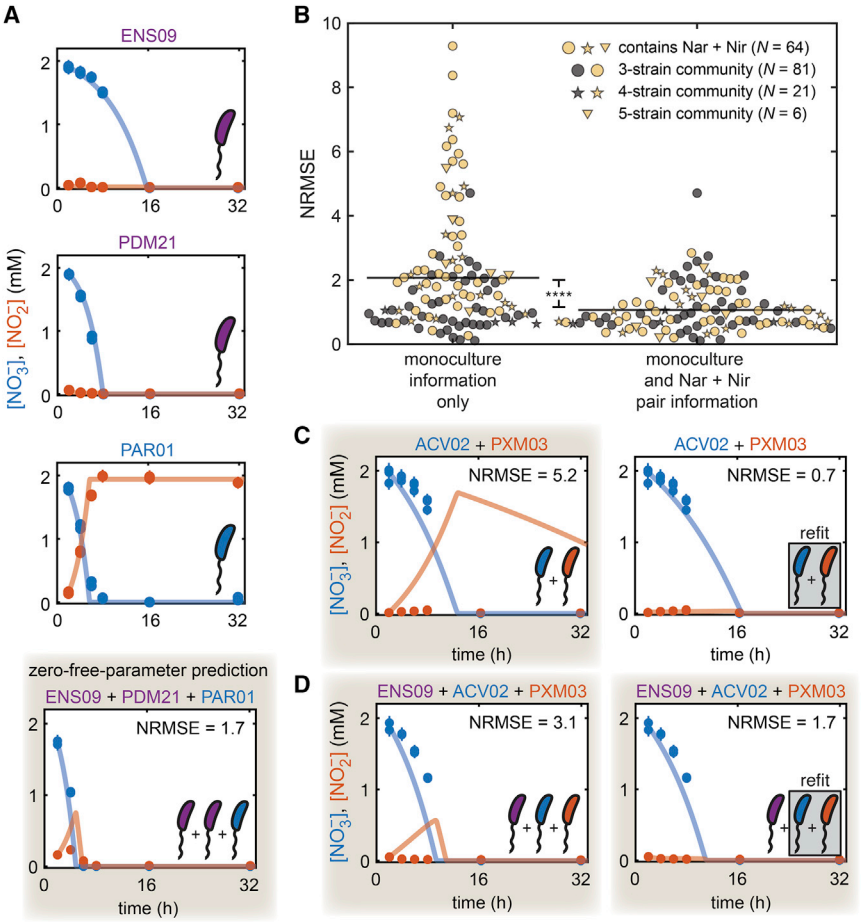

Figure 7. Metabolite dynamics are predictable in 3–5-strain communities

The additive consumer-resource model provides predictions for metabolite dynamics in communities of more than two strains, and these predictions were verified experimentally.

(A) Metabolite dynamics for an example 3-strain (Nar/Nir + Nar/Nir + Nar) community cultured in SDM. The first three panels show metabolite dynamics for each strain cultured individually, and the fourth panel shows the metabolite dynamics of the 3-strain community. Curves show the prediction of the consumer-resource model (Figure 6B) using measured values of consumer-resource model parameters in SDM (not values inferred from genomes).

(B) NRMSE (Equation 12; STAR Methods) values quantifying quality of consumer-resource model predictions for 3–5-strain communities cultured in SDM with nitrate. Yellow symbols denote communities that contain a Nar + Nir pair. Nar + Nir pair culture dynamics were poorly predicted by the model (Figure 6C) and resulted in a high NRMSE for communities containing Nar + Nir pairs (compare yellow and gray symbols). Left and right scatterplots compare predictions from a consumer-resource model using only monoculture data to a coarse-graining approach that describes Nar + Nir pairs as modules within the community (described in C and D). The coarse-graining approach improves the 3–5-strain community predictions; mean NRMSE (black lines) decreases when Nar + Nir pair information is used for prediction (*t*-test, **** denotes $p<10^{-4}$).

(C) Metabolite dynamics for an example Nar + Nir pair cultured in SDM, where curves in the left panel show the prediction of the consumer-resource model using only parameters fit to monocultures, and curves in the right panel show the results of refitting the reduction rates (r_A and r_I) to Nar + Nir pair culture data but leaving yields (γ_A and γ_I) fixed to monoculture values.

(D) Metabolite dynamics for a 3-strain community cultured in SDM containing a Nar/Nir strain and the Nar + Nir pair shown in (C). Curves in the left panel show the prediction of the consumer-resource model using parameters inferred from monoculture experiments for each strain, and curves in the right panel show the prediction when the Nar + Nir pair is treated as a module, with rate parameters refit from pair culture data (right panel in C). NRMSE decreased due to the coarse-graining of the Nar + Nir pair. Panels highlighted in beige denote zero-free-parameter predictions. See also Figures S3 and S5–S7.

with pair cultures, 3–5-strain communities were cultured in SDM with either nitrate or nitrite supplied initially in two separate experimental conditions. In communities that did not contain a Nar + Nir pair (e.g., Figure 7A), we found that prediction accuracy was high (gray symbols, Figures 7B and S3E). This again indicated that in most combinations of phenotypes, community dynamics were predictable from the consumer-resource parameters of each strain in the community. However, in communities that contained a Nar + Nir pair, predictions were relatively poor (yellow symbols, Figures 7B and S3E), suggesting that interactions between Nar and Nir phenotypes that were not captured in the additive model were again driving low prediction accuracy. Finally, we note that the additional error in community metabolite dynamics predictions associated with predicting phenotypes from genomes was typically modest (median increase in NRMSE ≈ 0.5–1.4) for 3–5-strain communities (Figure S5C; STAR Methods).

Correcting for interactions between Nar and Nir strains

To address the impact of interactions between Nar and Nir strains not accounted for by our additive model in 3–5-strain communities, we took a coarse-graining approach. We asked whether the metabolic contributions of Nar + Nir pairs could be treated as modules within larger communities. To do this, we re-fitted nitrate and nitrite reduction rates (r_A, r_I) to pair culture data (cultured in SDM with nitrate) for each Nar + Nir pair, leaving yields fixed (Figures 7C and S7A; STAR Methods). This resulted in effective nitrate and nitrite reduction rates ($\tilde{r}_A$, $\tilde{r}_I$) for each Nar + Nir pair. In every case, we observed that the re-fitted nitrate reduction rates $\tilde{r}_A$ were lower than the monoculture nitrate reduction rates (Figure S7B), demonstrating quantitatively that Nar strains were consistently slowed by the presence of Nir strains. This observation is consistent with the hypothesis of excretion of cytotoxic nitric oxide by the Nir strain.

We then used the re-fitted rates for Nar + Nir pairs to make predictions for communities (cultured in SDM with nitrate) that included such pairs (e.g., Figure 7D). For communities that included multiple Nar + Nir pairs, we developed a simple averaging rule for determining the effective rates from the rates for each Nar + Nir pair present (STAR Methods). For example, in a

Nar + Nar + Nir community, there are two sets of Nar + Nir pair interactions, with a different effective nitrite reduction rate $\tilde{r}_I$ measured for the Nir strain in its interactions with the two Nar strains. In this example, we would take the mean of these two effective reduction rates as the value used for prediction. We found that the metabolite dynamics in 3–5-strain communities containing Nar + Nir pairs were quantitatively well predicted by this coarse-graining approach (yellow symbols, Figure 7B). We concluded that treating Nar + Nir pairs as effective modules within larger communities recovered the predictive power of the additive consumer-resource model.

DISCUSSION

Quantifying the metabolic phenotypes of a diverse library of natural isolates using a consumer-resource model allowed us to take a statistical approach to connecting genotypes to dynamical metabolic phenotypes. The outcome was a sparse mapping from gene content to single-strain metabolite dynamics that exploited conserved correlations between metabolic traits and gene presence, some of which reflect the known mechanistic properties of enzymes in the denitrification pathway. The resource-based modeling formalism then permitted quantitative predictions of community-level metabolite dynamics. As a result, the approach yielded a mapping from genomic structure to metabolite dynamics at the community level for denitrifying bacterial communities.

A key contribution of this study is the demonstration of a quantitative mapping between gene content and metabolic traits for a model metabolic process. One might expect that gene presence and absence is too coarse a genomic feature to predict dynamic metabolic traits and that other genomic features, such as promoter sequences, synteny, or allelic variation, would be necessary to make predictions. We instead found that that the association between gene presence/absence and metabolic traits is strong. This result suggests that selection for specific metabolic traits in bacteria may primarily favor genomes with specific complements of genes (Cordero et al., 2012; Sakoparnig et al., 2021) and that more granular details of the genome, such as promoter sequences or allelic variation, are less important.

At the community level, we found that interactions beyond those described by the additive consumer-resource model are not idiosyncratic but instead exhibit a general pattern (i.e., they occur only when Nar and Nir strains are both present). This suggests that interactions beyond resource competition may exhibit patterns that can be discovered in the laboratory. The fact that community-level metabolite dynamics departed from the additive model in Nar + Nir communities suggests that such interactions may be more likely to occur when specific metabolic processes, such as facilitation via the exchange of a metabolite, are at work.

Improving predictions of community metabolism from genomes

There are some important caveats that apply to our prediction of single-strain metabolic traits from genomes and community-level metabolism from monocultures. For one, by parameterizing metabolite dynamics using a consumer-resource model, we assumed that the model could approximate the metabolic phenotypes of wild isolates. For most of our library (62/79 strains), this approximation worked well, but in some cases (17/79 strains), the model failed for at least some initial conditions (Figures S1J–S1L; Table S5; STAR Methods). These failures may have occurred because the model does not capture phenomena such as the inhibition of reduction rates by reaction products. Going forward, the assumptions of the model could be relaxed by applying methods to learn the appropriate phenotypic parameters directly from the data (Berman et al., 2014; Daniels and Nemenman, 2015).

Although we set out to obtain a diverse strain library for the purpose of mapping genomic variation to dynamic metabolic phenotypes, it is important to note that our library is composed solely of Proteobacteria and does not contain representatives from other phyla. This limitation means that it is unclear whether our regression approach can predict phenotypes of distantly related strains (e.g., gram-positive bacteria). In addition to the 79 strains described in this study, we attempted to assay the denitrification dynamics for three gram-positive Nar strains from the phylum Actinobacteria. We found their reduction rates to be slower than any strain in our library ($\sim$ 0.1 mM/OD/h), resulting in almost negligible nitrate reduction over 64 h. This observation suggests that denitrification phenotypes in clades distant from Proteobacteria may be distinct, with rates that are potentially much slower than what we observed for Proteobacteria. Supporting this idea, denitrification in gram-positive bacteria is poorly understood (Verbaendert et al., 2011), and previous studies that collected phenotypic data similar to ours characterized only Proteobacteria (Lycus et al., 2017; Liu et al., 2013). Therefore, extending our results to more diverse strains would require phenotyping a phylogenetically expanded library.

Considering the broader applicability of our statistical approach, there are some limitations to the types of metabolic processes and interactions that can be readily studied. Denitrification is a well-studied metabolic process, with the relevant enzymes known and easily annotated. Extending our method to less well-studied metabolic traits would require new approaches to learn the appropriate genomic features from data, since it may be challenging in those contexts to choose genes based on mechanistic knowledge. High-throughput mutant screens on wild isolates, for instance, via barcoded transposon mutant libraries (Price et al., 2018), could be used to discover unannotated or poorly annotated genes that are important for metabolic traits and potentially useful as predictors for metabolic phenotypes (Vaccaro et al., 2016).

Bridging the gap between the synthetic communities studied here and communities in the wild will require engaging with the chemical and spatial complexity of natural denitrifying communities. First, it is unclear whether the additive and non-additive interactions described here are relevant to wild communities. One way to determine the relevance of these interactions would be to measure co-occurrence between genotypes in natural contexts. Second, it remains to be seen how our approach generalizes to the complex nutrient environments, such as mixtures of organic carbon sources (Tiedje et al., 1982), that are characteristic of natural communities. One approach to this problem would be to quantify nitrate and nitrite dynamics directly in soils and ask whether gene content can predict metabolite dynamics in this

context. Finally, denitrification in nature occurs in the presence of other metabolic processes, where it often depends on nitrate from nitrifiers and competes with dissimilatory nitrate reduction to ammonia for electron acceptors (Tiedje et al., 1982). Extending the approach taken here to a broader ecological context that includes other metabolic fluxes is an important avenue to pursue.

Applying predictions of community metabolism from genomes

At the single-strain level, the apparent mechanistic relevance of the regression coefficients in this study suggests that a statistical approach, coupled with large-scale culturing and phenotyping on libraries of isolates (Connon and Giovannoni, 2002; Kehe et al., 2019), can be exploited to discover the salient features of genomes that determine community metabolism. Higher-throughput measurements will enable a more detailed investigation of genomic features, allowing us to extend our statistical approach to variation in gene sequences and synteny.

Further, statistical predictions similar to those employed here could be used to help specify constraint-based metabolic models. Constraint-based metabolic models are refined using experimental measurements of metabolic traits (Norsigian et al., 2020), but measuring these traits is challenging, especially for unculturable taxa or strains that are difficult to isolate from complex communities. Since our approach enables the prediction of metabolic phenotypes from genomes, these predictions could be used to refine constraint-based models of metabolic networks using genomic data alone and, thus, circumventing the need to experimentally measure metabolic phenotypes.

At the community level, our approach could eventually enable the prediction of metabolite dynamics in communities where gene presence and absence for individual genomes is known (Sieber et al., 2018). Soils and host-associated communities typically contain hundreds of bacterial taxa; therefore, it may be necessary to test the predictive power of the consumer-resource formalism in communities of many taxa. However, data from soils suggest that denitrification may occur locally, on 10–20 μm grains (Lensi et al., 1995). At this small scale, it is possible that communities are composed of just a few strains. If this is indeed the case, our results for communities of 2–5 strains (Figures 6 and 7) might apply to denitrifying communities in soil.

Departures from model predictions in Nar + Nir communities

It is striking that communities containing both Nar and Nir phenotypes departed from the expectation of an additive consumer-resource model (Figures 6C and 7B). We proposed that the inhibition of nitrate reduction in Nar + Nir communities may be caused by nitric oxide produced by the Nir strains. Consistent with this hypothesis, the most strongly inhibited Nar strains (PDM12 and PNT03, Figure S7) lack nitric oxide reductase (Figure 4A); therefore, they likely cannot alleviate this toxicity. In addition, the strongly inhibited Nar strains possess the periplasmic nitrate reductase (Figure 2B), which is exposed to the toxic effects of extracellular nitric oxide, whereas the weakly inhibited Nar strain ACV02 possesses the membrane-bound nitrate reductase, which is shielded from nitric oxide in the cytoplasm. Although Nir strains possess nitric oxide reductase and, therefore, could alleviate toxicity by reducing nitric oxide to nitrous oxide, Nir strains often transiently accumulate nitric oxide transiently (Lycus et al., 2017). Consistent with this idea, when we measured relative abundances of Nar and Nir strains in co-culture, we observed smaller fractions of Nar strains relative to our model predictions in most cases (Figure S4B).

To describe metabolite dynamics in communities where both Nar and Nir strains were present, we chose not to expand our modeling formalism to include our hypothesized mechanism of Nar strain inhibition. Instead, we used measurements from Nar + Nir pair cultures to describe community-level metabolite dynamics (Figure 7). The advantage of this approach was to maintain a small number of model parameters, but it came at the expense of mechanistic interpretation. Another possible disadvantage of our approach was the challenge of modeling communities with multiple Nar and Nir pairs. However, we found that a simple averaging method (STAR Methods) succeeded in describing community metabolite dynamics, even when multiple Nar + Nir pairs were present in communities of 3–5 strains (Figure 7B).

We note that Nar + Nir pair cultures are metabolically distinct from Nar/Nir monocultures, in that the former splits the denitrification pathway across two genomes resulting in obligate cross-feeding. It is notable that our model fails only in the case where cross-feeding is required, suggesting that our formalism is most relevant for competitive interactions and that accurately predicting obligate cross-feeding from monoculture information alone may require additional parameters. The ecological context of denitrification pathway splitting at nitrite reduction is believed to be associated with environmental pH, with low pH favoring a split pathway. This hypothesis comes from a previous study (Lilja and Johnson, 2016) showing that the transient accumulation of nitrite during denitrification can be reduced by segregating the processes of nitrate and nitrite reduction across genomes. Reducing transient nitrite accumulation is advantageous in low pH environments, where nitrite forms toxic intermediates (Lilja and Johnson, 2016). Because we observe Nar + Nir communities escaping the transient accumulation of nitrite (Figures 6A and S6), our results are consistent with splitting of the denitrification pathway at nitrite reduction as an adaptation to acidic environments.

CONCLUSION

We find it striking that a statistical approach can uncover a simple relationship between gene content and metabolite dynamics in communities of diverse wild isolates. It is our hope that future work can leverage this approach to understand and predict the metabolic activity of microbial communities in natural settings.

Limitations of the study

We assumed that metabolic phenotypes can be captured by a consumer-resource model, an assumption that breaks down for a fraction of our isolates and limits the direct applicability of our approach to strains and processes that can be modeled

using a simple phenomenology. For example, our modeling formalism works well when the electron acceptor is limiting but may fail when the donor (organic carbon) is limiting.

Our regression approach exploits correlations between genotype and phenotype to make predictions. To some extent, these correlations reflect conserved phenotypic impact of certain genes, but phylogenetic correlation also plays a role. Therefore, we do not expect the regression to make causal predictions of the impact of single-gene knockout mutations on phenotypes.

Our library of isolates comprises strains from the phylum Proteobacteria. We do not expect our results to generalize to distantly related denitrifiers in other phyla, such as gram-positive bacteria. Expanding the library is likely necessary to predict phenotypes of distantly related strains.

Our approach has been demonstrated for comparatively simple nutrient conditions in well-mixed conditions. It remains to be seen how well this statistical approach will work in natural contexts, where spatial structure and complex chemical environments are present.

STAR★METHODS

Detailed methods are provided in the online version of this paper and include the following:

- KEY RESOURCES TABLE
- RESOURCE AVAILABILITY
  - Lead contact
  - Materials availability
  - Data and code availability
- EXPERIMENTAL MODEL AND SUBJECT DETAILS
  - Strains
  - Isolation of denitrifying bacteria from soils
  - Defined growth medium
  - Denitrifying conditions
- METHOD DETAILS
  - Assay of nitrate and nitrite
  - Denitrification dynamics experiments
  - Whole genome sequencing and annotation
  - Phylogenetic classification of strains
  - Measuring relative abundances and contamination
- QUANTIFICATION AND STATISTICAL ANALYSIS
  - Consumer-resource model for metabolite dynamics
  - Inferring phenotypic parameters from data
  - Regressing SDM phenotypes onto denitrification gene content
  - Characterizing phylogenetic correlation
  - Evaluating randomly-selected genes as predictors
  - Evaluating alternative genomic predictors
  - Regressing ADM phenotypes onto denitrification gene content
  - Predicting community metabolic dynamics
  - Correcting for Nar + Nir interactions

SUPPLEMENTAL INFORMATION

Supplemental information can be found online at https://doi.org/10.1016/j.cell.2021.12.036.

ACKNOWLEDGMENTS

We thank Laura Troyer for assistance with isolating bacterial strains and Elizabeth Ujhelyi and Annette Wells for assistance with sequencing. We acknowledge Cameron Pittelkow for access to corn and soybean fields in Savoy, Illinois, and the laboratory of Julie Zilles for providing the bacterial strain *Paracoccus denitrificans* ATCC 19367. We also thank Rama Ranganathan, David Pincus, James Sethna, William Metcalf, Jun Song, Sara Clifton, and members of the Kuehn laboratory and Mani group for helpful discussions. This work was supported by the National Science Foundation Division of Emerging Frontiers EF 2025293 (S.K.) and EF 2025521 (M.M.), the National Science Foundation Physics Frontiers Center Program PHY 0822613 and PHY 1430124 (S.K.), James S. McDonnell Foundation Postdoctoral Fellowship Award 220020499 (K.G.), and the Simons Foundation Investigator Award 597491 (M.M.).

AUTHOR CONTRIBUTIONS

K.G.: conceptualization, experimental design, data collection, formal analysis, coding, writing–original draft, and writing–review & editing. D.P.: data collection. M.M.: conceptualization, formal analysis, writing – review & editing, supervision, and funding acquisition. S.K.: conceptualization, experimental design, formal analysis, writing–original draft, writing–review & editing, supervision, and funding acquisition.

DECLARATION OF INTERESTS

The authors declare no competing interests.

Received: January 22, 2021
Revised: July 16, 2021
Accepted: December 21, 2021
Published: January 26, 2022

REFERENCES

Abraham, Z.H.L., Lowe, D.J., and Smith, B.E. (1993). Purification and characterization of the dissimilatory nitrite reductase from *Alcaligenes xylosoxidans subsp*. xylosoxidans (N.C.I.M.B. 11015): evidence for the presence of both type 1 and type 2 copper centres. Biochem. J. *295*, 587–593.

Anantharaman, K., Brown, C.T., Hug, L.A., Sharon, I., Castelle, C.J., Probst, A.J., Thomas, B.C., Singh, A., Wilkins, M.J., Karaoz, U., et al. (2016). Thousands of microbial genomes shed light on interconnected biogeochemical processes in an aquifer system. Nat. Commun. *7*, 13219.

Bankevich, A., Nurk, S., Antipov, D., Gurevich, A.A., Dvorkin, M., Kulikov, A.S., Lesin, V.M., Nikolenko, S.I., Pham, S., Prjibelski, A.D., et al. (2012). SPAdes: a new genome assembly algorithm and its applications to single-cell sequencing. J. Comput. Biol. *19*, 455–477.

Beccari, M., Passino, R., Ramadori, R., and Tandoi, V. (1983). Kinetics of dissimilatory nitrate and nitrite reduction in suspended growth culture. J. Water Pollut. Control Fed. *55*, 58–64.

Bell, L.C., Richardson, D.J., and Ferguson, S.J. (1990). Periplasmic and membrane-bound respiratory nitrate reductases in *Thiosphaera pantotropha*: the periplasmic enzyme catalyzes the first step in aerobic denitrification. FEBS Lett. *265*, 85–87.

Berman, G.J., Choi, D.M., Bialek, W., and Shaevitz, J.W. (2014). Mapping the stereotyped behaviour of freely moving fruit flies. J. R. Soc. Interface *11*, 20140672.

Besson, S., Carneiro, C., Moura, J.J., Moura, I., and Fauque, G. (1995). A cytochrome cd1-type nitrite reductase isolated from the marine denitrifier *Pseudomonas nautica* 617: purification and characterization. Anaerobe *1*, 219–226.

Bolger, A.M., Lohse, M., and Usadel, B. (2014). Trimmomatic: a flexible trimmer for Illumina sequence data. Bioinformatics *30*, 2114–2120.

Braun, C., and Zumft, W.G. (1991). Marker exchange of the structural genes for nitric oxide reductase blocks the denitrification pathway of *Pseudomonas stutzeri* at nitric oxide. J. Biol. Chem. *266*, 22785–22788.

Brettin, T., Davis, J.J., Disz, T., Edwards, R.A., Gerdes, S., Olsen, G.J., Olson, R., Overbeek, R., Parrello, B., Pusch, G.D., et al. (2015). RASTtk: a modular and extensible implementation of the RAST algorithm for building custom annotation pipelines and annotating batches of genomes. Sci. Rep. *5*, 8365.

Canfield, D.E., Glazer, A.N., and Falkowski, P.G. (2010). The evolution and future of earth's nitrogen cycle. Science *330*, 192–196.

Cermak, N., Datta, M.S., and Conwill, A. (2020). Rapid, inexpensive measurement of synthetic bacterial community composition by Sanger sequencing of amplicon mixtures. iScience *23*, 100915.

Claus, G., and Kutzner, H. (1985). Physiology and kinetics of autotrophic denitrification by *Thiobacillus denitrificans*. Appl. Microbiol. Biotechnol. *22*, 283–288.

Connon, S.A., and Giovannoni, S.J. (2002). High-throughput methods for culturing microorganisms in very-low-nutrient media yield diverse new marine isolates. Appl. Environ. Microbiol. *68*, 3878–3885.

Cordero, O.X., Ventouras, L.A., DeLong, E.F., and Polz, M.F. (2012). Public good dynamics drive evolution of iron acquisition strategies in natural bacterioplankton populations. Proc. Natl. Acad. Sci. USA *109*, 20059–20064.

Coultate, T.P., and Sundaram, T.K. (1975). Energetics of *Bacillus stearothermophilus* growth: molar growth yield and temperature effects on growth efficiency. J. Bacteriol. *121*, 55–64.

Daniels, B.C., and Nemenman, I. (2015). Automated adaptive inference of phenomenological dynamical models. Nat. Commun. *6*, 8133.

Datta, M.S., Sliwerska, E., Gore, J., Polz, M.F., and Cordero, O.X. (2016). Microbial interactions lead to rapid micro-scale successions on model marine particles. Nat. Commun. *7*, 11965.

Denariaz, G., Payne, W.J., and LeGall, J. (1991). The denitrifying nitrite reductase of *Bacillus halodenitrificans*. Biochim. Biophys. Acta Bioenerg. *1056*, 225–232.

Dinçer, A.R., and Kargı, F. (2000). Kinetics of sequential nitrification and denitrification processes. Enzyme Microb. Technol. *27*, 37–42.

Erbilgin, O., Bowen, B.P., Kosina, S.M., Jenkins, S., Lau, R.K., and Northen, T.R. (2017). Dynamic substrate preferences predict metabolic properties of a simple microbial consortium. BMC Bioinformatics *18*, 57.

Falkowski, P.G., Fenchel, T., and Delong, E.F. (2008). The microbial engines that drive earth's biogeochemical cycles. Science *320*, 1034–1039.

Ferguson, S.J., and Richardson, D.J. (2004). The enzymes and bioenergetics of bacterial nitrate, nitrite, nitric oxide and nitrous oxide respiration. In Respiration in Archaea and Bacteria: Diversity of Prokaryotic Respiratory Systems, D. Zannoni, ed. (Springer), pp. 169–206.

Fierer, N., Lauber, C.L., Ramirez, K.S., Zaneveld, J., Bradford, M.A., and Knight, R. (2012). Comparative metagenomic, phylogenetic and physiological analyses of soil microbial communities across nitrogen gradients. ISME J. *6*, 1007–1017.

Forchhammer, J., and Lindahl, L. (1971). Growth rate of polypeptide chains as a function of the cell growth rate in a mutant of *Escherichia coli* 15. J. Mol. Biol. *55*, 563–568.

Fraebel, D.T., Gowda, K., Mani, M., and Kuehn, S. (2020). Evolution of generalists by phenotypic plasticity. iScience *23*, 101678.

Galtier, N., and Lobry, J.R. (1997). Relationships between genomic G+C content, RNA secondary structures, and optimal growth temperature in prokaryotes. J. Mol. Evol. *44*, 632–636.

Glockner, A.B., Jüngst, A., and Zumft, W.G. (1993). Copper-containing nitrite reductase from *Pseudomonas aureofaciens* is functional in a mutationally cytochrome cd1-free background (NirS-) of *Pseudomonas stutzeri*. Arch. Microbiol. *160*, 18–26.

Goddard, A.D., Bali, S., Mavridou, D.A., Luque-Almagro, V.M., Gates, A.J., Dolores Roldán, M., Newstead, S., Richardson, D.J., and Ferguson, S.J. (2017). The *Paracoccus denitrificans* NarK-like nitrate and nitrite transporters-probing nitrate uptake and nitrate/nitrite exchange mechanisms. Mol. Microbiol. *103*, 117–133.

Goddard, A.D., Moir, J.W.B., Richardson, D.J., and Ferguson, S.J. (2008). Interdependence of two NarK domains in a fused nitrate/nitrite transporter. Mol. Microbiol. *70*, 667–681.

Goldford, J.E., Lu, N., Bajić, D., Estrela, S., Tikhonov, M., Sanchez-Gorostiaga, A., Segrè, D., Mehta, P., and Sanchez, A. (2018). Emergent simplicity in microbial community assembly. Science *361*, 469–474.

Gordon, E.H.J., Sjögren, T., Löfqvist, M., Richter, C.D., Allen, J.W., Higham, C.W., Hajdu, J., Fülöp, V., and Ferguson, S.J. (2003). Structure and kinetic properties of *Paracoccus pantotrophus* cytochrome cd1 nitrite reductase with the d1 heme active site ligand tyrosine 25 replaced by serine. J. Biol. Chem. *278*, 11773–11781.

Graf, D.R.H., Jones, C.M., and Hallin, S. (2014). Intergenomic comparisons highlight modularity of the denitrification pathway and underpin the importance of community structure for N2O emissions. PLoS ONE *9*, e114118.

Gurevich, A., Saveliev, V., Vyahhi, N., and Tesler, G. (2013). QUAST: quality assessment tool for genome assemblies. Bioinformatics *29*, 1072–1075.

Harcombe, W.R., Riehl, W.J., Dukovski, I., Granger, B.R., Betts, A., Lang, A.H., Bonilla, G., Kar, A., Leiby, N., Mehta, P., et al. (2014). Metabolic resource allocation in individual microbes determines ecosystem interactions and spatial dynamics. Cell Rep. *7*, 1104–1115.

Hassen, A., Saidi, N., Cherif, M., and Boudabous, A. (1998). Effects of heavy metals on *Pseudomonas aeruginosa* and *Bacillus thuringiensis*. Bioresour. Technol. *65*, 73–82.

Hastie, T., Tibshirani, R., and Friedman, J. (2008). The Elements of Statistical Learning, 2nd Edition (Springer).

Hastie, T., Tibshirani, R.J., and Wainwright, R. (2016). Statistical learning with sparsity. Monographs on Statistics and Applied Probability, *143* (CRC Press).

Haywood-Farmer, E., and Otto, S.P. (2003). The evolution of genomic base composition in bacteria. Evolution *57*, 1783–1792.

Hempfling, W.P., and Mainzer, S.E. (1975). Effects of varying the carbon source limiting growth on yield and maintenance characteristics of *Escherichia coli* in continuous culture. J. Bacteriol. *123*, 1076–1087.

Hessen, D.O., Jeyasingh, P.D., Neiman, M., and Weider, L.J. (2010). Genome streamlining and the elemental costs of growth. Trends Ecol. Evol. *25*, 75–80.

Heylen, K., Gevers, D., Vanparys, B., Wittebolle, L., Geets, J., Boon, N., and De Vos, P. (2006). The incidence of nirS and nirK and their genetic heterogeneity in cultivated denitrifiers. Environ. Microbiol. *8*, 2012–2021.

Heylen, K., Vanparys, B., Wittebolle, L., Verstraete, W., Boon, N., and De Vos, P. (2006). Cultivation of denitrifying bacteria: optimization of isolation conditions and diversity study. Appl. Environ. Microbiol. *72*, 2637–2643.

Human Microbiome Project Consortium (2012). Structure, function and diversity of the healthy human microbiome. Nature *486*, 207–214.

Ikeda, E., Andou, S., Iwama, U., Kato, C., Horikoshi, K., and Tamegai, H. (2009). Physiological roles of two dissimilatory nitrate reductases in the deep-sea denitrifier *Pseudomonas* sp. strain MT-1. Biosci. Biotechnol. Biochem. *73*, 896–900.

Irrazábal, T., Belcheva, A., Girardin, S.E., Martin, A., and Philpott, D.J. (2014). The multifaceted role of the intestinal microbiota in colon cancer. Mol. Cell *54*, 309–320.

Iwasaki, H., and Matsubara, T. (1972). A nitrite reductase from *Achromobacter cyclastes*. J. Biochem. *71*, 645–652.

Jones, C.M., and Hallin, S. (2010). Ecological and evolutionary factors underlying global and local assembly of denitrifier communities. ISME J. *4*, 633–641.

Jones, C.M., Stres, B., Rosenquist, M., and Hallin, S. (2008). Phylogenetic analysis of nitrite, nitric oxide, and nitrous oxide respiratory enzymes reveal a complex evolutionary history for denitrification. Mol. Biol. Evol. *25*, 1955–1966.

Kakutani, T., Watanabe, H., Arima, K., and Beppu, T. (1981). Purification and properties of a copper-containing nitrite reductase from a denitrifying bacterium, *Alcaligenes faecalis* strain S-6. J. Biochem. *89*, 453–461.

Keck, F., Rimet, F., Bouchez, A., and Franc, A. (2016). phylosignal: an R package to measure, test, and explore the phylogenetic signal. Ecol. Evol. *6*, 2774–2780.

Kehe, J., Kulesa, A., Ortiz, A., Ackerman, C.M., Thakku, S.G., Sellers, D., Kuehn, S., Gore, J., Friedman, J., and Blainey, P.C. (2019). Massively parallel screening of synthetic microbial communities. Proc. Natl. Acad. Sci. USA *116*, 12804–12809.

Klitgord, N., and Segrè, D. (2010). Environments that induce synthetic microbial ecosystems. PLoS Comput. Biol. *6*, e1001002.

Kornaros, M., Zafiri, C., and Lyberatos, G. (1996). Kinetics of denitrification by *Pseudomonas denitrificans* under growth conditions limited by carbon and/or nitrate or nitrite. Water Environ. Res. *68*, 934–945.

Kukimoto, M., Nishiyama, M., Murphy, M.E., Turley, S., Adman, E.T., Horinouchi, S., and Beppu, T. (1994). X-ray structure and site-directed mutagenesis of a nitrite reductase from *Alcaligenes faecalis* S-6: roles of two copper atoms in nitrite reduction. Biochemistry *33*, 5246–5252.

Kumar, S., Stecher, G., Li, M., Knyaz, C., and Tamura, K. (2018). MEGA X: molecular evolutionary genetics analysis across computing platforms. F.U. Battistuzzi, ed. *35*, 1547–1549.

Lee, K.H., Park, J.H., Kim, T.Y., Kim, H.U., and Lee, S.Y. (2007). Systems metabolic engineering of *Escherichia coli* for L-threonine production. Mol. Syst. Biol. *3* (149), 149.

Lensi, R., Clays-Josserand, A., and Jocteur Monrozier, L. (1995). Denitrifiers and denitrifying activity in size fractions of a mollisol under permanent pasture and continuous cultivation. Soil Biol. Biochem. *27*, 61–69.

Li, J., Mau, R.L., Dijkstra, P., Koch, B.J., Schwartz, E., Liu, X.A., Morrissey, E.M., Blazewicz, S.J., Pett-Ridge, J., Stone, B.W., et al. (2019). Predictive genomic traits for bacterial growth in culture versus actual growth in soil. ISME J. *13*, 2162–2172.

Lilja, E.E., and Johnson, D.R. (2016). Segregating metabolic processes into different microbial cells accelerates the consumption of inhibitory substrates. ISME J. *10*, 1568–1578.

Liu, B., Mao, Y., Bergaust, L., Bakken, L.R., and Frostegård, A. (2013). Strains in the genus Thauera exhibit remarkably different denitrification regulatory phenotypes. Environ. Microbiol. *15*, 2816–2828.

Liu, M.Y., Liu, M.C., Payne, W.J., and Legall, J. (1986). Properties and electron transfer specificity of copper proteins from the denitrifier *"Achromobacter cycloclastes"*. J. Bacteriol. *166*, 604–608.

Louca, S., Jacques, S.M.S., Pires, A.P.F., Leal, J.S., Srivastava, D.S., Parfrey, L.W., Farjalla, V.F., and Doebeli, M. (2016a). High taxonomic variability despite stable functional structure across microbial communities. Nat. Ecol. Evol. *1*, 15.

Louca, S., Parfrey, L.W., and Doebeli, M. (2016b). Decoupling function and taxonomy in the global ocean microbiome. Science *353*, 1272–1277.

Louca, S., Polz, M.F., Mazel, F., Albright, M.B.N., Huber, J.A., O'Connor, M.I., Ackermann, M., Hahn, A.S., Srivastava, D.S., Crowe, S.A., et al. (2018). Function and functional redundancy in microbial systems. Nat. Ecol. Evol. *2*, 936–943.

Lu, H., Chandran, K., and Stensel, D. (2014). Microbial ecology of denitrification in biological wastewater treatment. Water Res. *64*, 237–254.

Lycus, P., Lovise Bøthun, K., Bergaust, L., Peele Shapleigh, J., Reier Bakken, L., and Frostegård, Å. (2017). Phenotypic and genotypic richness of denitrifiers revealed by a novel isolation strategy. ISME J. *11*, 2219–2232.

Lynch, M. (2006). Streamlining and simplification of microbial genome architecture. Annu. Rev. Microbiol. *60*, 327–349.

Martiny, J.B.H., Jones, S.E., Lennon, J.T., and Martiny, A.C. (2015). Microbiomes in light of traits: a phylogenetic perspective. Science *350*, aac9323.

Masuko, M., Iwasaki, H., Sakurai, T., Suzuki, S., and Nakahara, A. (1984). Characterization of nitrite reductase from a denitrifier, *Alcaligenes* sp. NCIB 11015. A novel copper protein. J. Biochem. *96*, 447–454.

Mathupala, S.P., Kiousis, S., and Szerlip, N.J. (2016). A lab assembled microcontroller-based sensor module for continuous oxygen measurement in portable hypoxia chambers. S.K. Batra, ed. *11*, e0148923.

Medlock, G.L., Carey, M.A., McDuffie, D.G., Mundy, M.B., Giallourou, N., Swann, J.R., Kolling, G.L., and Papin, J.A. (2018). Inferring metabolic mechanisms of interaction within a defined gut microbiota. Cell Syst. *7*, 245–257.e7.

Michalski, W.P., and Nicholas, D. (1985). Molecular characterization of a copper-containing nitrite reductase from *Rhodopseudomonas sphaeroides* forma sp. *denitrificans*. Biochim. Biophys. Acta Protein Struct. Mol. Enzymol. *828*, 130–137.

Mickalide, H., and Kuehn, S. (2019). Higher-order interaction between species inhibits bacterial invasion of a phototroph-predator microbial community. Cell Syst. *9*, 521–533.e10.

Miranda, K.M., Espey, M.G., and Wink, D.A. (2001). A rapid, simple spectrophotometric method for simultaneous detection of nitrate and nitrite. Nitric Oxide *5*, 62–71.

Moir, J.W.B., and Wood, N.J. (2001). Nitrate and nitrite transport in bacteria. Cell. Mol. Life Sci. *58*, 215–224.

Molina, N., and Nimwegen, E. van. (2009). Scaling laws in functional genome content across prokaryotic clades and lifestyles. Trends Genet. *25*, 243–247.

Monod, J. (1949). The growth of bacterial cultures. Annu. Rev. Microbiol. *3*, 371–394.

Mori, M., Hwa, T., Martin, O.C., De Martino, A., and Marinari, E. (2016). Constrained allocation flux balance analysis. PLoS Comput. Biol. *12*, e1004913.

Nichols, R.J., Sen, S., Choo, Y.J., Beltrao, P., Zietek, M., Chaba, R., Lee, S., Kazmierczak, K.M., Lee, K.J., Wong, A., et al. (2011). Phenotypic landscape of a bacterial cell. Cell *144*, 143–156.

Nikel, P.I., Fuhrer, T., Chavarría, M., Sánchez-Pascuala, A., Sauer, U., and de Lorenzo, V. (2021). Reconfiguration of metabolic fluxes in *Pseudomonas putida* as a response to sub-lethal oxidative stress. ISME J. *15*, 1751–1766.

Norsigian, C.J., Fang, X., Seif, Y., Monk, J.M., and Palsson, B.O. (2020). A workflow for generating multi-strain genome-scale metabolic models of prokaryotes. Nat. Protoc. *15*, 1–14.

Orth, J.D., Thiele, I., and Palsson, B.Ø. (2010). What is flux balance analysis? Nat. Biotechnol. *28*, 245–248.

Péquignot, C., Larroche, C., and Gros, J.B. (1998). A spectrophotometric method for determination of bacterial biomass in the presence of a polymer. Biotechnol. Tech. *12*, 899–903.

Perisin, M., Vetter, M., Gilbert, J.A., and Bergelson, J. (2016). 16Stimator: statistical estimation of ribosomal gene copy numbers from draft genome assemblies. ISME J. *10*, 1020–1024.

Phaiboun, A., Zhang, Y., Park, B., and Kim, M. (2015). Survival kinetics of starving bacteria is biphasic and density-dependent. PLoS Comput. Biol. *11*, e1004198.

Price, M.N., Wetmore, K.M., Waters, R.J., Callaghan, M., Ray, J., Liu, H., Kuehl, J.V., Melnyk, R.A., Lamson, J.S., Suh, Y., et al. (2018). Mutant phenotypes for thousands of bacterial genes of unknown function. Nature *557*, 503–509.

Pruesse, E., Peplies, J., and Glöckner, F.O. (2012). SINA: accurate high-throughput multiple sequence alignment of ribosomal RNA genes. Bioinformatics *28*, 1823–1829.

Rodionov, D.A., Dubchak, I.L., Arkin, A.P., Alm, E.J., and Gelfand, M.S. (2005). Dissimilatory metabolism of nitrogen oxides in bacteria: comparative reconstruction of transcriptional networks. PLoS Comput. Biol. *1*, e55, 17.

Roller, B.R.K., Stoddard, S.F., and Schmidt, T.M. (2016). Exploiting rRNA operon copy number to investigate bacterial reproductive strategies. Nat. Microbiol. *1*, 16160.

Rosenberger, R.F., and Elsden, S.R. (1960). The yields of Streptococcus faecalis grown in continuous culture. J. Gen. Microbiol. *22*, 726–739.

Sakoparnig, T., Field, C., and Nimwegen, E. van. (2021). Whole genome phylogenies reflect the distributions of recombination rates for many bacterial species. eLife *10*, e65366.

Sanchez-Gorostiaga, A., Bajić, D., Osborne, M.L., Poyatos, J.F., and Sanchez, A. (2019). High-order interactions distort the functional landscape of microbial consortia. PLoS Biol. *17*, e3000550.

Sawada, E., Toshio, S., and Kitamura, H. (1978). Purification and properties of a dissimilatory nitrite reductase of a denitrifying phototrophic bacterium. Plant Cell Physiol. *19*, 1339–1351.

Sawhney, V., and Nicholas, D.J.D. (1978). Sulphide-linked nitrite reductase from *Thiobacillus denitrificans* with cytochrome oxidase activity: purification and properties. J. Gen. Microbiol. *106*, 119–128.

Schober, A.F., Mathis, A.D., Ingle, C., Park, J.O., Chen, L., Rabinowitz, J.D., Junier, I., Rivoire, O., and Reynolds, K.A. (2019). A two-enzyme adaptive unit within bacterial folate metabolism. Cell Rep. *27*, 3359–3370.e7.

Scott, M., Gunderson, C.W., Mateescu, E.M., Zhang, Z., and Hwa, T. (2010). Interdependence of cell growth and gene expression: origins and consequences. Science *330*, 1099–1102.

Seitzinger, S., Harrison, J.A., Böhlke, J.K., Bouwman, A.F., Lowrance, R., Peterson, B., Tobias, C., and Van Drecht, G. (2006). Denitrification across landscapes and waterscapes: a synthesis. Ecol. Appl. *16*, 2064–2090.

Sela, I., Wolf, Y.I., and Koonin, E.V. (2019). Selection and genome plasticity as the key factors in the evolution of bacteria. Phys. Rev. X *9*, 031018.

Shou, W., Ram, S., and Vilar, J.M.G. (2007). Synthetic cooperation in engineered yeast populations. Proc. Natl. Acad. Sci. USA *104*, 1877–1882.

Si, Y.-Y., Xu, K.-H., Yu, X.-Y., Wang, M.-F., and Chen, X.-H. (2019). Complete genome sequence of *Paracoccus denitrificans* ATCC 19367 and its denitrification characteristics. Can. J. Microbiol. *65*, 486–495.

Sieber, C.M.K., Probst, A.J., Sharrar, A., Thomas, B.C., Hess, M., Tringe, S.G., and Banfield, J.F. (2018). Recovery of genomes from metagenomes via a dereplication, aggregation and scoring strategy. Nat. Microbiol. *3*, 836–843.

Stein, L.Y., and Klotz, M.G. (2016). The nitrogen cycle. Curr. Biol. *26*, R94–R98.

Stewart, V., Lu, Y., and Darwin, A.J. (2002). Periplasmic nitrate reductase (NapABC enzyme) supports anaerobic respiration by *Escherichia coli* K-12. J. Bacteriol. *184*, 1314–1323.

Strohm, T.O., Griffin, B., Zumft, W.G., and Schink, B. (2007). Growth yields in bacterial denitrification and nitrate ammonification. Appl. Environ. Microbiol. *73*, 1420–1424.

Subramanian, S., Huq, S., Yatsunenko, T., Haque, R., Mahfuz, M., Alam, M.A., Benezra, A., DeStefano, J., Meier, M.F., Muegge, B.D., et al. (2014). Persistent gut microbiota immaturity in malnourished Bangladeshi children. Nature *510*, 417–421.

Taylor, J., and Tibshirani, R.J. (2015). Statistical learning and selective inference. Proc. Natl. Acad. Sci. USA *112*, 7629–7634.

Tiedje, J.M., Sexstone, A.J., Myrold, D.D., and Robinson, J.A. (1982). Denitrification: ecological niches, competition and survival. Antonie van Leeuwenhoek *48*, 569–583.

Timkovich, R., Dhesi, R., Martinkus, K.J., Robinson, M.K., and Rea, T.M. (1982). Isolation of *Paracoccus denitrificans* cytochrome cd1: comparative kinetics with other nitrite reductases. Arch. Biochem. Biophys. *215*, 47–58.

Vaccaro, B.J., Thorgersen, M.P., Lancaster, W.A., Price, M.N., Wetmore, K.M., Poole, F.L., Deutschbauer, A., Arkin, A.P., and Adams, M.W. (2016). Determining roles of accessory genes in denitrification by mutant fitness analyses. Appl. Environ. Microbiol. *82*, 51–61.

Van Alst, N.E., Sherrill, L.A., Iglewski, B.H., and Haidaris, C.G. (2009). Compensatory periplasmic nitrate reductase activity supports anaerobic growth of *Pseudomonas aeruginosa* PAO1 in the absence of membrane nitrate reductase. Can. J. Microbiol. *55*, 1133–1144.

Verbaendert, I., De Vos, P., Boon, N., and Heylen, K. (2011). Denitrification in Gram-positive bacteria: an underexplored trait. Biochem. Soc. Trans. *39*, 254–258.

Ward, D.M., Bateson, M.M., Ferris, M.J., Kühl, M., Wieland, A., Koeppel, A., and Cohan, F.M. (2006). Cyanobacterial ecotypes in the microbial mat community of Mushroom Spring (Yellowstone National Park, Wyoming) as species-like units linking microbial community composition, structure and function. Philos. Trans. R. Soc. Lond. B Biol. Sci. *361*, 1997–2008.

Warnecke-Eberz, U., and Friedrich, B. (1993). Three nitrate reductase activities in *Alcaligenes eutrophus*. Arch. Microbiol. *159*, 405–409.

White, D., Drummond, J., and Fuqua, C. (2012). The Physiology and Biochemistry of Prokaryotes, 4th Edition (Oxford University Press).

Widder, S., Allen, R.J., Pfeiffer, T., Curtis, T.P., Wiuf, C., Sloan, W.T., Cordero, O.X., Brown, S.P., Momeni, B., Shou, W., et al. (2016). Challenges in microbial ecology: building predictive understanding of community function and dynamics. ISME J. *10*, 2557–2568.

Zumft, W.G. (1997). Cell biology and molecular basis of denitrification. Microbiol. Mol. Biol. Rev. *61*, 533–616.

STAR★METHODS

KEY RESOURCES TABLE

REAGENT or RESOURCE	SOURCE	IDENTIFIER
Bacterial and virus strains		
Bacterial isolates	This paper	Table S2
Paracoccus denitrificans	ATCC	Cat#19367
Biological samples		
Soils for bacterial isolation	This paper	Table S1
Chemicals, peptides, and recombinant proteins		
N-(1-Naphthyl)ethylenediamine dihydrochloride	Sigma-Aldrich	Cat#222488-10G
Sulfanilamide	Sigma-Aldrich	Cat#S9251-100G
Vanadium(III) chloride	Fisher Scientific	Cat#AC197000050
Critical commercial assays		
DNeasy UltraClean Microbial Kit	Qiagen	Cat#12224-250
MiSeq Reagent Kit v3 (600 cycle)	Illumina	Cat#MS-102-3003
Nextera DNA CD Indexes	Illumina	Cat#20018707
Nextera DNA Flex Library Prep Kit	Illumina	Cat#20018704
PhiX Control v3	Illumina	Cat#FC-110-3001
Platinum Hot Start PCR Master Mix	Invitrogen	Cat#13000013
QIAquick PCR Purification Kit	Qiagen	Cat#28106
Qubit dsDNA BR Assay	Invitrogen	Cat#Q32853
Deposited data		
Metabolite dynamics data, consumer-resource parameters, genome annotations	This paper	https://doi.org/10.17605/osf.io/t3prd
Paracoccus denitrificans complete genome	Si et al., 2019	BioProject ID PRJNA513156
Raw sequencing data and draft genome assemblies	This paper	BioProject ID PRJNA660495
Oligonucleotides		
16S rRNA universal primer (27F)	Integrated DNA Technologies	AGAGTTTGATCMTGGCTCAG
16S rRNA universal primer (806R)	Integrated DNA Technologies	GGACTACNVGGGTWTCTAAT
Software and algorithms		
MATLAB R2017B	Mathworks	https://www.mathworks.com/products/matlab.html
R 3.6.1	R Core Team	https://www.r-project.org/
Original code	This paper	https://doi.org/10.17605/osf.io/t3prd
CASEU 0.1.2	Cermak et al., 2020	https://bitbucket.org/DattaManoshi/caseu
MEGA X 10.1.8	Kumar et al., 2018	https://www.megasoftware.net/
phylosignal 1.3	Keck et al., 2016	https://cran.r-project.org/web/packages/phylosignal
QUAST 5.02	Gurevich et al., 2013	https://github.com/ablab/quast
RAST	Brettin et al., 2015	http://rast.theseed.org
selectiveInference 1.2.5	Taylor and Tibshirani, 2015	https://cran.r-project.org/web/packages/selectiveInference/
SILVA ACT	Pruesse et al., 2012	http://www.arb-silva.de/
SPAdes 3.13.0	Bankevich et al., 2012	https://github.com/ablab/spades
Trimmomatic 0.39	Bolger et al., 2014	https://github.com/usadellab/Trimmomatic

(*Continued on next page*)

Continued

REAGENT or RESOURCE	SOURCE	IDENTIFIER
Other		
Anaerobic glove box	Coy Laboratory Products	Cat#7601-110/220
Breathe-Easier membranes	Diversified Biotech	Cat#BERM-2000
Deepwell plates	Axygen	Cat#PDW20C
Digital mass flow controllers	Sierra Instruments	SmartTrak 50
High-throughput DNA sequencing system	Illumina	MiSeq
Liquid handling robot	Formulatrix	Mantis
Microplate reader	BMG	CLARIOstar
Plate shaker	Troemner	Talboys Professional 1000MP

RESOURCE AVAILABILITY

Lead contact

Further information and requests for resources should be directed to and will be fulfilled by the lead contact, Seppe Kuehn (seppe.kuehn@gmail.com).

Materials availability

Strains isolated in this study will be made available on request. No new or unique reagents were generated in this study.

Data and code availability

- Raw sequencing data and draft genome assemblies have been deposited to NCBI Sequence Read Archive and NCBI GenBank, respectively. The BioProject ID is listed in the key resources table. Metabolite dynamics data, phenotype data, and RAST annotations of draft assemblies used to infer gene presence and absence have been deposited on Open Science Framework and are publicly available as of the date of publication. The DOI is listed in the key resources table.
- All original code has been deposited at Open Science Framework and is publicly available as of the date of publication. The DOI is listed in the key resources table.
- Any additional information required to reanalyze the data reported in this paper is available from the lead contact upon request.

EXPERIMENTAL MODEL AND SUBJECT DETAILS

Strains

The bacterial strains and isolates used in this study are listed in Table S1.

Isolation of denitrifying bacteria from soils

Denitrifying bacteria were isolated from soil samples following a modified version of the protocol developed by Lycus et al. (Lycus et al., 2017). 5–10 g soil samples were collected from local prairie and forest environments, agricultural land, and manicured lawns (Table S2). Samples were stored separately in 50 mL centrifuge tubes at 4°C for no longer than three months before use.

Each soil sample was prepared for isolation by combining with 25 mL PBS (pH 7.4) and 5–10 g sterile 4 mm glass beads. Additionally 0.5 mL cycloheximide solution (10 mg/mL) and 20 μL nystatin solution (25 mg/mL) were added to prevent fungal growth. In certain rounds of isolation (Table S2), sterile $NaNO_2$ solution (1 M) was added to enrich for nitrite-reducing bacteria. Tubes were then vortexed (Vortex-Genie 2) at high speed for 1 min to homogenize the samples. In certain rounds of isolation (Table S2), homogenized soils were incubated at either room temperature or 30°C for up to two weeks, and then briefly re-vortexed before further processing.

Supernatants from homogenized soils were then diluted and plated. After vortexing, large particles in homogenized soil samples were allowed to settle for 20–30 min before transferring 1 mL of supernatant to sterile 1.7 mL microcentrifuge tubes. Soil supernatants were then serially-diluted in PBS to obtain 10^{-4}-fold and 10^{-5}-fold dilutions. 100 μL of the 10^{-4} and 10^{-5} soil supernatant dilutions were plated on 1/10X tryptic soy agar (1/10X TSA, 1.5 g/L tryptone, 0.5 g/L soytone, 0.5 g/L NaCl, 15 g/L agar), with two replicates for each dilution. Plates were then incubated under aerobic conditions at 30°C for 48 h.

Colonies from plated soil supernatants were picked and streaked to purity. Plated soil dilutions were examined for growth after incubation. Plates showing little or no growth were incubated for an additional 24–48 h until colonies appeared. Plates showing likely fungal growth were discarded. For each set of plates derived from a soil sample, 5–15 well-separated colonies were picked and streaked to purity on 1/10X TSA plates, again incubating at 30°C. Whenever possible, colonies were selected which varied in morphology, size, and color, in order to enhance the diversity of the isolate collection.

Bacterial isolates were assayed for nitrate and/or nitrite-reduction capability. Isolates were first cultured aerobically in sterile 96-deepwell plates (Axygen PDW20C) containing 1 mL per well 1/10X tryptic soy broth liquid medium (1/10X TSB), inoculated directly from streak plate colonies. Deepwell plates were sealed with a gas-permeable membrane (Diversified Biotech BERM-2000) and incubated/shaken at 30°C/950RPM (Talboys Professional 1000MP) for 48 h. 1 μL of each dense aerobic culture was then passaged to fresh 96-deepwell plates containing 1 mL per well 1/10X TSB supplemented with either sterile $NaNO_3$ or $NaNO_2$ solution (1 M) to yield a final concentration of 2 mM NO_3^- or NO_2^-, with two replicates of each condition per isolate. Plates were sealed with gas-permeable membranes (Diversified Biotech BEM-1) and transferred to an N_2-purged anaerobic glove box (Coy Laboratory Products 7601-110/220). Plates were incubated/shaken at 30°C/950RPM for 48 h under anaerobic conditions. After incubation, plates were sampled to determine endpoint concentrations of nitrate and nitrite.

Nitrate and nitrite-reduction capability for each isolate was determined by comparing endpoint concentrations of NO_3^- and NO_2^- in each culture with the corresponding concentrations in uninoculated controls. Isolates showing lower endpoint levels of nitrate and/or nitrite than the uninoculated controls were identified as nitrate and/or nitrite reducers, respectively. Strains that performed both nitrate and nitrite reduction were classified as "Nar/Nir" strains, while strains that performed nitrate or nitrite reduction only were classified as "Nar" or "Nir" strains, respectively. These isolates were cryopreserved by mixing 500 μL of saturated culture grown in 1/10X TSB under aerobic conditions with 500 μL filter-sterilized 50% glycerol solution in 2 mL cryotubes, and freezing/storing at -80°C.

Defined growth medium

In order to eliminate the possibility of fermentative metabolism in subsequent (post-isolation) denitrification experiments, defined growth media based on the medium designed by Heylen et al. (2006) for the cultivation of diverse denitrifying bacteria were used (Table S4). A succinate-defined medium (SDM) that contained 25 mM succinate (100 mM C) as the sole (non-fermentable) carbon source was used for most denitrification experiments. The medium also contained trace metals and vitamins, 15 mM ammonium as the assimilatory nitrogen source, and a 40 mM phosphate buffer with the final medium pH adjusted to 7.3. It was expected that nitrate and nitrite assimilation were inhibited by high concentrations of ammonia (Zumft, 1997). Additionally an acetate defined medium (ADM) containing 50 mM acetate (100 mM C) in place of succinate was used for some experiments, with all other medium components unchanged. In ADM, acetate served as the sole non-fermentable carbon source.

In denitrification experiments using defined media, nitrate or nitrite was provided in at most 2 mM concentrations, and it was expected that growth was nitrate and/or nitrite limited. This expectation was corroborated by measurements of endpoint biomass densities for strains in axenic culture, in which typically higher biomass densities were observed in conditions where 2 mM nitrate or nitrite was supplied (and completely reduced) than when 1 mM was supplied. Moreover, in a previous study, growth experiments using a mineral medium containing 5 mM acetate (10 mM C), 3.7 mM ammonia, and 1.5 mM phosphate, demonstrated that nitrate and nitrite were limiting at up to a 5 mM concentration for the strains *Paracoccus denitrificans* and *Pseudomonas stutzeri* (Strohm et al., 2007). For comparison, SDM and ADM supplied carbon, ammonia, and phosphate in significantly greater concentrations, and nitrate and nitrite in lower concentrations, further supporting the claim that nitrate and/or nitrite were growth limiting under denitrifying conditions.

Denitrifying isolates were screened for growth on SDM under aerobic conditions by first growing axenically from freezer stocks in 1/10X TSB, passaging 1:300 into 300 μL SDM in 96-well plates (with two replicates per isolate), and culturing at 30°C for 48 h. Endpoint optical density was measured to assess growth on SDM using a microplate reader (BMG CLARIOstar). Denitrifying isolates unable to grow on SDM (approximately 36% of isolates) were excluded from further experimentation and analysis. Strains that grew on SDM were also further screened for growth on ADM (Table S1).

Denitrifying conditions

Post-isolation denitrification experiments were performed in a vinyl glove box (Coy Laboratory Products 7601-110/220) purged of oxygen with a 99%/1% N_2/CO_2 gas mixture. Provision of CO_2 was necessary to support the growth of cultures from low initial biomass densities ($OD600_0 \ll 0.01$), likely due to the CO_2-fixation requirements of core anaplerotic metabolism (White et al., 2012). Gas mixing and a purge rate of 20 SLPM were controlled using digital mass flow controllers (Sierra Instruments SmartTrak 50). Oxygen and CO_2 concentrations inside the glove box were continually monitored using Arduino-attached (Mathupala et al., 2016) optical sensors (SST Sensing LOX-02, Gas Sensing Solutions EXPLORIR-M-20). Gaseous oxygen concentration was maintained around 200 ppm, which was sufficient to prevent growth via aerobic respiration. This was verified using two denitrifying isolates, the Nar strain *Paracoccus* sp. PAR01 and the Nir strain *Pseudomonas* sp. PDM13, which were grown under denitrifying conditions for 64h with and without a suitable electron acceptor (i.e., nitrate for the Nar strain and nitrite for the Nir strain). The Nar strain PAR01 was inoculated at biomass density $OD600_0 = 0.011$ and grew to $OD600_{64} = 0.072$ with nitrate and remained at $OD600_{64} = 0.013$ without nitrate. Similarly, the Nir strain PDM13 was inoculated at biomass density $OD600_0 = 0.010$ and grew to $OD600_{64} = 0.026$ with nitrite and remained at $OD600_{64} = 0.010$ without nitrite.

METHOD DETAILS

Assay of nitrate and nitrite

Concentrations of nitrate and nitrite were measured using a microplate reader (BMG CLARIOstar) following a modified version of the protocol by Miranda et al. (2001), where the conventional Griess assay for detection of nitrite is coupled with the chemical reduction of

nitrate to nitrite using vanadium (III) chloride. Stock solutions of *N*-(1-Napthyl)ethylenediamine dihydrochloride (NEDD), sulfanilamide (SULF, in 5% HCl), and VCl_3 (in 1 M HCl) were prepared and stored as described in Miranda et al. (2001). Griess reagent was freshly prepared on the day of each assay by mixing NEDD and SULF stock solutions with ultrapure H_2O in a 5:5:9 ratio.

Nitrate and nitrite were measured using 10 μL samples of analyte in a 96-well microplate. Nitrite was first quantified by adding 190 μL of Griess reagent to each sample and recording blank-corrected maximum absorbance within the interval 450 to 650 nm, denoted Abs^G_{max}. Then nitrate was chemically reduced to nitrite by adding 50 μL of VCl_3 solution to each sample and incubating at 30°C for 6–7 h, which was sufficient time for complete reduction of nitrate to nitrite. After incubation, the maximum blank-corrected absorbance within the interval 450 to 650 nm, denoted Abs^V_{max}, was recorded to quantify the sum total of nitrate and nitrite in the sample.

Concentrations of nitrate and nitrite were determined using 8-point standard curves. Separate two-fold dilutions of $NaNO_2$ and $NaNO_3$ standards spanning 31 μM–2 mM were prepared, and 10 μL samples of these standards were dispensed in triplicate into a 96-well plate, along with 10 μL samples of ultrapure water that served as blanks. Griess reagents were used as described above to measure nitrite in the $NaNO_2$ standards, and these data were parameterized by fitting the equation:

$$Abs^G_{max}(I) = a_0 + a_1 I + a_2 I^2, \quad \text{(Equation 1)}$$

where I is the concentration of NO_2^-. A quadratic term was included to account for the slight nonlinearity of the absorbance at high values of concentration. Then VCl_3 solution was used as described above to measure nitrate in the $NaNO_3$ standards, and these data were parameterized by fitting the equation:

$$Abs^V_{max}(A) = b_0 + b_1 A + b_2 A^2, \quad \text{(Equation 2)}$$

where A is the concentration of NO_3^-. Standard curves were run in triplicate on each day that an assay was performed.

The nitrate and nitrite concentrations in a new sample, for which Abs^G_{max} and Abs^V_{max} were recorded, were then determined by:

1. Solving Equation 1 to determine I from $Abs^G_{max}(I)$,
2. Solving Equation 2 to determine the quantity $A + I$ from $Abs^V_{max}(A + I)$ (since this step of the assay measures the sum total of nitrate and nitrite in a sample),
3. Subtracting the result of step 1 from the result of step 2 to obtain A.

This approach was validated using mixed standards containing both nitrate and nitrite in a 1:1 ratio, and relative error was found to be typically less than ± 5% for concentrations ≥ 62.5 μM.

In this study, nitrate and nitrite assays were performed directly on samples taken from denitrifying cultures (i.e., without first removing cells via filtration or centrifugation). To verify that neither the presence of cells nor molecules secreted by strains during denitrification interfere with the assay, measurement error was evaluated in standards combined with samples taken from denitrifying cultures of four representative strains. The strains *Achromobacter* sp. ACM01, *Ensifer* sp. ENS09, *Paracoccus denitrificans* ATCC 19367 (PAR19367), and *Pseudomonas* sp. PDM21 were grown in a succinate defined medium under denitrifying conditions from low initial abundance ($OD600_0 \approx 0.01$) for 64 h, by which time cells were in stationary phase ($OD600_{64} = 0.052–0.148$). 10 μL samples of these cultures were then then combined with 10 μL samples of nitrate and nitrite standards and then assayed as described above. In standards containing nitrate or nitrite separately, relative error of the assay was typically less than ± 5% for concentrations ≥ 125 μM, with relative error ± 10% at 62.5 μM. In standards containing mixtures of both nitrate and nitrite in a 1:1 ratio, relative error was again found to be typically less than ± 5% for concentrations ≥ 125 μM, with relative error ± 10% at 62.5 μM. This indicates that presence of cells and/or molecules secreted by strains during denitrification do not appreciably increase measurement error above concentrations of 125 μM.

Denitrification dynamics experiments

Strains were pre-cultured under aerobic conditions (using first broth then defined medium) prior to growth under denitrifying (anaerobic) conditions in defined medium. Strains were first grown axenically to saturation from freezer stocks in 1/5X TSB, then passaged 1:100 into defined medium and again grown to saturation. All pre-cultures were grown in 24-well plates containing 1.7 mL medium per well and incubated/shaken at 30°C/400RPM under aerobic conditions. Since strains in the library vary widely in the time required to grow to saturation in 1/5X TSB and defined medium (12–96 h), inoculation and passaging of strains was timed so that defined medium aerobic cultures would enter stationary phase within 12 h of the start of an experiment in denitrifying conditions.

Experiments to measure the nitrate/nitrite-reduction dynamics of strains in monoculture were performed with multiple initial media and biomass density conditions: (a) 2 mM NO_*^-, $OD600_0 = 0.01$, (b) 1 mM NO_*^-, $OD600_0 = 0.01$, (c) 2 mM NO_*^-, $OD600_0 = 0.001$, where Nar/Nir strains were cultured with NO_3^- and NO_2^- separately (6 conditions total), Nar strains were cultured with NO_3^- (3 conditions total), and Nir strains were cultured with NO_2^- (3 conditions total). Medium containing (separately) 2 mM NO_3^-, 1 mM NO_3^-, 2 mM NO_2^-, and 1 mM NO_2^- were prepared by supplementing fresh defined medium with sterile $NaNO_3$ or $NaNO_2$ (1 M) solutions. Aerobic defined medium pre-cultures were normalized to two levels of optical density ($OD600 \approx 1.2$ and 0.12) by diluting with PBS, and these normalized densities were recorded. 96-deepwell plates containing 1.2 mL of NO_3^- or NO_2^--supplemented defined medium were then

inoculated with 10 μL of density-normalized culture, resulting in OD600 ≈ 0.01 and 0.001 cell density conditions. 2–4 replicates were used for each combination of media and cell density conditions.

Inoculated plates were sealed with gas-permeable membranes (Diversified Biotech BERM-2000) and transferred to an anaerobic glove box for incubation/shaking at 30°C/950RPM. Cultures were manually sampled with a multichannel pipette (10 μL per well) at 2, 4, 6, 8, 16, 32, and 64 h from the start of anaerobic culture. Samples were stored in clean 96-well plates, and immediately sealed (Bio-Rad MSB1001) and frozen at -20°C for later assay of nitrate and nitrite. Additionally, at 64 h, 300 μL per well of culture was sampled into clean 96-well plates and the optical density (pathlength normalized to 1 cm) immediately measured to quantify endpoint biomass density. Strains observed to form excessive cell aggregation (to the extent that quantification of endpoint biomass by optical density was not possible) were at this point excluded from further experimentation and analysis (Table S3).

Additional experiments to measure nitrate/nitrite-reduction dynamics on communities of 2–5 strains (including monoculture controls) were performed in separate 2 mM NO_3^- and 2 mM NO_2^- conditions. Aerobic pre-cultures were normalized to OD600 ≈ 1.2 with PBS. Using liquid handling robotics (Formulatrix Mantis), 96-deepwell plates containing 1.2 mL of 2 mM NO_3^- or NO_2^- SDM was inoculated with 10 μL droplets of density-normalized culture in defined combinations (e.g., a pair community containing strains A and B would be inoculated with separate 10 μL droplets of strain A and strain B). Following inoculation, all culture and sampling details were the same as described above.

Measurements were post-processed to correct for gradual evaporation of H_2O that increased apparent concentrations with time. 3–8 uninoculated controls containing nitrate or nitrite-supplemented medium were used on each culture plate to quantify the effect of evaporation. Raw nitrate and nitrite measurements for cultures were scaled at each time point by the concentration of initially supplied nitrate or nitrite divided by the median concentration across blank measurements at that time point.

Whole genome sequencing and annotation

Denitrifying strains were grown axenically from freezer stocks or plated colonies in 1/10X TSB incubated at 30°C with shaking. Saturated cell cultures were harvested and DNA extracted using the DNeasy UltraClean Microbial Kit (Qiagen). DNA concentrations were quantified using the Qubit dsDNA BR Assay Kit (Invitrogen).

Library preparation for sequencing of DNA extracts was performed using the Nextera DNA Flex Library Prep Kit (Illumina) and the Nextera DNA CD Indexes (Illumina). Barcoded libraries for each strain were pooled in groups of 21–24 strains and quantified using the Qubit dsDNA BR kit and an Agilent 2100 Bioanalyzer (Carver Biotechnology Center, University of Illinois at Urbana-Champaign). Each pooled library was then separately sequenced using a MiSeq Reagent Kit v3 (Illumina, 2 × 300 bp paired-end), with a 12 pM library loading concentration and a 1% spike-in of PhiX Control v3 (Illumina). Sequencing was performed on a locally maintained and operated Illumina MiSeq system.

Raw paired-end reads were trimmed of low-quality regions and Illumina adapters using Trimmomatic 0.39 (Bolger et al., 2014). Trimmed reads were assembled into contigs *de novo* using SPAdes 3.13.0 (Bankevich et al., 2012) with k-mer lengths of 21, 33, 55, 77, 99, and 127 and the error-correction option "careful" enabled. Assembly quality was assessed using QUAST 5.02 (Gurevich et al., 2013). The draft assembly of the laboratory strain *Paracoccus denitrificans* ATCC 19367 was compared to a complete assembly of the same strain by Si et al. (Si et al., 2019), which served as a reference. The comparison indicated a 97.8% genome fraction (percentage of bases in the reference that align to the draft assembly), with one 30.8 kbp relocation misassembly, 7.02 mismatches (sequencing errors or single nucleotide polymorphisms) per 100 kbp, and 0.43 indels per 100 kbp. The draft assembly produced 4635 predicted genes relative to 4644 genes predicted in the reference. The coverage depth of the *P. denitrificans* draft assembly was 32X, compared to a median of 35X for the other strains in the library. Together these analyses suggest that the draft assemblies are likely to cover the vast majority of the protein-coding sequences, with relatively few errors that would affect the inference of gene presence or absence.

Contigs were uploaded for gene annotation on the RAST Server (http://rast.theseed.org) using the RASTtk pipeline (Brettin et al., 2015). Denitrification gene presence and absence information was obtained from annotation files by a text search of gene function labels (Table S6). The NarXL two-component nitrate/nitrite sensing system was considered "present" if a gene encoding the sensor (*narX*) and/or the response regulator (*narL*) were identified in the annotation. Each gene identified as a NarK-type nitrate transporter was classified post-annotation as encoding either a nitrate/H^+ symporter (*narK1*), a nitrate/nitrite antiporter (*narK2*), or a fusion of both transporters (*narK1K2*). This classification was performed by locally aligning each transporter sequence with the *narK1K2* gene previously identified in *Paracoccus denitrificans* PD1222 (Goddard et al., 2017), for which the N-terminal domain has been identified to be NarK1 and the C-terminal domain NarK2. From this it was determined which RAST gene function labels correspond to *narK1*, *narK2*, and *narK1K2*.

Additionally annotation files were searched for the cytochrome c nitrite reductase gene (*nrfA*) associated with dissimilatory nitrate reduction to ammonia (DNRA). Strains possessing this gene were excluded from further experimentation and analysis (Table S3).

Phylogenetic classification of strains

Phylogenetic analysis of denitrifying strains was performed using full 16S rRNA sequences identified in annotated draft genome assemblies. 16S sequences were uploaded for classification up to the genus level using the SILVA ACT service (http://www.arb-silva.de/) (Pruesse et al., 2012). A maximum-likelihood phylogenetic tree was computed using MEGA X 10.1.8 (Kumar et al., 2018).

Measuring relative abundances and contamination

The *N*-strain consumer-resource model provides predictions of the relative abundances of each strain in a community. These predictions were tested by measuring relative abundances for a set of 2-strain communities using the package CASEU 0.1.2 in R 3.6.1 (Cermak et al., 2020). Compositional Analysis by Sanger Electropherogram Unmixing (CASEU) infers relative abundances in communities via Sanger sequencing amplicons of a marker gene that distinguishes the different strains (e.g., the 16S rRNA gene). The approach works by deconvolving mixed Sanger electropherograms of amplicons from a community using the pure electropherograms obtained by sequencing amplicons from axenic cultures. Therefore the approach requires that (a) the constituents of a community can be cultured axenically, and (b) the electropherograms of a marker gene for each strain individually be sufficiently distinct (i.e., having pairwise electropherogram correlations less or equal to than approximately 0.8; Cermak et al., 2020).

All pair combinations and monocultures of six taxonomically and phenotypically representative strains, *Achromobacter* sp. ACM01 (Nar/Nir), *Ensifer* sp. ENS09 (Nar/Nir), *Paracoccus* sp. PAR01 (Nar), *Pantoea* sp. PNT03 (Nar), *Agrobacterium* sp. AGB01 (Nir), and *Pseudomonas* sp. PDM13 (Nir), were inoculated, grown, and periodically sampled in denitrifying conditions. All cultures were initiated with 2 mM NO_3^-, with the exception of monocultures of Nir strains AGB01 and PDM13 and the pair culture of these two strains, which were initiated with 2 mM NO_2^-. Cultures were harvested at 64 h, at which time optical densities were measured. In order to calibrate a conversion from relative biomass density (as measured by OD600) and relative abundance of 16S amplicons, equal volume (450 μL) synthetic mixtures of all pairs of monocultures were also prepared with known relative abundances of each strain.

DNA was extracted from monocultures, pair cultures, and synthetic pair mixtures using the DNeasy UltraClean Microbial Kit. A fragment of the 16S rRNA gene was amplified using the 27F (AGAGTTTGATCMTGGCTCAG) and 806R (GGACTACNVGGGTWTCTAAT) universal primers. The following reagents were used for each reaction: 22 μL nuclease-free H_2O, 1 μL 27F primer (10 μM), 1 μL 807R primer (10 μM), 1 μL DNA extract, 25 μL Platinum Hot Start PCR Master Mix (Invitrogen). The following thermocycler settings were used: initial denaturation, 2 min at 94°C; amplification (35 cycles), 30 sec at 94°C, 30 sec at 53°C, 60 sec at 72°C; final extension, 10 min at 72°C. PCR products were cleaned using the QIAquick PCR Purification Kit (Qiagen). Sanger sequencing of cleaned PCR products was performed at the University of Chicago Comprehensive Cancer Center DNA Sequencing and Genotyping Facility.

Resulting AB1 files containing electropherogram signals were analyzed using CASEU to infer relative abundances in each sample. First, it was verified that the six pure electropherograms from monocultures of the different strains were sufficiently distinct to distinguish signals in mixed electropherograms. Pairwise correlations between pure electropherograms were computed using CASEU, and were generally found to be much smaller than 0.8, with the exception of the Alphaproteobacteria ENS09, PAR01, and AGB01, pairs of which had electropherogram correlations of approximately 0.8. It was therefore concluded that these strains could be distinguished in a community using the CASEU approach.

Next, the six pure electropherograms were used to infer relative abundances in the pair cultures. In order to assess the extent of cross-contamination in these pair cultures, CASEU was allowed infer relative abundance using all six pure electropherograms for each pair culture, in essence assuming that any of the six strains could be present in any given pair culture. In every community, no evidence of cross-contamination was observed (i.e., in each pair community, only the intended pair of strains was measured at non-zero relative abundance. Though the CASEU approach cannot reliably resolve relative abundances below 1–2% (Cermak et al., 2020), if cross-contamination was present at these levels, it would have little to no impact on community metabolite dynamics. Therefore it was concluded that cross-contamination was generally negligible in denitrification experiments.

QUANTIFICATION AND STATISTICAL ANALYSIS

Consumer-resource model for metabolite dynamics

A consumer-resource model was used to parameterize the dynamics of nitrate and nitrite-reduction. For a single strain that performs both nitrate and nitrite reduction (Nar/Nir strain), the model is as follows:

$$\begin{aligned}\frac{dx}{dt} &= \left(\gamma_A r_A \frac{A}{K_A + A} + \gamma_I r_I \frac{I}{K_I + I}\right) x, \\ \frac{dA}{dt} &= -r_A \frac{A}{K_A + A} x, \\ \frac{dI}{dt} &= \left(r_A \frac{A}{K_A + A} - r_I \frac{I}{K_I + I}\right) x.\end{aligned} \qquad \text{(Equation 3)}$$

The variable x (in units of OD at 600 nm) is the biomass density of a single population, and A and I (mM) are the concentrations of nitrate and nitrite respectively. The model is parameterized by reduction rates r_A and r_I (mM/OD/h), yields γ_A and γ_I (OD/mM), and substrate affinities and K_A and K_I (mM), for growth on nitrate and nitrite, respectively.

The model, which resembles the Monod model for bacterial growth (Monod, 1949), assumes that growth of the population occurs at a rate proportional to the reduction rates of nitrate and nitrite, with the two resources treated as substitutable. Nitrite is the direct product of nitrate reduction (in a 1:1 stoichiometry). Nitric oxide, the product of nitrite reduction, is not explicitly modeled, and thus mass leaves the system when nitrite is reduced. For a strain that performs only nitrate reduction (Nar strain), the model simplifies by

setting $r_I, \gamma_I = 0$. Likewise for a strain that performs only nitrite reduction (Nir strain), $r_A, \gamma_A = 0$. This model assumes that nitrate and/or nitrite are the growth-limiting nutrients and therefore the concentration of electron donors (e.g., succinate) is not explicitly modeled.

Inferring phenotypic parameters from data

Monoculture experiments were performed for 78 soil isolates and one reference strain *Paracoccus denitrificans* ATCC 19367 under denitrifying conditions in succinate defined medium (SDM) in order to estimate parameters of the consumer-resource model (Equation 3). Monoculture experiments were also performed in acetate defined medium (ADM) for the 64 strains that grew aerobically on ADM (Table S1).

Fitting yield parameters

The yield parameters γ_A and/or γ_I were directly measured for each strain from endpoint measurements of optical density and nitrate/nitrite concentration.

To demonstrate how this is possible, Equation 3 gives:

$$\frac{dx}{dt} = -\gamma_A \frac{dA}{dt} - \gamma_I \left(\frac{dA}{dt} + \frac{dI}{dt} \right). \quad \text{(Equation 4)}$$

Therefore it follows from the fundamental theorem of calculus that:

$$\int_0^T \frac{dx}{dt} dt = x_T - x_0 = -\gamma_A \int_0^T \frac{dA}{dt} dt - \gamma_I \left(\int_0^T \frac{dA}{dt} dt + \int_0^T \frac{dI}{dt} dt \right) \quad \text{(Equation 5)}$$
$$= \gamma_A (A_0 - A_T) + \gamma_I (A_0 - A_T + I_0 - I_T),$$

where the subscripts 0 and T denote the values of the variables at $t = 0$ and T, respectively.

Equation 5 indicates that γ_A and γ_I can be inferred using measurements of biomass density and nitrate/nitrite concentrations at some time $t = T$, given knowledge of the experimentally-specified initial values of these variables. Because this equation is linear with up to two unknowns (recall that $\gamma_I = 0$ for Nar strains and $\gamma_A = 0$ for Nir strains), fitting this equation could in principle be accomplished using data from a single experimental condition for Nar and Nir strains or two experimental conditions for Nar/Nir strains. Instead γ_A and γ_I were fit to data from many conditions in order to obtain more robust estimates. Specifically, monocultures were grown in the following conditions: (a) 2 mM NO_*^-, $OD600_0$ = 0.01, (b) 1 mM NO_*^-, $OD600_0$ = 0.01, (c) 2 mM NO_*^-, $OD600_0$ = 0.001, where Nar/Nir strains were cultured with NO_3^- and NO_2^- separately (6 conditions total), Nar strains were cultured with NO_3^- (3 conditions total), and Nir strains were cultured with NO_2^- (3 conditions total). Then the equation

$$OD600_{64} - OD600_0 = \gamma_0 + \gamma_A (A_0 - A_{64}) + \gamma_I (A_0 - A_{64} + I_0 - I_{64}), \quad \text{(Equation 6)}$$

was fit via ordinary least squares regression using endpoint measurements from all conditions taken at $t = 64$ h. The intercept term γ_0 was included in Equation 6 to account for small systematic measurement errors, and was typically close to zero (Figure S1A). Examples of fits to Equation 6 are shown in Figures S1B–S1D.

Parameterizing Equation 3 in terms of OD assumed that biomass (g dry weight/L) is proportional to OD600, and that the constant of proportionality is the same for all strains in the library. Previous literature reports that the ratio g dry weight/L/OD is typically 0.4 (Coultate and Sundaram, 1975; Rosenberger and Elsden, 1960; Hassen et al., 1998; Péquignot et al., 1998; Nikel et al., 2021; Lee et al., 2007). In order to test whether some strains might secrete optically active compounds that absorb strongly at 600 nm, and thereby corrupt the biomass to OD conversion, four representative strains (*Achromobacter* sp. ACM01, *Ensifer* sp. ENS09, *Paracoccus denitrificans* ATCC 19367, and *Pseudomonas* sp. PDM21) were cultured in SDM under denitrifying conditions for 64 h. Cells were then removed from the endpoint cultures by filtration and OD600 of the filtered medium was measured. It was observed that absorbance levels were at or below that of fresh medium. It was therefore concluded that secretion of optically active molecules likely does not impact the inference of biomass from OD, and that using OD600 as a proxy for biomass incurs only a modest error. However, it is important to recognize that directly measuring the biomass of each strain in the library may improve the quality of model fits to data and alter regression results.

Fitting rate parameters

For each strain, having determined the yield parameters, the rate parameters r_A and r_I were then globally (simultaneously) fit to nitrate/nitrite dynamics data across all experimental conditions by minimizing the sum of squared residuals between the data and numerical solutions to Equation 3 (see example in Figure S1E). Equation 3 was solved numerically using the differential equation solver ode23s in MATLAB R2017b. The solver was initialized at $t = t_1$ (where t_1 is the time point of first nitrate/nitrite measurement, approximately 2 h), setting initial conditions $N(t_1) = OD600_0$, and $A(t_1)$ and $I(t_1)$ to the median measured values of nitrate and nitrite concentration at $t = t_1$ over experimental replicates within a given condition. The constrained optimization function fmincon was used in conjunction with the global minimum search function GlobalSearch to minimize the sum of squared residuals and obtain optimal values of r_A and r_I. Values of r_A and r_I were constrained between 0 and 50 mM/OD/h.

Initially, this approach was used to simultaneously fit both rates (r_A and r_I) and substrate affinities (K_A and K_I), but it was observed in nonparametric bootstrap estimates of parameter error that the affinities K_A and K_I were not well constrained by experimental

measurements (Figure S1F, median fractional errors of 30.0% and 26.5% for K_A and K_I in SDM, respectively). This is likely because the true values are small relative to the typical scale of substrate concentrations in the experiments: values for nitrate/nitrite affinity constants between 0.003–0.055 mM have been identified for denitrifying cultures previously (Beccari et al., 1983; Claus and Kutzner, 1985; Kornaros et al., 1996; Dinçer and Kargı, 2000), while cultures were initialized with 1–2 mM nitrate/nitrite. In the dynamical regimes of Equation 3 where substrate concentrations are much greater than affinity constants (i.e., $A \gg K_A, I \gg K_I$), the dependence of Equation 3 on K_A and K_I vanishes. This restricts identifiability of the affinity parameters to the regime where A, I are on the same scale as K_A, K_I (likely in the micromolar range). This regime typically occurs only briefly during the experiments, just before the substrates are exhausted, and sampling this regime for all strains would require a much greater sampling frequency than what was attempted in this study. Alternatively, the affinity parameters could be measured by comparing differences in growth/reduction rates at very low substrate concentrations, so that growth occurs in a regime where these rates depend more strongly on the affinity parameters (i.e., $A_0 \ll K_A$, $I_0 \ll K_I$). Doing this would require much more sensitive measurement of biomass density or nitrate/nitrite concentration than what was attempted in this study. Regardless, it was observed in nonparametric bootstrap estimates of parameter error that fitted values of r_A and r_I were insensitive to K_A and K_I (Figure S1G, median fractional errors of 3.8% and 4.2% for r_A and r_I in SDM, respectively), as was the qualitative model behavior (Figure S1H) and the fit quality (Figure S1I). Therefore K_A and K_I were fixed to 0.01 mM.

Treatment of poorly-fitting strains

By fitting metabolite dynamics across multiple initial media and biomass density conditions to the model Equation 3, it was assumed that this simple model is a good representation of the metabolic phenotypes of denitrifying strains, with a few parameters capturing the full extent of the metabolite dynamics. In the majority of cases it was observed that the model fit the metabolite dynamics well (see example in Figure S1E), indicating that the assumptions of model Equation 3 were appropriate. However in some cases (e.g., Figures S1J and S1K) the observed metabolite dynamics departed significantly from the optimal model fits. Often it appeared that different parameterizations were necessary for different initial conditions, e.g., nitrite reduction rates appeared to differ depending on whether nitrite was initially supplied (for example Figure S1J). In these cases, while the model apparently failed to capture the metabolite dynamics phenotypes across all conditions simultaneously, it appeared that it was still possible to estimate consumer-resource parameters for a subset of initial conditions.

Therefore a pipeline was developed for parameterizing the model Equation 3 on a subset of experimental conditions if poor fits were obtained when fitting to all conditions. First yields on nitrate and nitrite were fit using all experimental conditions. Then the pipeline proceeded as follows for each strain:

1. Fit reduction rates to all experimental conditions. If the root-mean-square error (RMSE) evaluated between observed data and model solutions across all experimental conditions and replicates exceeds a threshold T, then proceed to step 2. If not, accept the parameter fit.
2. Fit reduction rates only to experimental conditions where $OD600_0 = 0.01$. If the RMSE evaluated across these high biomass-density conditions exceeds T, proceed to step 3. If not, accept the parameter fit.
3. (Nar/Nir strains only) Fit reduction rates only to experimental conditions where nitrate was initially supplied. If the RMSE evaluated across these conditions exceeds T, then proceed to step 4. If not, accept the parameter fit.
4. (Nar/Nir strains only) Fit reduction rates only to experimental conditions where $OD600_0 = 0.01$ and nitrate was initially supplied. If the RMSE evaluted across these conditions is less than or equal to T, accept the parameter fit.

This pipeline was used with $T = 0.17$ to obtain fits for monocultures of all 79 strains in SDM and 64 strains in ADM. The RMSEs for strains at each step in the fitting pipeline are shown in Table S5. An example of a fit obtained using the first three steps of the pipeline is shown in Figure S1J, and a fit obtained using the first two steps is shown in Figure S1K. Only the first three steps of the pipeline were necessary to produce parameter fits with error less than $T = 0.17$ for the monocultures in SDM, while step 4 was necessary for only 4 out of 64 ADM monocultures (Table S5).

Finally, there were 7 Nar strains (PDM26–PDM32) for which nitrate concentrations appeared to asymptotically approach nonzero values in SDM (see example in Figure S1L). However, since it was possible to fit consumer-resource parameters to these cases with relatively low error (Table S5), these parameter fits were accepted for use in subsequent analyses.

Validating predictions for biomass density dynamics

Although the rate parameters r_A and r_I for each strain were fit by directly measuring the dynamics of nitrate and nitrite reduction, only endpoint measurements were used to fit the yield parameters γ_A and γ_I, and biomass density dynamics were not directly measured. Though the yield parameters are identifiable via endpoint measurements (Equation 5), the accuracy of predictions for biomass density dynamics depends on the consumer-resource model (Equation 3) being reasonably well-specified. For instance, if mortality is an important factor that causes biomass density to change significantly on the timescale of the experiment, then the measurement of yields would lead to poor biomass predictions because cell death is not accounted for in the model.

To validate the inference of yields and model predictions for biomass density dynamics, these dynamics were directly measured for a set of four taxonomically-representative Nar/Nir strains: *Achromobacter* sp. ACM01, *Ensifer* sp. ENS09, *Paracoccus denitrificans* ATCC 19367, and *Pseudomonas* sp. PDM21. These four strains were cultured in SDM under denitrifying conditions with 2 mM NO_3^-, $OD600_0 = 0.01$, and 21 experimental replicates. Cultures were manually sampled (300 μL) from 3 replicates at 7

time points (2, 4, 6, 8, 16, 32, and 64 h from the start of anaerobic culture), with different replicates sampled at each time point. Optical density was measured immediately after sampling, and measurements were post-processed to correct for evaporation.

The measured values of biomass density are shown in Figure S1M, alongside predictions of the model Equation 3 using previous inferences of rate and yield parameters for these strains in SDM. Predicted biomass dynamics agree well with the measured optical densities, both in the exponential and stationary phases. The errors of predicted biomass density relative to measurements at $t =$ 64 h are all less than 10%, indicating that the yields were well-estimated by the fitting protocol. No appreciable evidence for mortality was observed, with little to no decline in biomass density observed after nitrate and nitrite were exhausted. This is consistent with previous measurements of low-density starving cultures of *Escherischia coli* K12, where negligible cell death was observed after approximately 50 h (Phaiboun et al., 2015). It was concluded that the fitting procedure for rates and yields faithfully captures biomass density dynamics, despite the fact that biomass density is only measured at $t =$ 64 h.

Estimating parameter error

A nonparametric bootstrap was used to estimate the sampling distributions of $\{r_A, \gamma_A, r_I, \gamma_I\}$ for the 79-strain library in SDM. Bootstrap datasets were generated by resampling (with replacement) among replicates; that is, for an experimental condition (e.g., A_0 = 2 mM, I_0 = 0 mM, $OD600_0$ = 0.01) performed with four replicates, a new dataset was created by randomly selecting a set of four replicates with replacement, doing this for all conditions. Then $\{r_A, r_I, \gamma_A, \gamma_I\}$ were refit to these bootstrap resamples. This was repeated 100 times for each strain to obtain sampling distributions for these parameters. Fractional errors, defined as the ratio of the interquartile range to the value of the parameter, are less than 10% for the vast majority of inferred parameters. Since γ_A and γ_I inferences are error-prone when measured biomass densities (and therefore yields) are low, a yield parameter was set identically to zero if its estimate was negative or within one standard error of zero.

Regressing SDM phenotypes onto denitrification gene content

Formulating the regression problem

Linear regression was used to predict the measured consumer-resource parameters $\{r_A, \gamma_A, r_I, \gamma_I\}$ from the presence and absence of denitrification-related genes in the genomes of each strain. The regression problem was formulated as follows:

$$y_i = \beta_0 + \sum_{j=1}^{P} \beta_j g_{ij} + \varepsilon_i \quad \text{for } i = 1, \ldots, N. \qquad \text{(Equation 7)}$$

The response variable y_i is the observed value of a consumer-resource model parameter (e.g., r_A) for strain i, with N such observations in total. The predictors g_{ij} are indicator variables that take the value 1 if strain I has gene j and take 0 otherwise, with $P =$ 17 predictors in total. The coefficients β_j and intercept β_0 are fit by the regression, which determines the residual term ε_i. This formulation assumes that genes contribute additively (and not quadratically, etc.) to the value of a phenotypic parameter. While in principle there may exist a formulation of this regression with greater predictive power that takes into account the nonlinear interactions between predictors (e.g., a model with quadratic terms), a linear formulation was chosen to keep the number of fitting parameters small relative to the number of observations.

The LASSO regression method (Hastie et al., 2008; Hastie et al., 2016) was used to solve Equation 7. For given gene presence/absence vectors $\vec{g}_i$ and response vector y, LASSO regression solves:

$$\min_{\beta_0, \vec{\beta}} \left\{ \frac{1}{2N} \sum_{i=1}^{N} \left(y_i - \beta_0 - \vec{g}_i^{\,T} \vec{\beta} \right)^2 + \lambda || \vec{\beta} ||_1 \right\}, \qquad \text{(Equation 8)}$$

performing both variable selection and regularization by penalizing the sum of squared residuals by the L_1 norm of the coefficient vector $\vec{\beta}$. The strength of the penalty is controlled by the hyperparameter λ, which at moderate values sets the coefficients of poor predictors identically to zero, thus resulting in a sparse model. Typically the hyperparameter value $\lambda = \hat{\lambda}$ is selected by minimizing prediction error in cross-validation, which optimizes the ability of the model to generalize out of sample, and makes the method suitable for datasets where overfitting via an approach such as ordinary least squares (OLS) is likely because the number of predictors and the number of observations are on the same order of magnitude.

LASSO regressions were performed in MATLAB R2017b for each consumer-resource parameter measured in SDM separately, obtaining different $\vec{\beta}$ and β_0 for each regression. The fits and coefficients for regressions on consumer-resource parameters measured in SDM are shown in Figures 4C–4J. Note that for nitrate-related parameters (r_A and γ_A), only strains capable of nitrate reduction (Nar and Nar/Nir phenotypes) were included in the predictor-response datasets. Similarly for the nitrite-related parameters, only strains with Nar/Nir and Nir phenotypes were included in the predictor-response datasets. Prior to fitting, all predictors were standardized to have zero mean and unit variance.

Hyperparameter selection via cross-validation

For each regression of the form given in Equation 7, iterated K-fold cross-validation was used to determine the value $\lambda = \hat{\lambda}$ that minimizes estimated prediction error. Optimal hyperparameter values were determined for each regression individually, rather determining than one hyperparameter value to be used for all regressions. This was done because the hyperparameter controls the level of sparsity in the resulting solution (i.e., the number of genes that are nonzero in the optimal set of regression coefficients), and *a priori*

the optimal level of sparsity may differ among the different regressions on consumer-resource parameters. Choosing an optimal value of λ for each regression individually ensured that the best LASSO solution for each regression was identified.

Let Λ be a set of discrete values of λ for which Equation 8 is solved. Each iteration of cross-validation proceeds in the following way:

1. Randomly partition the data into K subsamples of roughly equal size.
2. For each $k = 1,2,\ldots,K$:
   (a) Holding out the kth fold (test set), solve Equation 8 at each $\lambda \in \Lambda$ using the union of the remaining remaining $K-1$ folds of data (training set).
   (b) Use the resulting regression coefficients to predict the responses in the test set.
   (c) Evaluate root-mean-square error of the test set prediction.

This process is iterated M times, each time choosing a new random partition of the data into K subsamples. The average over the KM estimates of prediction error was recorded at each value of $\lambda \in \Lambda$, and the optimal value $\lambda = \widehat{\lambda}$ was then selected as that which minimized this estimate of error. An iterated K-fold cross-validation approach was chosen over either basic K-fold $(M = 1)$ or leave-one-out $(K = N)$ cross-validation because iterated cross-validation averages over the sampling variability inherent in randomly partitioning the dataset into groups, and also because partitioning into $K \neq N$ folds allows the estimation the out-of-sample performance of the model through statistics such as the coefficient of determination between observed and predicted values on each test set.

A value of $K = 4$ for iterated cross-validation ($M = 10^4$ iterations) was chosen to balance the relative sizes of training and test sets for the purpose of evaluating out-of-sample performance; as K increases, the size of the cross-validation training set increases, while the size of test set decreases. It was observed that $\widehat{\lambda}$ was insensitive to the choice of K.

Estimating out-of-sample performance

The out-of-sample performance of regressions on each consumer-resource parameter was estimated during iterated K-fold cross-validation by computing the coefficient of determination (R^2) between observed and predicted response values in each test set. The median values of R^2 obtained via iterated 4-fold cross-validation ($M = 10^4$ iterations) at $\lambda = \widehat{\lambda}$, denoted $\overline{R}^2_{CV}$, is positive for all regressions.

The significance of $\overline{R}^2_{CV}$ for regressions on each consumer-resource parameter was evaluated under the null hypothesis that there is no relationship between the predictor and the response via a permutation test. The response variable for each regression was repeatedly permuted (1×10^3 permutations) and regression coefficients were re-fitted, using iterated 4-fold cross-validation ($M = 10^2$ iterations) to select the hyperparameter for each permutation. Under the null distributions of $\overline{R}^2_{CV}$ computed using this approach for regressions on SDM consumer-resource parameters, $p<0.001$ in all cases.

Post-selection inference

When the data used for model training via LASSO are also used for inference of significant regression coefficients, it is necessary to account for the fact that LASSO performs variable selection (i.e., selects some coefficients to be nonzero over others) (Hastie et al., 2016; Taylor and Tibshirani, 2015). Because LASSO preferentially selects variables with high predictive power in the training set, neglecting this selection results in overoptimistic confidence intervals and p-values.

To illustrate how and why this was done, first consider the simpler case of inference on regression coefficients determined by OLS. If the residuals ε_i are normally distributed, it can be shown that the sampling distribution of a coefficient β_j is also normal, with a sampling variance that can be estimated from the data. This sampling distribution can then be used to test the hypothesis that the true value of β_j is zero. In contrast, in the case where LASSO regression is used and the coefficient β_j is selected to be nonzero, it can be shown that a normal distribution is not appropriate for the sampling distribution of β_j (Taylor and Tibshirani, 2015). Instead the appropriate distribution is a truncated normal distribution, i.e., a normal distribution only defined along a finite interval. Intuitively, the distribution is truncated because the likely range of β_j must be conditioned upon the knowledge that LASSO selected it (along with a set of other elements of $\vec{\beta}$) to be nonzero. The bounds of the truncated distribution are determined by both the data and by the set of other nonzero elements of $\vec{\beta}$ via analytical relations, and can be computed using the package selectiveInference 1.2.5 in R 3.6.1 to estimate the sampling distributions for each nonzero element of $\vec{\beta}$. An intuitive description of this post-selection inference approach applied to the simpler context of forward stepwise regression can be found in Taylor and Tibshirani (2015), and a technical description of the approach applied to LASSO can be found in Hastie et al. (2016).

The function fixedLassoInf in the selectiveInference package was used to compute 90% confidence intervals and to obtain p-values under the null hypothesis the true value is zero for each nonzero coefficient for regressions on SDM consumer-resource parameters, evaluated at the hyperparameter value $\lambda = \widehat{\lambda}$ selected by cross-validation.

Characterizing phylogenetic correlation

Microbial phenotypic traits exhibit varying degrees of phylogenetic correlation as a result of shared evolutionary history (Martiny et al., 2015). To characterize the extent of phylogenetic correlation in the consumer-resource parameters $\{r_A, \gamma_A, r_I, \gamma_I\}$, the function phyloCorrelogram in the package phylosignal 1.3 for R 3.6.1 (Keck et al., 2016) was used. This function estimates autocorrelation in trait values by computing Moran's I index as a function of phylogenetic distance, measured here using the 16S rRNA phylogenetic tree. Statistically significant correlation (95% confidence intervals estimated using 1×10^3 bootstrap replicates) was observed over varying

levels of phylogenetic distance for the different parameters. The rate r_A was correlated to a small degree ($\max(I) = 0.16$) over a relatively short interval of phylogenetic distance (16S tree distance 0.01), while γ_A, r_I, and γ_I were correlated to a modest degree ($\max(I) =$ 0.33, 0.27 and 0.48, respectively) over longer intervals (0.16, 0.06 and 0.12, respectively).

Because the strain library contains a few clades of very closely related strains (e.g., ENS01–08, PDM20–23, Figure 3C), it is possible that some of the phylogenetic correlation measured in the full 79-strain library is attributable to the over-representation of these close relatives. In addition, the over-representation of these close relatives could in principle skew the results of the regressions. To estimate the influence of over-represented close relatives in the strain library on phylogenetic correlations and regression results, clades comprising strains with identical 16S rRNA sequences were pruned by randomly selecting one representative and removing the remaining strains from the dataset. This removed 15 strains from the library, resulting in a subsampled dataset of 64 strains. Phylogenetic correlograms were then computed for the SDM consumer-resource parameters on this pruned dataset. Pruning the dataset reduced correlations for γ_A, r_I, and γ_I, with maximum correlations decreasing for all three parameters ($\max(I) =$ 0.30, 0.21 and 0.39, respectively), and significant correlation lengths decreasing for γ_A and γ_I (0.05 and 0.09, respectively). The correlogram for the rate r_A in the pruned dataset, which showed a small degree of correlation in the full dataset, changed little. It was concluded that some of the phylogenetic correlation estimated for the full dataset was attributable to the over-representation of close relatives, but it is still the case that there exists statistically significant phylogenetic correlations at short distances. Next LASSO regressions were performed on the pruned dataset. Both in-sample and out-of-sample metrics of model performance (R^2_{fit} and $\overline{R}^2_{CV}$, respectively) changed little relative to the corresponding values for regressions on the full dataset. Similarly, the regression coefficients did not change substantially. From this it was concluded that the over-representation of close relatives did not have a large impact on the results of regressions on the consumer-resource parameters.

Evaluating randomly-selected genes as predictors

In order to assess whether denitrification genes make better predictor variables than other possible sets of genes, the SDM consumer-resource parameters $\{r_A, \gamma_A, r_I, \gamma_I\}$ were regressed onto the presence and absence of randomly-selected genes from the set of all annotated genes in strains in the library.

First the set of all uniquely-labelled protein-encoding genes present in the RAST annotations were identified for the 79-strain library. From this set of 13415 unique genes, 51 genes associated with denitrification were removed; this included not only terminal reductases, sensors/regulators, and transporters that were used as variables in the regression (Table S6), but also related chaperones, structural genes, and biosynthesis genes that frequently occur in clusters with the denitrification genes (Table S7).

New sets of predictor variables were then generated by randomly selecting genes from the set of 13364 non-denitrification genes and constructing binary presence/absence matrices as for denitrification-related genes. In order to create a fair comparison between these randomly-selected predictors and the denitrification gene predictors, (a) sets of only 17 genes were selected, matching the dimensionality of the denitrification gene presence/absence matrix, and (b) rejection sampling was performed to match the gene presence frequency (fraction of strains that possess a given gene) distribution of the denitrification genes. The latter was a necessary consideration because the distribution of presence frequencies of non-denitrification genes is heavily skewed toward zero relative to the frequencies of denitrification genes (Figure S2A), indicating that a large portion of genes occur only in a small number of strains.

To perform rejection sampling, densities for the gene frequency distributions were estimated, and these densities were used to define acceptance probabilities for random samples. Let $f(x)$ denote the probability density of gene frequencies for non-denitrification genes and similarly $g(x)$ for denitrification genes, where x here denotes gene presence frequency, and set the constant H so that $g(x)/f(x)/H \leq 1$ for all $x \in [0,1]$. Rejection sampling was then performed in the following way:

1. With uniform probability, randomly sample a candidate gene from the set of non-denitrification genes. Denote the frequency of this gene as x_0.
2. Accept the candidate gene as a predictor with probability $g(x_0)/f(x_0)/H$. Otherwise reject the candidate and return to step 1.
3. Return to step 1 until 17 genes are accepted.

This process results in a set of 17 predictors that have a gene presence frequency distribution approximately equal to $g(x)$. The ksdensity function in MATLAB R2017b was used to estimate $f(x)$ and $g(x)$ using a bandwidth parameter value of 0.4 (Figure S2A). This rejection sampling approach was used to generate 1×10^3 different sets of 17 predictors for regressing against each of the SDM consumer-resource parameters $\{r_A, \gamma_A, r_I, \gamma_I\}$.

LASSO regressions were performed on each of the SDM consumer-resource parameters $\{r_A, \gamma_A, r_I, \gamma_I\}$ using the rejection-sampled sets of gene predictors, where the optimal hyperparameter value $\lambda = \widehat{\lambda}$ was selected via iterated 4-fold cross-validation ($M = 10^3$ iterations). Out-of-sample performance of each regression was also evaluated in cross-validation by computing $\overline{R}^2_{CV}$, the median coefficient of determination value computed across cross-validation test sets. The distributions of these $\overline{R}^2_{CV}$ values across different sets of random genes are shown in (Figure S2B), alongside the values of $\overline{R}^2_{CV}$ obtained via the regressions onto denitrification-related genes. The denitrification genes performed better than the typical set of random genes in regressions on two out of four consumer-resource parameters (r_A and γ_A), and as well as random genes for one parameter (γ_I). On the whole, this analysis suggested that denitrification genes were better predictors than arbitrary genes, but it remains unclear why arbitrary genes tend have modest predictive power ($\overline{R}^2_{CV} > 0$), and why the denitrification genes performed worse than the typical set of random genes for

the r_I parameter. One possible explanation is that some random genes served as good predictors only because they resemble the denitrification genes in terms of presence and absence.

To investigate whether the predictive power of random genes arises because of correlations (in terms of presence and absence) with the denitrification genes, new sets of random gene predictors were constructed via rejection sampling as described above, but this time sampling only from the set of genes that have low or non-significant correlation with denitrification genes. Specifically, for each of the non-denitrification gene presence/absence vectors, the Pearson correlation ρ was computed with each of the denitrification gene presence/absence vectors. This identified the set of non-denitrification genes that have large correlations ($|\rho| \geq 0.5$) with any of the denitrification genes that are significant at the 1% level, where significance was evaluated by generating a zero-correlation null distribution via a permutation test. The latter consideration is important for evaluating correlations between very high or very low-frequency genes, for which the probability of spurious large correlations can be high. These denitrification gene-correlates were excluded from sampling when generating the new sets of random gene predictors. As before, 1×10^3 different sets of 17 predictors for regressing against each of the consumer-resource parameters were generated.

LASSO regressions on each of the SDM consumer-resource parameters $\{r_A, \gamma_A, r_I, \gamma_I\}$ were again performed using the rejection-sampled genes that exclude denitrification gene correlates. The distributions of the resulting $\overline{R}^2_{CV}$ values are shown in Figure S2C. The following changes in these distributions relative to Figure S2B were observed: (a) the median predictive power for all random gene regressions decreased substantially (i.e., $\overline{R}^2_{CV}$ decreased), indicating that indeed a substantial part of the predictive power of random genes arises due to large correlations with denitrification genes, and (b) denitrification genes now outperformed the typical set of random genes as predictors for even the r_I regression, demonstrating the superiority of denitrification genes as predictors for regressions on all consumer-resource parameters.

While the superior predictive power of the 17 denitrification genes was demonstrated in direct comparisons with sets of 17 randomly-selected genes, there may exist genes outside of the denitrification pathway with complementary predictive power when added to the denitrification genes. Therefore it was investigated whether adding additional randomly-selected genes to the denitrification genes further improves the predictive power of regressions on the consumer-resource parameters. To address this question, sets of predictor variables were generated by randomly sampling (without replacement) $P-17$ genes from the set of 13364 non-denitrification-related genes and constructing binary presence/absence matrices using the denitrification genes as the first 17 predictors and the randomly-selected genes as the subsequent $P-17$ predictors. P was varied between 32 and 2048 to investigate the dependence of prediction quality on the number of additional genes added. 10 sets of predictor variables were randomly generated for each value of P. Then LASSO regressions on each of the SDM consumer-resource parameters $\{r_A, \gamma_A, r_I, \gamma_I\}$ were performed using these predictors. The distributions of $\overline{R}^2_{CV}$ as a function of P are shown in Figure S2D. Adding additional predictors beyond the 17 denitrification genes did not substantially improve the predictive power of the models, regardless of how many additional predictors were added. This indicates that the 17 denitrification genes harbor the majority of gene presence/absence predictive power.

Evaluating alternative genomic predictors

It was investigated whether either 16S rRNA copy number, genome size, or GC-content could serve as better predictor variables for the consumer-resource parameters $\{r_A, \gamma_A, r_I, \gamma_I\}$ than denitrification genes. Previous work demonstrates a positive relationship between 16S copy number and maximum potential growth rate across diverse taxa in nutrient-replete conditions (Roller et al., 2016; Li et al., 2019), likely because increased ribosome production allows a higher rate of protein synthesis, thereby increasing growth rate (Scott et al., 2010). A negative relationship between growth rate and genome size has also been observed (Li et al., 2019), possibly due to a reduced nutrient burden required by smaller genomes (Hessen et al., 2010). GC-content has been investigated as a genomic predictor for various bacterial phenotypes such as optimal growth temperature (Galtier and Lobry, 1997), and can serve as a baseline for spurious phylogenetic correlations because it is a slowly-evolving genomic property (Haywood- Farmer and Otto, 2003).

16S copy number was estimated for all 79 strains in the library using the 16Stimator pipeline (Perisin et al., 2016). This approach uses Illumina sequencing reads and annotated draft assemblies to compute the coverage ratio of the 16S gene relative to a curated set of single-copy genes. The genome size was estimated for all strains in the library by summing the lengths of all assembled contigs for each strain. Genomic GC-content was computed from draft assemblies using QUAST 5.02 (Gurevich et al., 2013). For the reference strain *Paracoccus denitrificans* ATCC 19367, a complete genome assembly (Si et al., 2019) showed 3 copies of the 16S gene, a genome size of 5.24 mb, and a GC-content of 66.80%, and 3.36 16S copies; a genome size of 5.15 mb, and a GC-content of 66.81% were estimated using the draft assembly.

First the relationships between 16S copy number, genome size, GC-content, and the SDM consumer-resource parameters $\{r_A, \gamma_A, r_I, \gamma_I\}$ were considered. No significant (permutation test) correlations were observed between 16S copy number and the consumer-resource parameters, significant positive correlations were observed between genome size and γ_A ($\rho = 0.40$, $p< 1\times10^{-4}$) and γ_I ($\rho = 0.63$, $p<1\times10^{-4}$), and significant but weak positive correlations were observed between GC-content and γ_A ($\rho = 0.24$, $p = 0.02$) and r_I ($\rho = 0.23$, $p = 0.04$). These data suggest that genome size may be a good predictor for the yields γ_A and γ_I.

In order to compare consumer-resource parameter measurements to previous findings relating growth rate to 16S copy number and genome size, growth rates on nitrate and nitrite were computed for each strain. Equation 3 can be recast in terms of growth rates μ_* (1/h) by setting $r_* = \mu_*/\gamma_*$:

$$\frac{dx}{dt} = \left(\mu_A \frac{A}{K_A + A} + \mu_I \frac{I}{K_I + I}\right)x,$$
$$\frac{dA}{dt} = -\frac{\mu_A}{\gamma_A}\frac{A}{K_A + A}x, \qquad \text{(Equation 9)}$$
$$\frac{dI}{dt} = \left(\frac{\mu_A}{\gamma_A}\frac{A}{K_A + A} - \frac{\mu_I}{\gamma_I}\frac{I}{K_I + I}\right)x.$$

In this form the μ_* represent the exponential growth rates when substrates are not limiting (e.g., when $A \gg K_A$ or $I \gg K_I$). Therefore $\mu_* = r_*\gamma_*$ were computed using the SDM consumer-resource parameters.

No significant positive correlations were observed between either of the growth rates with 16S copy number. This differs from what has been previously observed under aerobic, nutrient-replete conditions (Roller et al., 2016; Li et al., 2019), where ribosomal production is likely to be growth limiting. This may be because these previous studies were based on maximum potential growth rates (measured across a variety of medium and culturing conditions), whereas maximum potential growth rates were not systematically identified for strains in the library. Moreover it is likely that most of the measured growth rates in denitrifying conditions with a succinate defined medium are much smaller than maximum potential growth rates, because denitrification is generally a significantly lower ATP-yielding process than aerobic respiration (Strohm et al., 2007), and also because succinate defined medium likely imposes more stringent biosynthesis demands than a complex, rich medium (Scott et al., 2010). Therefore the relative benefit of high gene copy number of rRNA for many strains under denitrifying growth conditions may be small. However significant (permutation test) positive correlations were observed between genome size and μ_A ($\rho = 0.21, p = 0.04$), and μ_I ($\rho = 0.63\,0.52, p < 1\times10^{-4}$). This finding also differs the previous observation of a negative relationship between genome size and growth rate (Li et al., 2019).

Finally, the potential of 16S copy number, genome size, and GC-content as predictor variables was evaluated in a head-to-head comparison with denitrification genes by using all these predictors simultaneously in LASSO regressions on the SDM consumer-resource parameters $\{r_A, \gamma_A, r_I, \gamma_I\}$ (4-fold cross-validation, iterated 1×10^4 times). As before, all predictors were standardized to have zero mean and unit variance before fitting. The following was observed: (a) 16S copy number, genome size, and GC-content were not assigned large coefficients in any regression, (b) the statistics of fitting and generalization quality (R^2_{fit} and $\overline{R}^2_{CV}$) were essentially the same as those obtained in the original regressions, and (c) the coefficients for denitrification genes were very similar to those obtained in the original regressions. It was concluded that the denitrification genes hold greater predictive power than 16S copy number, genome size, and GC-content, since the latter predictors are not selected as important variables by LASSO regression.

Regressing ADM phenotypes onto denitrification gene content

Regressions for the consumer-resource parameters measured in ADM were performed as for those parameters measured in SDM. The median values of R^2 obtained via iterated 4-fold cross-validation ($M = 10^4$ iterations) ($\overline{R}^2_{CV}$) were positive for all regressions. The p-values of $\overline{R}^2_{CV}$ (permutation test) were all <0.01.

Predicting community metabolic dynamics

The consumer-resource model (Equation 3) was extended to generate predictions for community (i.e., multi-strain) metabolite dynamics. For an N-strain community, the extended model is as follows:

$$\frac{dx_i}{dt} = \left(\gamma_A r^i_A \frac{A}{K_A + A} + \gamma^i_I r^i_I \frac{I}{K_I + I}\right)x_i, \quad \text{for } i = 1, \ldots, N$$
$$\frac{dA}{dt} = -\sum_{i=1}^{N} r^i_A \frac{A}{K_A + A}x_i,$$
$$\frac{dI}{dt} = \sum_{i=1}^{N}\left(r^i_A \frac{A}{K_A + A} - r^i_I \frac{I}{K_I + I}\right)x_i. \qquad \text{(Equation 10)}$$

For each strain i, which has biomass density x_i, the parameters $\{r^i_A, \gamma^i_A, r^i_I, \gamma^i_I\}$ were measured in monoculture. Note that, as before, $K_A = K_I = 0.01$ mM for all strains. This "additive" model sums the independent rate contributions of each strain to the nitrate and nitrite differential equations, in effect assuming that strains only interact via cross-feeding and competition for extracellular nitrate and nitrite. The model *does not* assume that strains interact through Lotka-Volterra-type (quadratic) terms in the biomass density equations, nor does it assume that the parameters $\{r^i_A, \gamma^i_A, r^i_I, \gamma^i_I\}$, measured in monoculture, are modulated by the presence of any other strain. Thus Equation 10 represents a null model for community metabolite dynamics where each strain in a community behaves as it does in monoculture, and as a result provides a prediction requiring no additional free parameters.

Simple communities were assembled and cultured to test the predictions of Equation 10, drawing from a representative 12-strain subset of the 79-strain library: Nar/Nir strains *Achromobacter* sp. ACM01, *Ensifer* sp. ENS09, *Paracoccus denitrificans*, *Pseudomonas* sp. PDM21; Nar strains *Acidovorax* sp. ACV02, *Paracoccus* sp. PAR01, *Pseudomonas* sp. PDM12, *Pantoea* sp. PNT03; Nir strains *Agrobacterium* sp. AGB01, *Pseudomonas* sp. PDM13, *Pseudomonas* sp. PDM14, and *Pseudoxanthomonas* sp. PXM03. Nitrate/nitrite dynamics and endpoint optical density were measured for (a) all 66 2-strain combinations, (b) a random set of 81 three-strain combinations, (c) 21 four-strain combinations, (d) 6 five-strain combinations, and (e) controls of each strain in monoculture. 6 of the four-strain combinations were chosen randomly from the set of 12 strains, while the remaining 15 four-strain combinations and all five-strain combinations were exhaustive combinations of the six strains ACM01, ENS09, PAR01, PNT03, AGB01, and PDM13. All communities/controls were cultured in SDM in each of two media conditions, 2 mM nitrate and 2 mM nitrite, with 2–3 experimental replicates per condition. Initial biomass densities were $OD600_0 = 0.01$ for each strain in a given community.

First endpoint biomass densities were compared with the values predicted by the additive model, Equation 10. Since the optical density measurement cannot discern between strains in a mixed population, a model prediction for total endpoint biomass density was computed by summing the endpoint biomass densities of each strain. Endpoint biomass densities were well-predicted by Equation 10 (Figure S4A). This gives one indication that the additive consumer-resource model in Equation 10 accurately predicts community behavior using only information from monocultures.

The ability of the additive model to predict relative abundances for a subset of pair cultures was evaluated. All pair combinations and monocultures of six taxonomically and phenotypically representative strains (Nar/Nir strains *Achromobacter* sp. ACM01 and *Ensifer* sp. ENS09; Nar strains *Paracoccus* sp. PAR01 and *Pantoea* sp. PNT03; Nir strains *Agrobacterium* sp. AGB01 and *Pseudomonas* sp. PDM13) were cultured and periodically sampled. All cultures were initiated with 2 mM NO_3^-, with the exception of monocultures of Nir strains AGB01 and PDM13 and the pair culture of these two strains, which were initiated with 2 mM NO_2^-. Then the relative abundance of 16S rRNA amplicons in the pair cultures was measured using CASEU (Cermak et al., 2020). In order to enable a comparison with the predictions of the model, Equation 10, which makes predictions in terms of biomass density (in units of OD), conversion constants were measured to transform 16S amplicon relative abundances to OD600 relative abundances. Doing so is necessary because (a) strains generally differ in 16S rRNA gene copy number per cell (ranging from 4–7 copies per cell for these strains), and (b) strains will have generally different conversion factors from OD600 to cells/mL, arising for instance due to differences in cell size. Therefore, the ratios of 16S amplicon abundances will be related to the ratio of biomass densities by the equation:

$$\frac{a_i}{a_j} = \frac{b_i c_i x_i}{b_j c_j x_j} = K_{ij}\frac{x_i}{x_j}, \qquad \text{(Equation 11)}$$

where for strain i, a_i is the 16S amplicon relative abundance, x_i the biomass density relative abundance, and b_i and c_i are respectively the 16S rRNA gene copy number (16S rRNA copies/cell) and cell density to OD600 conversion factor (cells/mL/OD). This means that the ratio of 16S amplicon abundances for strains i and j will be related to the ratio of OD600 abundances by the conversion factor K_{ij}. Therefore K_{ij} was directly measured for each pair of strains by growing monocultures of each strain in denitrifying conditions, harvesting cells after 64 h, measuring OD600, combining monocultures in equal-volume (450 μL) mixtures, and then processing, sequencing, and analyzing mixtures. Relative amplicon abundances of these mixtures along with OD600 measurements of the constituent monocultures were used to solve Equation 11 for the parameters K_{ij} for each pair. Then these conversion factors were used to transform the 16S amplicon relative abundances for pair cultures to OD600 relative abundances. These measurements were compared with the OD600 relative abundance predictions of Equation 10 (Figure S4B). In general, the model predictions for strain relative abundances closely matched the observed values, indicating that the model accurately predicts community compositions in the majority of cases using only information from monocultures. There were a small number of pair cultures with modest differences between predicted and observed relative abundances, mainly involving combinations of the Nar strains PAR01 and PNT03 and the Nir strains AGB01 and PDM13. These lower quality predictions may reflect interactions between these phenotypes not captured in the model (Equation 10).

Finally the ability of additive model to predict community nitrate and nitrite dynamics from individual strain consumer-resource parameters was evaluated. To do this, a normalized root-mean-square error (NRMSE) was computed for a given N-strain community as:

$$\mathrm{NRMSE}_{1,\ldots,N} = \frac{\mathrm{RMSE}_{1,\ldots,N}}{\left(\frac{1}{N}\sum_{i=1}^{N}\mathrm{RMSE}_i^2\right)^{1/2}}, \qquad \text{(Equation 12)}$$

where $\mathrm{RMSE}_{1,\ldots,N}$ is the root-mean-square error between measurements and predictions for the community, and RMSE_i is the error for each constituent strain in monoculture, with errors averaged over experimental replicates. The monoculture RMSEs of each strain were used in this normalization in order to correct for variations in monoculture fit quality. NRMSE in the range 0–2 indicates errors in 2-strain communities that are within twofold of fits associated with their constituent monocultures, while values of NRMSE much greater than this indicate low quality predictions. It should be noted that, because the denominator of Equation 12 depends on the RMSE of the constituent monocultures in a community, a potential pathology is that NRMSEs can be modestly inflated when the RMSEs for constituent monocultures are all small (indicating a strong correspondence between the data and the model).

However, this pathology is expected to be rare because it requires all monoculture RMSEs to be small.

The NRMSEs for all pairs of 12 strains cultured in separate nitrate and nitrite medium conditions are shown in Figures S3A and S3B. For most pair communities, typically low values of NRMSE indicated that Equation 10 made high quality predictions in most cases. The apparent exception to this was Nar + Nir communities (comprising any combination of Nar strain and Nir strain) initialized with nitrate (Figure S6), for which NRMSE values appeared much higher than for any other group. Permutation tests were then performed on the mean NRMSE values within phenotypic groups to determine whether the Nar + Nir group had significantly higher NRMSE than other groups (1×10^5 permutations). Since 10 hypothesis tests were performed in this manner, a Bonferroni-corrected threshold of $p = 0.05/10 = 0.005$ was used for testing at the 5% significance level. These tests indicated that only the Nar + Nir group in nitrate medium conditions had a significantly large mean NRMSE value ($p < 1\times10^{-5}$).

The NRMSEs for 108 3–5-strain communities cultured in separate nitrate and nitrite medium conditions are shown in Figure S3E. As with pair cultures, many 3–5-strain communities communities have low values of NRMSE indicating that Equation 10 made high quality predictions of nitrate and nitrite dynamics. Also, most apparent failures of the model predictions occurred when a community contains both a Nar strain and a Nir strain.

Up to this point, to test the ability of the consumer-resource model to predict community metabolic dynamics, directly measured values of the consumer-resource parameters were used to make community predictions. Using regressions instead to make predictions of single-strain phenotypes from gene presence/absence would be expected to add some degree of error to community metabolite dynamics predictions. To quantify this additional error, regressions on each of the SDM consumer-resource parameters (Figures 4C–4F) were used to predict these parameters for the each of the 12 strains, and then these parameters were used to predict community dynamics in the pair cultures and 3–5-strain communities. The NRMSEs evaluating the accuracy of these predictions relative to observed community metabolite dynamics are shown in Figure S5. For pair cultures (Figures S5A and S5B), NRMSEs changed little relative to using the directly measured parameters to make predictions; the median difference between NRMSEs using regression predicted parameters versus measured parameters for pair cultures in nitrate was -0.1, and for pair cultures in nitrite the median difference was approximately zero. NRMSEs increased modestly for 3–5-strain communities (Figure S5C); the median difference was 0.5 for communities in nitrate, and 1.4 for communities in nitrite.

Correcting for Nar + Nir interactions

The additive *N*-strain consumer-resource model, Equation 10, generally failed to predict the dynamics of communities initialized with nitrate that included both a Nar and a Nir strain (see plots of all Nar + Nir pairs in Figure S6). In every instance, the nitrate reduction rate of the Nar strain appears to be diminished relative to the rate in monoculture, and in some instances the nitrite reduction rate for the Nir strain appears to be increased relative to monoculture. Since Nar and Nir strains utilize different electron acceptors and therefore do not plausibly compete for any resource under these experimental conditions, it was concluded that interactions aside from resource competition must be taking place.

It was therefore investigated whether the predictions of the additive model in Equation 10 could be improved by correcting for interactions between Nar and Nir strains. To do this, the nitrate and nitrite reduction parameters r_A^i and r_I^j of the Nar strain *i* and the Nir strain *j*, respectively, were refit using the measured metabolite dynamics data from the pair cultures of these strains. Changes to the reduction rate parameters rather than the yields (γ_A^i and γ_I^j) were investigated because the additive model accurately predicted endpoint optical densities in all pair communities (Figure S4A), and therefore there was no evidence that interactions between Nar and Nir strains involved a change in yields. However, given the hypothesis that Nir strains inhibit Nar strains via excretion of cytotoxic nitric oxide (see discussion), it is plausible that interactions may involve a change in yields that are not detectable given the precision of the optical density measurement.

Nitrate and nitrite reduction rate parameters for each Nar + Nir pair culture were refit in the following way:

1. Refit r_A^i for the Nar strain *i*, holding all other parameters fixed. Record the NRMSE for the resulting prediction.
2. Refit both r_A^i for the Nar strain *i* and r_I^j for the Nir strain *j*, holding all other parameters fixed. Record the NRMSE for the resulting prediction.
3. If the NRMSE obtained in step 2 was more than 10% smaller than the NRMSE in step 1, then accept the refit parameters obtained in step 2, denoting these values as $\tilde{r}_A^{i,j}$ and $\tilde{r}_I^{j,i}$. Otherwise, accepted the refit parameter obtained in step 1 as $\tilde{r}_A^{i,j}$, and let $\tilde{r}_I^{j,i} = r_I^j$.

Refitting was performed as described above for Equation 3. In step 3, improvements in fit quality obtained by refitting only r_A versus refitting both r_A and r_I were compared in order to identify cases where increases in nitrite reduction rate were necessary to improve fits of Equation 10 to the data.

The results of this refitting procedure are shown in Figure S7. These results demonstrate that, in all cases, the nitrate reduction rate of the Nar strain was slowed ($\tilde{r}_A < r_A$) in Nar + Nir pair culture. Additionally, in several cases the nitrite reduction rate of the Nir strain was increased ($\tilde{r}_I > r_I$) in Nar + Nir pair culture. Each Nar strain is affected in essentially the same way by every Nir strain (e.g., the nitrate reduction rate of Nar strain PAR01 diminished by approximately 50% in every pair culture with a Nir strain). This observation is consistent with the proposal that nitric oxide toxicity impacted nitrate reduction by the Nar-strain in a manner that is specific to each Nar strain (see discussion).

These refit parameter values were then used in Equation 10 to generate new predictions for 3–5-strain communities containing at least one Nar + Nir pair. To do so, the following rules were employed for replacing r_A and r_I in Equation 10, which depend on the number of Nar and Nir strains in the community:

1. One Nar strain i and one Nir strain j: $r_A^i = \tilde{r}_A^{i,j}$, $r_I^j = \tilde{r}_I^{j,i}$.
2. Two Nar strains i and j and one Nir strain k: $r_A^i = \tilde{r}_A^{i,k}$, $r_A^j = \tilde{r}_A^{j,k}$, $r_I^k = (\tilde{r}_I^{k,i} + \tilde{r}_I^{k,j})/2$.
3. One Nar strain i and two Nir strains j and k: $r_A^i = (\tilde{r}_A^{i,j} + \tilde{r}_A^{i,k})/2$, $r_I^j = \tilde{r}_I^{j,i}$, $r_I^k = \tilde{r}_I^{k,i}$.
4. General case with N Nar strains in the set $\mathcal{S}_{Nar}$ and M Nir strains in the set $\mathcal{S}_{Nir}$:

$r_A^i = 1/M \sum_{j \in \mathcal{S}_{Nir}} \tilde{r}_A^{i,j}$ for all $i \in \mathcal{S}_{Nar}$ and $r_I^j = 1/N \sum_{i \in \mathcal{S}_{Nar}} \tilde{r}_I^{j,i}$ for all $j \in \mathcal{S}_{Nir}$.

The results of using refit Nar and Nir parameters to predict 3–5-strain cultures are shown in Figure 7B (yellow points). Correcting predictions using refit r_A and r_I parameters substantially improved prediction quality, reducing median NRMSE values from 1.68 to 0.92. These results did not appreciably change if a min or max function is used instead of a mean.

Supplemental figures

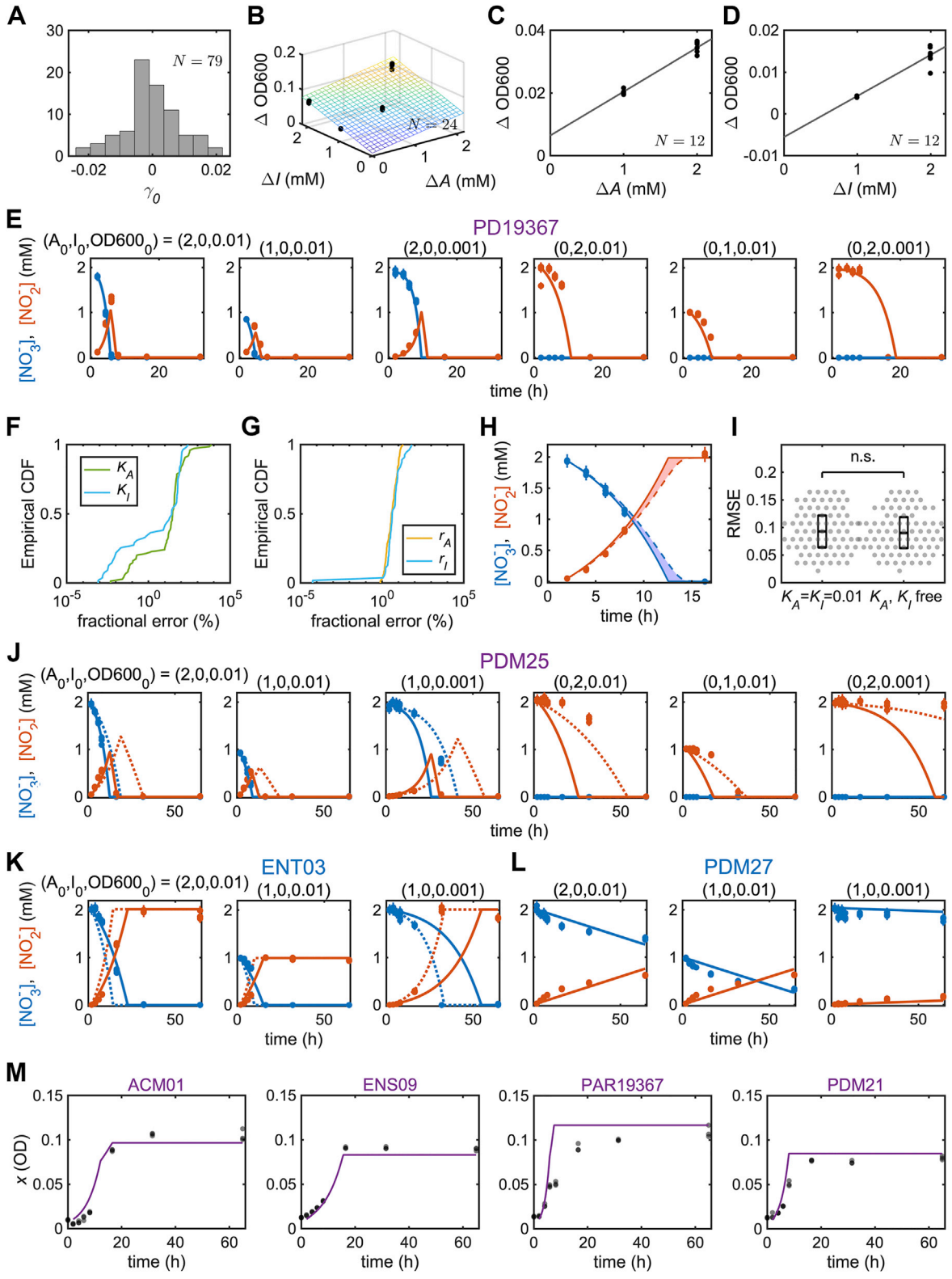

(legend on next page)

Figure S1. Fitting consumer-resource parameters, related to Figure 3

(A) Histogram showing the distribution of yield intercept (γ_0) values for 79 strains cultured in SDM. Units are dimensionless absorbances at 600 nm, path length normalized to 1 cm.

(B–D) Examples of yield parameter fits using data obtained in different growth conditions. Points show observed values of $\Delta OD600 = OD600_{64} - OD600_0$ from different conditions where different amounts of nitrate and nitrite are reduced ($\Delta A = A_0 - A_{64}$ and $\Delta I = A_0 - A_{64} + I_0 - I_{64}$, respectively) with 4 replicates used in each condition. The plane/lines show the least-squares fits of the data to Equation 6 (STAR Methods). (B) shows the yield fit for the Nar/Nir strain *P. denitrificans* ATCC 19367 in SDM. (C) shows the yield fit for the Nar strain *Raoultella* sp. RLT01 in SDM. (D) shows the yield fit for the Nir strain *Pseudomonas* sp. PDM13 in SDM.

(E) Example global fits of the consumer-resource model (Equation 3; STAR Methods) to nitrate and nitrite dynamics data for the Nar/Nir strain *P. denitrificans* ATCC 19367 cultured in SDM. Points show measured concentrations of nitrate and nitrite, and curves show optimal model fits. Four replicates were used in each experimental condition.

(F and G) Distributions of fractional errors (%) for (F) the affinity parameters K_A and K_I and (G) the rate parameters r_A and r_I, fit using SDM monocultures. Distributions were computed via nonparametric bootstrap with K_A, K_I constrained during fitting between 0.001 and 10. Fractional error is defined as the ratio of the interquartile range obtained via bootstrapping to the value of the parameter obtained using a standard fit to all experimental data.

(H) Example nitrate and nitrite dynamics for the Nar strain *Raoultella* sp. RLT01 cultured in SDM. Solid lines show the fit to Equation 3 (STAR Methods) holding K_A fixed at 0.001, while dashed lines show fits holding $K_A = 0.1$.

(I) Comparison of model fit errors (RMSE) for $N = 79$ denitrifying strains cultured in SDM. Fits that hold $K_A = K_I = 0.01$ and fits that take K_A and K_I as free fitting parameters are compared. A two-sample Kolomogorov-Smirnov test accepts the null hypothesis that underlying distributions for the two samples are the same $(p = 0.97)$. Boxplots indicating quartiles of each distribution are shown.

(J) Example Nar/Nir strain PDM25 cultured in SDM for which reduction rates were fit using all experimental conditions (dashed lines, RMSE = 0.177) and using only conditions where nitrate was initially supplied (solid lines, RMSE = 0.138).

(K) Example Nar strain ENT03 cultured in SDM for which the reduction rate r_A was fit using all experimental conditions (dashed lines, RMSE = 0.254) and using only conditions where $OD600_0 = 0.01$ (solid lines, RMSE = 0.095).

(L) Example Nar strain PDM27 cultured in SDM for which nitrate concentrations appear to asymptotically approach a nonzero value.

(M) The biomass densities of four Nar/Nir strains (*Achromobacter* sp. ACM01, *Ensifer* sp. ENS09, *Paracoccus denitrificans* ATCC 19367, and *Pseudomonas* sp. PDM21) grown in SDM were measured in denitrifying conditions over 64 h (points) to validate the predictions (curves) of the consumer-resource model (Equation 3; STAR Methods). The parameters for each strain were inferred in previous SDM monocultures (STAR Methods). 2 mM NO_3^- was initially supplied to each culture, and three experimental replicates were used for each time point. The median relative errors in biomass density predictions at $t = 64$ h were −5.2%, −7.5%, 9.4%, and 6.4% for ACM01, ENS09, PAR19367, and PDM21, respectively.

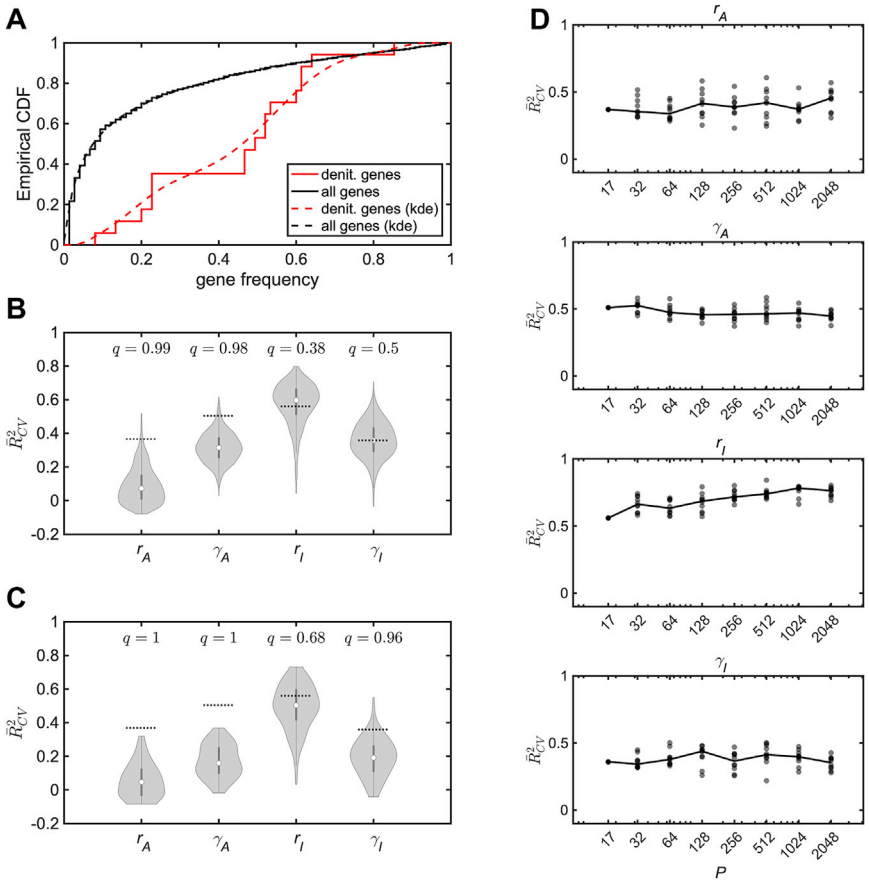

Figure S2. Randomly selected genes as alternative predictors for consumer-resource parameters, related to Figure 4

(A) Distributions of gene presence frequency (fraction of strains that possess a given gene) for denitrification-related genes (red) and the distribution of gene presence frequency for all other annotated genes (black), both in the ensemble of the 75 nitrate-reducing strains. Solid lines show empirical cumulative distribution functions (CDFs) of gene frequencies, and dashed lines show kernel density estimates of these distributions (bandwidth = 0.4).

(B and C) Distributions of $\overline{R}^2_{CV}$ values obtained by regressing each of the SDM consumer-resource parameters onto the presence and absence of sets of randomly selected genes (1×10^3 sets of random genes per consumer-resource parameter). (B) shows results for genes randomly selected from the set of all annotated genes across strains in our library, while (C) shows results for genes randomly selected from the set of all annotated genes excluding those that have large and significant correlation ($|\rho| \geq 0.5$) with any denitrification genes. Dashed lines indicate $\overline{R}^2_{CV}$ values obtained in regressions onto the presence and absence of denitrification-related genes (the same values are shown in both panels) with the corresponding quantile values (q).

(D) Points show distributions of $\overline{R}^2_{CV}$ obtained by regressing the SDM consumer-resource parameters onto sets of the 17 denitrification genes plus $P - 17$ additional randomly selected genes (10 predictor sets per consumer-resource parameter), and the solid lines pass through the median values of these distributions as a function of P. The values of $\overline{R}^2_{CV}$ shown at $P = 17$ are the same as the values indicated by dashed lines in (B) and (C).

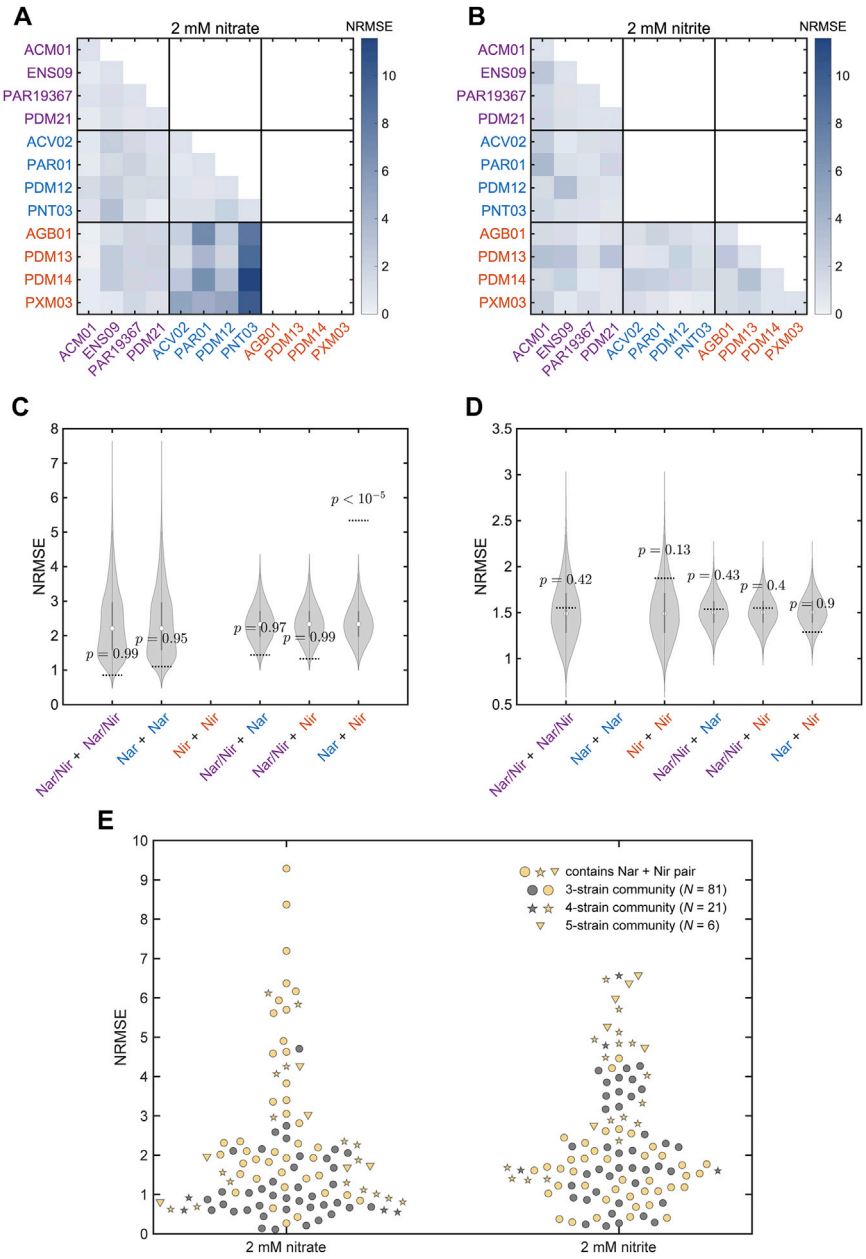

Figure S3. Accuracy of consumer-resource nitrate/nitrite dynamics predictions for simple communities, related to Figures 6 and 7

(A and B) Normalized RMSE (NRMSE) values comparing measurements and predictions for nitrate and nitrite dynamics in all pair communities of 12 strains. Values are grouped according to the constituent phenotypes in a community, with Nar/Nir strains labeled in purple, Nar strains in blue, and Nir strains in orange. (A) shows NRMSEs for communities initialized with 2 mM nitrate (with "Nir + Nir" communities omitted, since Nir strains do not utilize nitrate as an electron acceptor). (B) shows NRMSEs for communities initialized with 2 mM nitrite (with Nar + Nar communities omitted, since Nar strains do not utilize nitrite as an electron acceptor). All cultures were performed in SDM.

(C and D) Hypothesis testing on means of NRMSEs grouped by constituent phenotypes (e.g., Nar/Nir + Nar/Nir communities, etc.). Null distributions for group means are generated via permutation of group labels for each pair community (1×10^5 permutations) and are compared with the observed mean NRMSEs in each group (dashed lines). A Bonferroni-corrected threshold for 5% significance over 10 hypothesis tests is 0.005. Note that some groups contain only 6 NRMSE values (e.g., Nar/Nir + Nar/Nir communities), while others contain 16 NRMSE values (e.g., Nar/Nir + Nar communities). Panel C shows hypothesis testing on the NRMSE values in (A) (communities initialized with nitrate), while (D) shows inference on the values in (B) (communities initialized with nitrite).

(E) Distributions of NRMSE values comparing measurements and predictions for nitrate and nitrite dynamics in 3–5-strain communities ($N = 108$). Communities were cultured in SDM and separately initialized with 2 mM nitrate or 2 mM nitrite. Points in yellow indicate values for communities that contain both a Nar strain and a Nir strain.

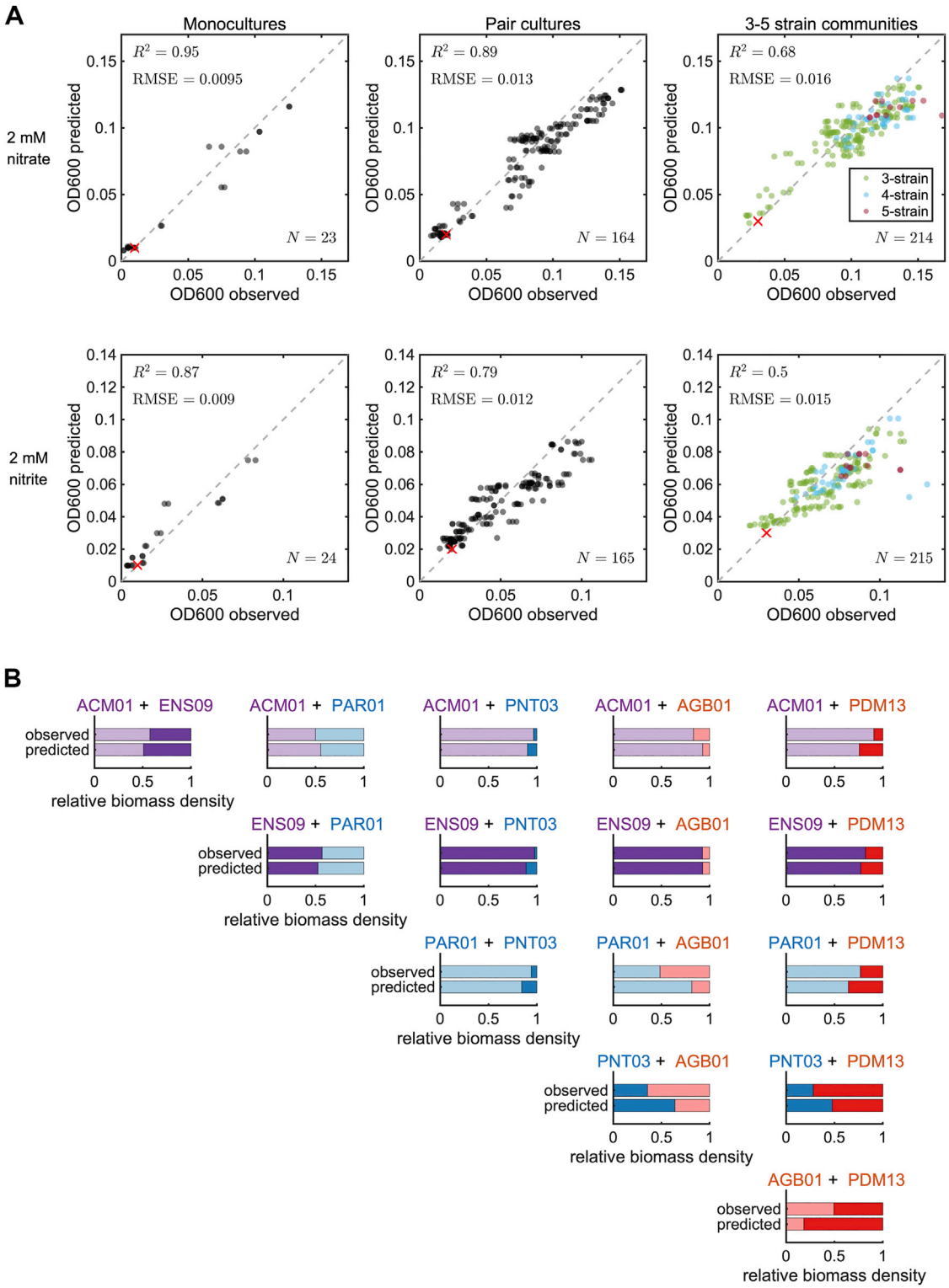

Figure S4. Accuracy of consumer-resource endpoint biomass density and composition predictions, related to Figure 6

(A) Comparisons between observed endpoint optical densities and values predicted by the additive consumer-resource model (Equation 10; STAR Methods), where the latter was obtained by summing the endpoint biomass densities of each strain in the community. Comparisons are shown for monoculture controls, pair cultures, and 3–5-strain communities, in 2 mM nitrate and nitrite media conditions separately. All cultures were performed in SDM. Initial optical densities are indicated (red cross), and coefficients of determination R^2 and root-mean-square errors (RMSE) for observed versus predicted values are shown.

(legend continued on next page)

(B) Comparisons between observed relative biomass densities and relative biomass densities predicted by the additive consumer-resource model (Equation 10; STAR Methods). Root-mean-square error for observed versus predicted relative abundances across all pairs is 0.16. Endpoint community relative abundances were measured for all pair cultures of the six strains *Achromobacter* sp. ACM01 (Nar/Nir), *Ensifer* sp. ENS09 (Nar/Nir), *Paracoccus* sp. PAR01 (Nar), *Pantoea* sp. PNT03 (Nar), *Agrobacterium* sp. AGB01 (Nir), and *Pseudomonas* sp. PDM13 (Nir). All cultures were performed in SDM initiated with 2 mM NO_3^-, with the exception of the pair culture of the two Nir strains AGB01 and PDM13, which was initiated with 2 mM NO_2^-. Relative abundances of 16S rRNA amplicons were measured using CASEU (Cermak et al., 2020; STAR Methods). To make comparisons in terms of relative biomass densities, conversion factors from 16S amplicon relative abundance to relative biomass density were computed using mixtures of monocultures (Equation 11; STAR Methods).

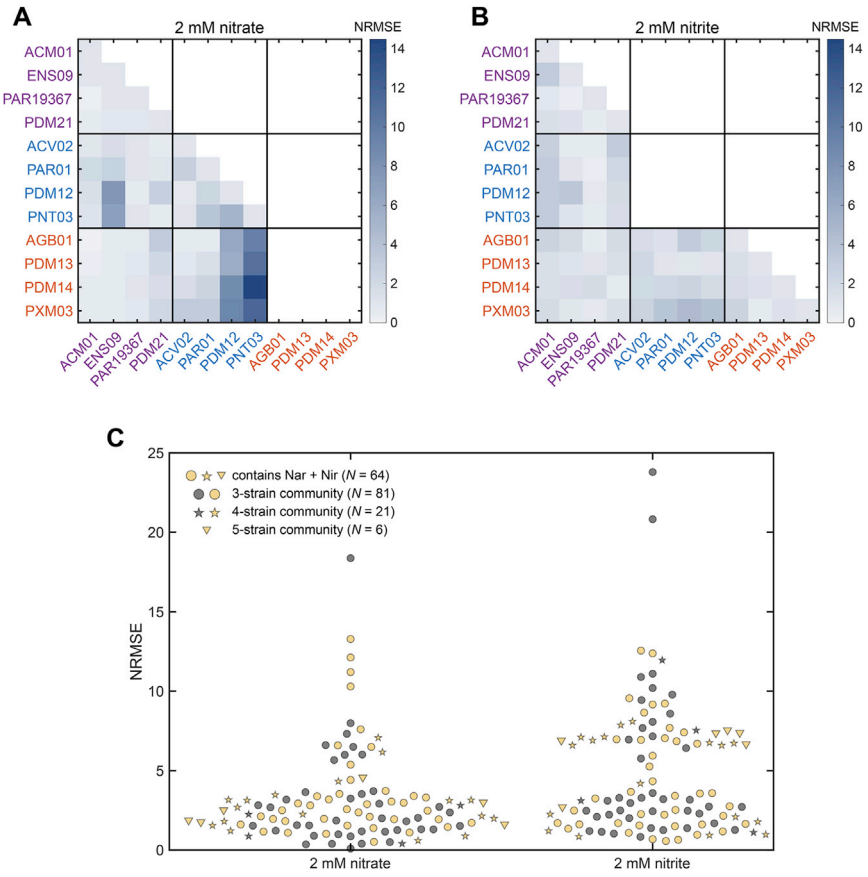

Figure S5. Accuracy of consumer-resource nitrate/nitrite dynamics predictions for 2–5-strain communities using genomic predictions of phenotypes, related to Figures 6 and 7

(A–C) NRMSE values comparing measurements and predictions for nitrate and nitrite dynamics in (A and B) pair cultures and (C) 3–5-strain communities (N = 108). Predictions were made using regressions in Figure 4 to predict single-strain consumer-resource parameters from gene presence/absence, which were, in turn, used by the consumer-resource model to predict metabolite dynamics. This is in contrast to Figures 6, 7, and S3, where predictions for metabolite dynamics were made using directly measured values of consumer-resource parameters. Communities were cultured in SDM and were separately initialized with 2 mM nitrate and 2 mM nitrite. Points in yellow indicate values for communities that contain both a Nar strain and a Nir strain.

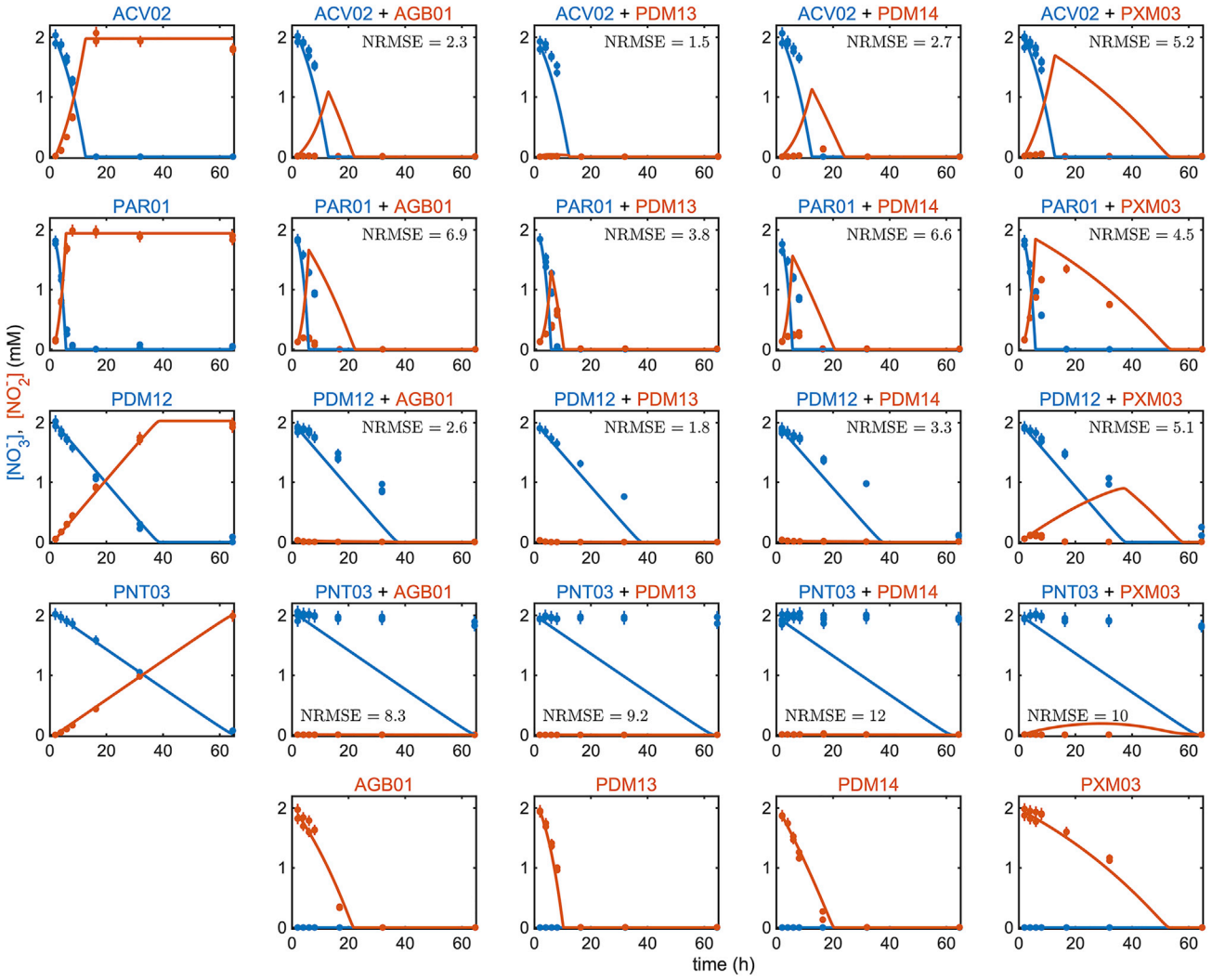

Figure S6. Nitrate/nitrite dynamics for Nar + Nir pair cultures, related to Figures 6 and 7

Monoculture controls are shown for Nar strains (left column) and Nir strains (bottom row). Points show measured concentrations of nitrate and nitrite, and curves show predictions of Equation 10 (STAR Methods). NRMSE values for pair cultures are shown. 2–3 experimental replicates are used for each combination of strains. All cultures were performed in SDM.

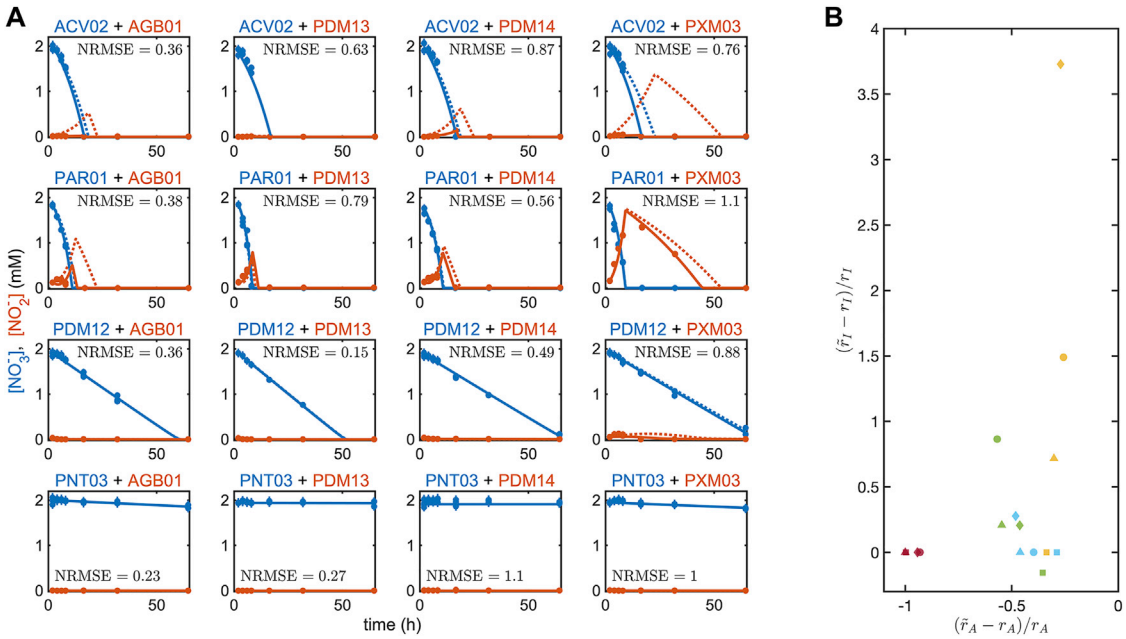

Figure S7. Refitting model parameters for Nar + Nir pair cultures, related to Figure 7

(A) The r_A parameter for the Nar strain and/or the r_I parameter for the Nir strain were refit to the Nar + Nir pair culture measurements to obtain new parameter values $\tilde{r}_A$ and $\tilde{r}_I$, respectively. In some cases (panels with only solid lines), it was only necessary to refit the r_A parameter to obtain a good model fit. In other cases (panels with both solid and dashed lines), better fits (more than 10% smaller NRMSE) could be obtained by refitting both r_A and r_I (solid lines). NRMSE values for refit models are indicated. 2–3 experimental replicates are used for each combination of strains.

(B) Relative changes in r_A and r_I parameters. Nar strains are coded by color: ACV02 (yellow), PAR01 (green), PDM12 (blue), and PNT03 (red). Nir strains are coded by symbol: AGB01 (circle), PDM13 (square), PDM14 (triangle), and PXM03 (diamond). NRMSE values for pair cultures are shown. All cultures were performed in SDM.